# 論文 / 著書情報
# Article / Book Information

| | |
|---|---|
| 題目(和文) | 相互反応や反応速度論的解析および反応メカニズムに着目した精油汚泥または精油汚泥チャーとバイオマスの熱分解および共燃焼挙動の解明 |
| Title(English) | Pyrolysis and combustion of oil sludge/oil sludge char with biomass focusing on interactions, kinetics, and mechanisms |
| 著者(和文) | XuHao |
| Author(English) | Hao Xu |
| 出典(和文) | 学位:博士(工学),<br>学位授与機関:東京工業大学,<br>報告番号:甲第12225号,<br>授与年月日:2022年9月22日,<br>学位の種別:課程博士,<br>審査員:高橋 史武,中崎 清彦,CROSS JEFFREY SCOTT,江頭 竜一,時松 宏治 |
| Citation(English) | Degree:Doctor (Engineering),<br>Conferring organization: Tokyo Institute of Technology,<br>Report number:甲第12225号,<br>Conferred date:2022/9/22,<br>Degree Type:Course doctor,<br>Examiner:,,,, |
| 学位種別(和文) | 博士論文 |
| Type(English) | Doctoral Thesis |

**Doctoral Dissertation**

# Pyrolysis and Combustion of Oil Sludge/Oil Sludge Char with Biomass focusing on Interactions, Kinetics, and Mechanisms

**Xu Hao**

**Supervisor: Professor Fumitake Takahashi**

**Department of Transdisciplinary Science and Engineering**
**School of Environment and Society**
**Tokyo Institute of Technology**

**September 2022**

# Acknowledgments

Foremost, I would like to express my sincere gratitude to my supervisor, Assoc. Prof. Fumitake Takahashi for accepting me as a doctoral student and for his helpful guidance and support for my research and life. His rigorous attitude towards research, constant pursuit of new things, and balance between work and family, will be the direction of my future academic path. Also, I would like to express my great gratitude to Assis. Prof Shuo Cheng for her patient guidance, valuable suggestions for my research and future career, and for teaching me how to think from the whole perspective. I want to express my great gratitude to Prof. Kunio Yoshikawa for research opportunities and helpful guidance. I would appreciate Assoc. Prof. Koji Tokimatsu and Prof. Jeffrey S. Cross for their kind recommendations and support for my research and life. Also, I would like to express my gratitude to all my referees for valuable suggestions to improve my work.

I would like to thank Mrs. Eriko Ohno for her administrative work and help during my study. I would appreciate the China Scholarship Council (CSC) for financial support.

I would like to thank all members of Takahashi-Tokimatsu Lab for the scientific discussion and non-scientific fun hours.

Last but not least, I would be sincerely grateful to my family for their endless love and support.

# Table of Contents

# List of Figures

# List of Tables

# Chapter 1 Introduction

## 1.1 Background

Rapid global industrialization and economic growth increase demand for petroleum-based products and are estimated to increase by 35% by 2025 [1-1]. At the same time, a large amount of oil-containing waste, known as oil sludge, is inevitably generated during the exploration, transportation, storage, and refining of oil [1-2, 1-3]. Oil sludge has a complex composition and contains toxic and harmful substances such as petroleum hydrocarbons, waste chemicals, and heavy metals. Without or improper disposal, it will cause severe environmental pollution and threaten human health and ecosystems [1-3]. Therefore, oil sludge has been classified as a hazardous waste in many countries. At present, efficient and clean disposal methods are the mainstream concerns of oil sludge disposal in terms of its large output and harmfulness. From the perspective of the 3R principle (Recycle, Reuse, and Reduce) in waste treatment, oil sludge contains high content of value-added hydrocarbon components, through recycling which can be used as alternative fuel products and mitigate the dilemma of fossil energy depletion.

In recent years, various methods have been developed for oil sludge treatment, among which thermochemical treatments can effectively achieve resource recovery and terminally non-hazardous disposal simultaneously [1-4]. Therefore, a comprehensive thermochemical treatment, combining pyrolysis and combustion, has been regarded as a promising method to deal with oil sludge [1-5]. However, limited research has been conducted on this integrated treatment. This system itself is an energy-intensive process, requiring necessary measures to reduce the high energy consumption and operational cost. Consequently, it is of great research significance to further improve the processing efficiency and the internal energy recycling in this system. Based on the above background, this work conducts research on co-pyrolysis and co-combustion of oil sludge/oil sludge char.

## 1.2 Overview of oil sludge

The yield of oil sludge is dependent on the output of crude oil and the larger throughput of crude oil results in higher production of oil sludge. According to the *BP Statistical Review of World Energy 2019* [1-6], the United States is still the country processing the most significant volume of crude oil in the world in 2018, whose refining volume accounted for 18.8%, followed by China with 15.6%. It is estimated that 1 ton of oil sludge is produced for every 200 tons of crude oil produced or processed [1-7]. Taking China's crude oil status as an example, according to the 2021 China Statistical Yearbook [1-8], as shown in **Figure 1.1**, the production and import of crude oil gradually increased in the past ten years, reaching approximately 800 million tons in 2019. Therefore, it is certain that the production of oil sludge will continue to grow because of the ascending global demand for petroleum products.

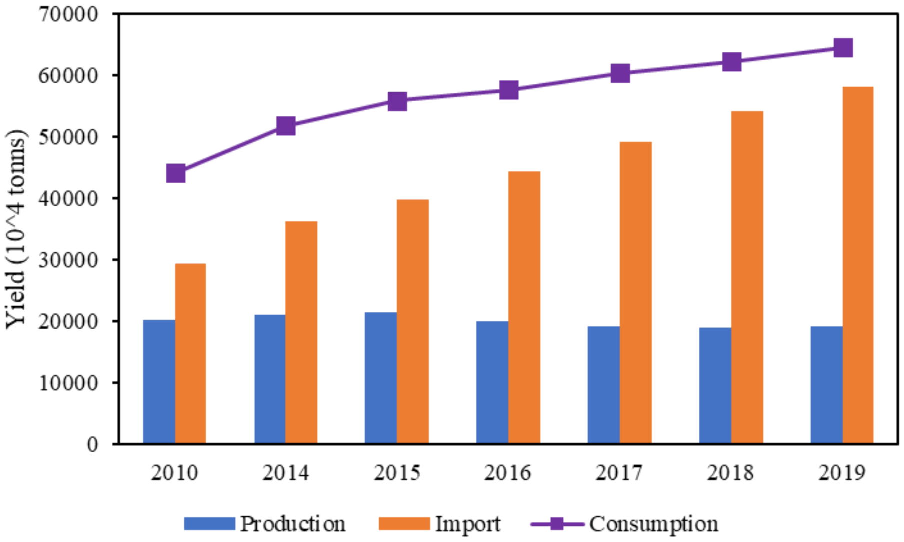

**Figure 1.1** Oil supply and consumption in China

### 1.2.1 Classification of oil sludge

Oil sludge is a byproduct generated from exploration, transportation, storage, and refining during crude oil processing. Consequently, it can be classified as oilfield sludge, oil tank sludge, and refinery sludge based on their sources.

Oilfield sludge is mainly produced during oilfield exploitation, drilling, and other operations, including oil-contaminated soil at oil wells (falling sludge), sediments from the separation system of union stations, and drilling mud. Falling sludge is generated due to the accidents, running off, and dripping during the exploitation of oilfield, where oil penetrates or drops on the ground and is mixed with soil, sand, water, etc., to form an oil-soil mixture with oil content ranging from 10-30% [1-9]. Meanwhile, falling sludge contains low moisture, more sediment, high density, high viscosity, and poor fluidity [1-10]. Falling sludge is often accumulated in a fixed control area. As the accumulation time increases, the light components are evaporated, and the asphaltene and colloidal components get enriched, increasing the difficulty of separating oil and soil. Drilling mud is oil-containing waste mud generated in oilfield drilling, with high water content, viscous fluid or semi-fluid state, and many chemicals [1-11]. The annual yield of oilfield sludge in China is around 1 million tons, of which falling sludge accounts for 10% [1-12]. Oilfield sludge seriously pollutes the surrounding soil and water environment, accompanied by a large and wide pollution area.

During the storage of crude oil or petroleum products, some impurities like sediments and metal salts in the oil, as well as heavy components such as colloid and asphaltene, are prone to be deposited at the bottom due to natural sedimentation to form a black and thick colloidal material, which is called oil tank sludge [1-13]. The amount of oil tank sludge obtained from oil storage tank cleaning in China can reach about 1 million tons every year [1-14]. Compared to oilfield sludge, the oil content in oil tank sludge is relatively high, ranging from 30-70%, entailing higher resource utilization value [1-15]. Nonetheless, due to the addition of cleaning agents during the cleaning process, the water content and the degree of water-oil emulsification are enhanced, thus increasing the difficulty of separation [1-16].

Refinery sludge is the grease trap bottom sludge, flotation tank scum, and excess activated sludge produced by the oil sewage in the refinery after oil separation, flotation, sedimentation, and other purification processes [1-17]. Refinery sludge contains a higher amount of water and oil, as well as heavy components [1-18]. The composition of refining sludge is very complex and varies depending on the types of pollutants in the oil sewage and the used chemicals. It often contains bacteria, microorganisms, etc., and it is difficult to undergo advanced treatment, posing serious pollution to the water environment [1-19].

### 1.2.2 Characterization of oil sludge

Oil sludge is a highly emulsified viscous semi-solid with three phases of oil, water, and solid, as shown in **Figure 1.2**. It contains aged crude oil, asphaltenes, bacteria, suspended solids, heavy metals, chemicals, behaving as stable properties [1-3]. The asphaltenes, colloids, and fine particles in the water-oil interface play the role of interface active materials, promoting the emulsification of water and oil, and forming water-in-oil (W/O) emulsion. Typically, oil sludge contains about 30-50% water, 30-80% oil, and 10-20% solid particles, which vary over a wide range depending on crude oil source, production, and processing scheme [1-20, 1-21]. Moreover, the equipment and reagents used in crude oil processing also affect the properties of oil sludge. For example, the oil content in the oilfield sludge used in this work is around 20%, with a low water content (~ 10%) and relatively high content of solid particles up to approximately 70%.

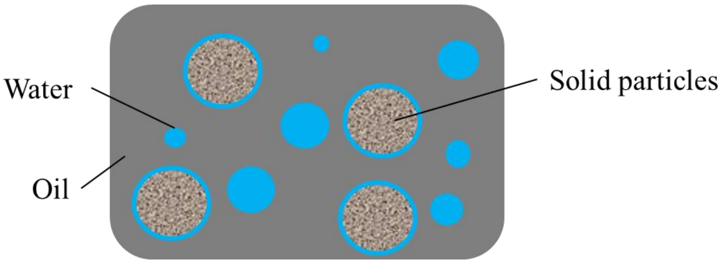

**Figure 1.2** Typical composition of oil sludge

The oil phase in oil sludge is derived from crude oil, mainly composed of four fractions: saturates, aromatics, resins, and asphaltenes, as well as a small amount of heteroatom organic compounds such as oxygen, sulfur, and nitrogen. Saturates and aromatics are collectively referred as petroleum hydrocarbons. Their content can reach more than 70% in oil sludge, including straight-chain paraffin, cycloparaffin, benzene, toluene, xylenes, naphthalene, and various polycyclic aromatic hydrocarbons (PAHs)

[1-3]. The resin fraction contains polar compounds such as carboxylic acids and N or S-containing compounds (e.g., thiophenes and pyridines). Asphaltenes fraction has a complex composition compared to other fractions, consisted of PAHs, heteroatoms (O, S, and N), cycloparaffin, and even metal atoms (Ni, V) connected by alkaline bridges or ether bonds. Resin and asphaltenes are heavy hydrocarbons and are challenging to degrade; consequently, they are prone to accumulate at the bottom during the storage of crude oil, which concentrations increase with the volatilization of light-weight components resulting in an enhancement of density and viscosity of oil sludge [1-22]. The oxygen and nitrogen contents in oil sludge are relatively low, around 0.05-1.5% and 0.1-2.0%, respectively. Whereas the sulfur content is higher, accounting for 0.05-6.0% [1-23]. in addition, the enrichment of thiophene in heavy oil increases the sulfur content, reaching 8% [1-24]. Therefore, the sulfur content in oil-rich oil sludge, especially oil sludge composed of high fractions of heavy compounds, can be relatively high.

The composition of solid matrices in oil sludge varies significantly depending on the source of oil sludge. For example, the solid particles of oilfield sludge mainly include quartz, silicates, and other minerals, as they come from rocks, soil, and sand [1-3]. Oil sludge also contains metal oxides, such as rust and paint in oil tank sludge and refinery sludge, scaling from corrosion of pipes and tank walls [1-13]. A variety of heavy metals is also found in oil sludge. For example, the metal concentration in refinery sludge was reported as Zn (1299 mg/kg), Fe (60200 mg/kg), Cu (500 mg/kg), Cr (480 mg/kg), Ni (480 mg/kg), Pb (565 mg/kg), and V (2400 mg/kg), respectively [1-19, 1-25, 1-26].

### 1.2.3 Hazards of oil sludge

Oil sludge poses severe pollution to soil, water, and air environment and causes harm to human health due to the presence of high concentrations of toxic components. Generally, it can be embodied in the following aspects: (1) the petroleum hydrocarbons in oil sludge will penetrate the soil as oil sludge is directly discarded on the ground, changing the physical and chemical properties of soil [1-27]. On one hand, the organic components will combine with nitrogen, phosphorus, and other elements in soil, leading to the inability of nutrients to be absorbed by plants. On the other hand, oil sludge will increase soil viscosity, and the heavy fractions are prone to be adsorbed on the soil surface, forming a hydrophobic coating, and blocking the soil water-conducting channels, which will reduce soil water permeability, hinder plant water adsorption, and affect plant and crop growth [1-28]; (2) large amount of petroleum hydrocarbons in oil sludge will flow into rivers and lakes with natural rainfall during stacking. The oil fractions float on the water surface, preventing the oxygen in the air from entering the water body for gas exchange, resulting in the ineffective supplementation of dissolved oxygen in the water, limiting the survival of aquatic organisms, thereby destroying the balance of the water ecosystem [1-29]; (3) when oil sludge is directly stacked without treatment, the light organic components will volatilize into the air with increasing ambient temperature, polluting the atmosphere and releasing foul odors. In addition, flammable and explosive gases such as methane and hydrogen are easily generated during the stacking of oil sludge. Burning and explosion accidents are prone to occur without effective management [1-30]; (4) oil sludge contains a lot of polycyclic aromatic hydrocarbons. These substances have strong teratogenicity and carcinogenicity, and they will irritate the respiratory and skin, and seriously harm human health after entering the human body. Furthermore, many heavy metals in oil sludge will be enriched by crops after penetrating the soil and finally go into the human body through the food chain, which will cause genotoxicity to humans [1-31].

Considering the harm of oil sludge to the ecological environment and human health, it is essential to take adequate measures to deal with oil sludge.

## 1.3 Overview of oil sludge treatment method

A number of methods have been developed for the treatment of oil sludge. The primary principle of oil sludge treatment is to achieve volume reduction and hazardous substances removal, and then resource recovery. Therefore, the treating methods can be classified into two groups: harmless disposal-based methods and resource recovery-based methods, as listed in **Figure 1.3**. Harmless disposal methods include oxidation, stabilization, incineration, and bioremediation. Oil sludge is a kind of solid waste, and the conventional disposal methods of solid waste are landfill and incineration, which requires much space and poses a serious threat to the atmosphere and groundwater environment [1-32]. Bioremediation is a novel and effective method to degrade organic components in oil sludge into light-weight compounds, reducing its potential hazards [1-12]. However, the degradation of PAHs takes a longer time, and it is difficult to decompose heavy metals; therefore, this technique remains further development [1-13]. Although harmless disposal is relatively thorough, the high-quality oil components in oil sludge cannot be recovered.

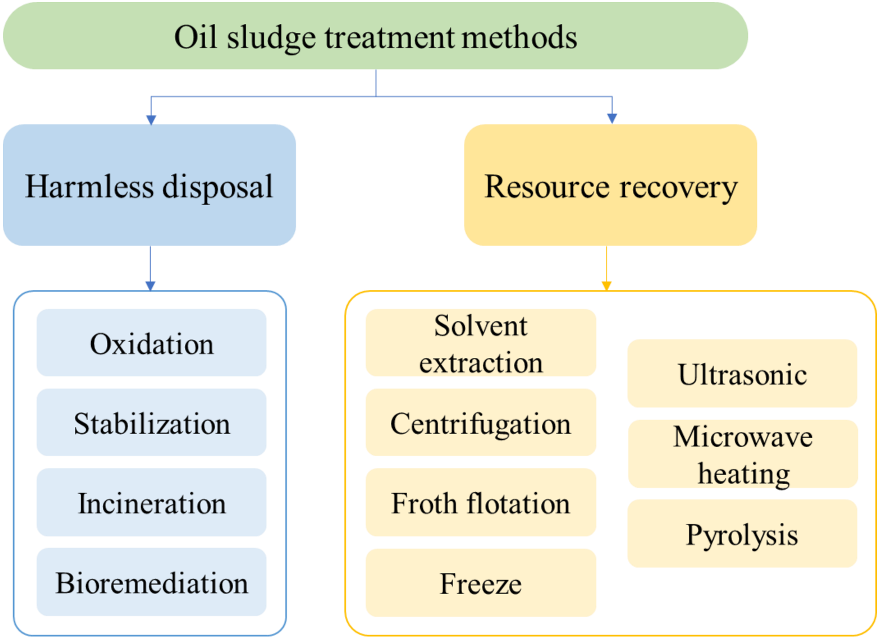

**Figure 1.3** Oil sludge treatment methods

According to the American Petroleum Institute (API) and *Technical Policy for Pollution Prevention and Control in the Oil and Gas Exploitation Industry* issued by China's Ministry of Environmental protection, the primary environmental consideration in handling oil sludge should be the maximization of hydrocarbon recovery. Therefore, resource recovery method for oil sludge treatment is the current research hotspot and this work is also focused on this field. Previous studies suggested that the oil sludge with oil content > 10% deserves oil recovery [1-33]. Resource recovery method generally includes solvent extraction, centrifugation, froth flotation, pyrolysis, ultrasonic, microwave heating, and freeze. The advantages and disadvantages of these methods are summarized in **Table 1.1**. During solvent extraction, the oil phase in oil sludge is dissolved in a specific solvent and recovered by evaporation. The remaining water and solids are removed by centrifugation [1-34]. This process is indeed feasible and efficient for oil recovery. However, a large number of solvents are consumed, and additional energy input is needed for evaporation and centrifugation [1-35]. Additionally, the volatilization of solvents will cause secondary pollution during extraction. Although centrifugation and froth flotation have been widely used due to their high effectiveness and low-cost, high-energy consumption and incomplete separation of oil and solid make the obtained oil unsatisfactory [1-36]. Ultrasonic and microwave heating show relatively high efficiency of oil recovery compared to other methods, whereas these emerging methods are still limited by their high operation cost and technical problem of scaling up [1-37, 1-38, 1-39]. The freeze method can effectively break the emulsified status of oil and water in oil sludge, then oil can be recovered [1-40]. However, this method is restricted by many factors, such as freezing temperature, heating and cooling rate, and water content. For oil-rich oil sludge, especially oil tank sludge, the dewatering effect is not obvious [1-41]. The freeze method is more suitable to be applied in cold areas, where the natural freeze can save energy.

Among these methods, pyrolysis is one of the resource recovery technologies worth in-depth research and industrial application. Pyrolysis of oil sludge is conducted at temperatures ranging from 350 to 600 °C in an inert atmosphere. Through pyrolysis, the organic substances in oil sludge are degraded, generating low-molecular-weight condensable oil and small-molecular non-condensable gas, which poses elevated heating value than raw oil sludge and can be selectively produced by controlling the operation conditions [1-42]. As mentioned above, resource recovery methods are often limited by the properties of oil sludge, as the composition of oil sludge varies from source to source and with the storing period. The advantage of pyrolysis is that this technology poses good material adaptability and can eliminate or weaken the feedstock impact on processing efficiency, especially oil sludge with high viscosity or high ash. The oil sludge-derived oil can be easily stored and transported, with a quality similar to low-grade petroleum distillates produced by refineries. From commercialization and practical application perspective, the mobility of the pyrolysis unit can facilitate the process implementation. For example, pyrolysis units can be directly transported to the oilfield sludge producing site, reducing transporting costs of waste to treatment plants [1-43].

**Table 1.1** Summary and comparison of oil sludge resource recovery methods

| Method | Cost | Oil recovery | Scale | Advantages | Disadvantages |
|---|---|---|---|---|---|
| Solvent extraction | High | 50-90% | Large | Effective; large processing capacity | A large volume of organic solvent consumption; secondary pollution |
| Centrifugation | Medium | ≤75% | Large | Effective; large processing capacity | High energy consumption; noise problems |
| Froth flotation | Medium | ≤75% | Large | Simple operation; less expensive | Not suitable for high viscosity sludge; incomplete separation |
| Freeze | High | 50-75% | Small | Simple and cleaning operation | Low efficiency; geographical limitation |
| Ultrasonic | High | 50-90% | Small | Efficient; no secondary pollution | High cost of equipment; low treatment capacity |
| Microwave heating | High | ≥90% | Small | High efficiency | Specific equipment investment; high energy consumption |
| Pyrolysis | High | 50-90% | Large | Raw material adaptability; mobility; high oil yield | High operation cost; dewatering pretreatment is required; low economic value of oil product |

Many relevant studies have proved that pyrolysis is a promising and ideal choice to deal with oil sludge. The effect of temperature, heating rate, and residence time on pyrolysis behavior and the properties of pyrolysis products have been evaluated using thermogravimetric analyzer (TGA) [1-44, 1-45, 1-46] and fixed bed reactor [1-47, 1-48, 1-49]. Generally, the pyrolysis process of oil sludge can be divided into two steps: degradation of volatile compounds and decomposition of non-volatile matters. The degradation of volatile compounds mainly occurs between 150-600 °C with three sub-stages: vaporization of light hydrocarbons and remaining water (150-250 °C), desorption and thermal cracking of light and medium-molecular-weight hydrocarbons, (250-400 °C), and decomposition and cracking of heavy hydrocarbons (400-600 °C) [1-43, 1-44, 1-45]. The temperature ranges of these three stages fluctuate and overlap for oil sludge from different sources and under different heating rates. Higher heating rates and longer pyrolysis time facilitate the degradation of heavy compounds, shifting forward its corresponding temperature windows [1-46]. Noteworthy, the decomposition of heavy hydrocarbon is accompanied by many secondary reactions, such as aromatization, cyclization, polymerization, re-condensation, and carbonylation [1-45]. At higher temperatures (> 600 °C), degradation of organic fractions terminates, and the decomposition of minerals in oil sludge dominates, i.e., $CaCO_3 \rightarrow CaO + CO_2$, $K_2SO4 \rightarrow K_2O + CO_2 + 1/2O_2$ [1-50] [1-51].

Oil sludge is converted to char, oil, and gas through pyrolysis. The recovered oil contains a higher concentration of hydrocarbons with a boiling point ranging from 150 to 350 °C and can be used as an alternative for refining step or chemical production. The gas product, including $H_2$, CO, $CH_4$, $CO_2$, and $C_xH_y$, has a high possibility for commercialization and clean utilization [1-43]. During pyrolysis of oil sludge, heavy components are deposited on the surface of pyrolysis residue, known as coke [1-50]; meanwhile, a small amount of petroleum hydrocarbons remains in the solid residue after pyrolysis due to the low operation efficiency, posing threat to the environment if the solid residue is directly discharged [1-5]. Therefore, it is necessary to propose a method that can simultaneously reuse the oil sludge pyrolysis derived volatiles (oil and gas), address the potential hazards of char products, and alleviate the high energy consumption in the pyrolysis process.

## 1.4 Integrated pyrolysis and combustion of oil sludge

An integrated pyrolysis and combustion treatment has been put forward to achieve above mentioned purpose [1-5, 1-51]. As shown in **Figure 1.4**, oil sludge firstly undergoes pyrolysis and generate char, oil, and gas; the nascent char and gas products continuously enter the combustion section, making full use of their residual value and eliminating the potential hazard of residual petroleum hydrocarbons in char (discharge of char meets environmental standards). Then, the heat generated in the combustion stage can be recycled for pyrolysis treatment. This scheme has also been applied to dispose and utilize oil sand, oil shale, and coal [1-52] [1-53]. However, both pyrolysis and combustion consume energy, making this integrated thermochemical treatment an energy-intensive process [1-5]. Consequently, it is inevitable to modify this treatment, reducing energy consumption and improving its market competitiveness. Since this coupled treatment consists of two thermochemical methods, improvements can be separately implemented for the pyrolysis section and combustion section. For example, (1) the properties of oil sludge can be modified to improve its pyrolysis efficiency, (2) catalysts can be employed to improve the quality of pyrolysis products and thus enhance their secondary utilization value, and (3) substances with good combustion properties can be added to improve the heating value and combustion efficiency of char product. The former two methods can be referred to as co-pyrolysis and catalytic pyrolysis. Simplicity and effectiveness are two critical criteria when developing a technique to produce ideal synthetic liquid fuel. In this regard, co-pyrolysis of oil sludge might be the better choice for commercial application in the future because of its attractive performance and cost ratios compared to catalytic pyrolysis. Catalytic pyrolysis indeed significantly improves the quality of pyrolysis products, especially oil and gas, which, however, consumes many catalysts, causing extra economic losses. Many studies have shown that co-pyrolysis of oil sludge has significantly improved the oil quantity and quality without any improvement during system processing [1-47, 1-49]. Therefore, this work focuses on improving the integrated pyrolysis and combustion by co-pyrolysis of oil sludge and co-combustion of oil sludge char.

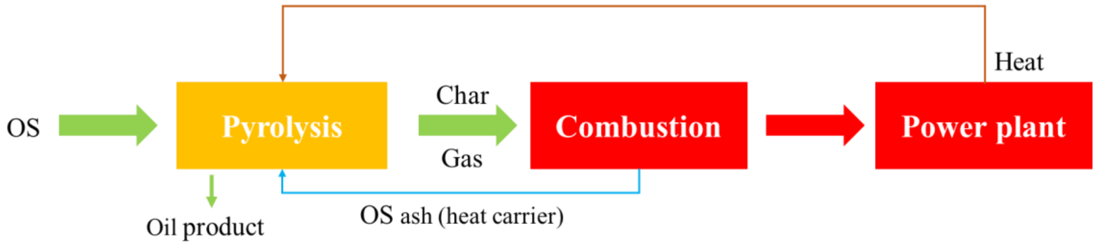

**Figure 1.4** Schematic diagram of the integrated pyrolysis and combustion treatment

### 1.4.1 Co-pyrolysis of oil sludge with other feedstocks

**Table 1.2** summarizes some present oil sludge co-pyrolysis studies. Biomass and plastics are two widely selected feedstocks. Previous work indicated that the key to the success of co-pyrolysis is the synergistic effect that comes from the reaction of different materials. Hu et al. [1-54] found that oil sludge blending improved the H/C molar ratio and higher heating value of pyrolysis oil compared to wood waste alone. Lin et al. [1-49] proposed that the synergistic effect between oil sludge and rice husk increased the aromatic and saturate hydrocarbons in oil by 55-86 % and 15-55%. Zhou et al. [1-55] conducted co-pyrolysis of oil sludge with a series of agricultural biomass including rice husk, walnut shell, and sawdust. They noticed that the co-pyrolysis process was predominantly affected by the biomass composition, such as the proportion of hemicellulose, cellulose, and lignin. The minerals in reactants were reported to contribute to the synergistic effect during co-pyrolysis. For example, the ash and alkali metals (K, Na, and Ca) in biomass can catalytically promote the pyrolysis process, and the metal oxides in oil sludge such as $Fe_3O_4$, CaO, and $Al_2O_3$ can also enhance the conversion of char to volatiles [1-47] (Zhu 2020). Milato et al. [1-48, 1-57] observed that adding polyolefins (HDPE, LDPE, and PP) increased the yields of paraffinic products and improved the light fractions in oil.

**Table 1.2** A brief review of co-pyrolysis of oil sludge and other feedstocks

| Type of oil sludge | Additives | Temperature (°C) | Pyrolysis reactors | Results | References |
|---|---|---|---|---|---|
| Tank bottom sludge | Wood waste | 400-600 | TGA; Fixed bed tube furnace reactor | ➢ OS derived oil has better properties and has a great potential for fuel source.<br>➢ OS blending improved the H/C ratio and HHV of pyrolysis oil comparing to wood derived bio-oil. | [1-54]. |
| Tank bottom sludge | Rice husk | 600 | Horizontal fixed-bed reactor | ➢ The synergistic effect between OS and rice husk increased the aromatic and saturate content in oil by 55–86% and 15–55%.<br>➢ Catalytic effect of ash and alkali metals derived from biomass, promoting the secondary reactions of liquid products. | [1-49]. |
| Tank bottom sludge | Agricultural biomass: rice husk, walnut shell, sawdust, | 500-800 | TGA; Horizontal quartz reactor | ➢ The presence of biomass reduced the activation energy during pyrolysis of OS, favoring energy conservation.<br>➢ Biomass components (hemicellulose, cellulose, and lignin) affected the co-pyrolysis process. | [1-55]. |
| Oilfield sludge | Microalgae residue | 600 | TGA; Tube furnace reactor | ➢ Microalgae residue addition increased the oil content by suppressing the secondary cracking of heavy hydrocarbons to form gas products.<br>➢ Minerals in microalgae residue (Ca, K, and Fe) might play a vital catalytic effect in the OS pyrolysis, affecting the product distribution. | [1-56]. |
| Refinery sludge | Sawdust | 500-900 | TG-MS; Fixed bed reactor | ➢ Sawdust addition promoted the increase of gas yield ($H_2$ and CO).<br>➢ Sawdust addition increased the carbon content and enhanced the reduction of minerals, for example, the $Fe_3O_4$ in solid was reduced by carbon with the generation of CO and $CO_2$, leading to the increase of gas yields. | [1-47]. |
| Tank bottom sludge | Polyolefins (HDPE, LDPE, and PP) | 450 | Fixed bed reactor | ➢ Polyolefins addition increased the paraffinic products in oil.<br>➢ However, the tertiary carbons in polyolefins inevitably yielded heavier hydrocarbons, requiring catalytic section for oil upgrading. | [1-48] and [1-57]. |

It could be noted that previous studies prefer choosing biomass as additives for co-pyrolysis with oil sludge due to its abundant, renewable, and carbon-neutral characteristics. For the ash-rich oil sludge, such as the oilfield sludge used in this work, the addition of biomass can remedy the lack of organic substances in oil sludge to promote the pyrolysis efficiency; lead to enhanced production of volatiles (oil and gas), and increase the carbon content in char product, thereby improving the recycling value of pyrolysis products. Plastics and oil sludge are both crude oil-derived matters, and plastic addition can significantly increase the yield of pyrolysis oil. Still, heavy fractions are accumulated in oil, requiring secondary cracking such as employing catalysts in the pyrolysis process [1-57].

### 1.4.2 Co-combustion of oil sludge char with biomass

Biomass, one of the leading renewable energy resources, has attracted worldwide attention. Through proper utilization, biomass can act as an alternative fuel and play a supplementary role in meeting the world's energy demand [1-58]. Combustion is the most efficient and sustainable technology among biomass utilization methods due to its high reactivity and carbon-neutral characteristic [1-59]. Many researchers have conducted systematic techno-economic analyses on the co-combustion of coal and biomass [1-60]. These results confirmed the vast potential of biomass in replacing fossil fuel as an energy source. Given these aspects, co-combustion of biomass and other solid waste is a promising measurement for waste treatment, especially for the wastes with high ash content and cannot be directly landfilled, during which these wastes could be effectively disposed of, and their additional values could be recovered. Previous studies pointed out that biomass blending could effectively improve the combustion properties of oil sludge char. Gong et al. [1-61] and Wang et al. [1-62] studied co-combustion of oil sludge char with microalgae residues. Their results demonstrated that the addition of microalgae residues increased the volatile content, promoted the combustion property of oil sludge char, and reduced heavy metal ecotoxicity in combustion fly ash. Moreover, $SO_2$ emission from the co-combustion was decreased due to the catalytic cracking effect of metal and metal oxides in OSC.

## 1.5 Research gaps in pyrolysis/combustion of oil sludge/oil sludge char

According to current related studies, biomass addition can significantly promote the c-processing efficiency and the synergy between oil sludge and biomass improves the quality of products. However, there still exist some research gaps in co-pyrolysis of oil sludge and biomass, and co-combustion of oil sludge char and biomass:

(1) The quality of oil sludge and biomass co-pyrolysis-derived oil needs further improvement. Biomass addition significantly increases pyrolysis oil yield compared to oil sludge alone. However, the oil still contains a relatively high concentration of oxygenates, rendering it corrosive and chemically unstable, thus limiting the large-scale commercial application. Few studies have been carried out to further improve the quality of oil obtained from co-pyrolysis of oil sludge and biomass.

(2) The synergistic behavior during oil sludge and biomass co-pyrolysis is understudied. The organic components in oil sludge are mainly petroleum hydrocarbons, while those in biomass are mainly oxygenates, entailing interactions between oil sludge-derived hydrocarbon intermediates and biomass-derived oxygen-containing radicals. Previous studies mainly conducted co-pyrolysis of oil sludge and specific biomass and speculated the synergistic effect based on the properties of pyrolysis products. However, biomass composition is complex, and the proportion of basic components (mainly hemicellulose, cellulose, and lignin) varies among biomass from different sources. Therefore, it is meant to carry out studies on co-pyrolysis of oil sludge of biomass with typical characteristics.

(3) The co-combustion mechanism of oil sludge char and biomass remains for further investigation. Current research on co-combustion of oil sludge char and biomass is limited to raw biomass utilization to improve the combustion characteristics of oil sludge char. The interactive mechanisms of oil sludge char and biomass co-combustion, such as the nature of synergy/inhibition during the co-combustion of oil sludge char

and biomass, are still uncertain. Furthermore, the alkali metals in biomass could also act as catalysts during co-combustion in addition to causing fouling and slagging problems. Therefore, the effect of alkali metals on the co-combustion mechanism should be evaluated. Moreover, kinetic analysis of oil sludge char and biomass co-combustion is still weak and requires in-depth inspection.

## 1.6 Objective of present work

The main objective of this study is to investigate the interactions, kinetics, and mechanisms during co-pyrolysis/co-combustion of oil sludge/oil sludge char and biomass. Two widely used thermochemical pretreatments are employed to modify biomass without the consumption of chemicals. Torrefaction, a mild pyrolysis process operating between 200-300 °C at a low heating rate, is an effective pretreating method to alter the physicochemical properties of biomass, after which the content of holocellulose (hemicellulose and cellulose) decreases while lignin content gets an increase [1-63]. Moreover, the oxygenated compounds in pyrolysis oil of torrefied biomass are significantly reduced. Therefore, torrefaction pretreatment is firstly conducted to (1) further promote hydrocarbon production in pyrolysis oil and (2) support analyzing the synergistic behavior during pyrolysis of oil sludge and typical biomass components (hemicellulose, cellulose, and lignin).

Hydrothermal treatment (HTT), which is defined as a treatment of biomass in hot compressed water at temperatures within 180-260°C (also referred to as hydrothermal carbonization in this temperature range), has been regarded as a promising and environmentally acceptable method to upgrade biomass [1-64]. The hydrochars, generated by HTT, exhibit ameliorated homogeneity and higher fuel properties than raw biomass, such as lower oxygen content, higher carbon content, higher calorific values, and enhanced reactivity [1-65]. On the other hand, most alkali metals are removed during HTT [1-66]. The problems (fouling and slagging) can be avoided or significantly mitigated, which also assists in evaluating the effect of alkali metals in the co-combustion of oil sludge char and biomass.

Above all, the work of this study includes: (1) investigate the effect of torrefaction on the morphological structure evolution and pyrolysis reactivity of biomass; (2) conduct co-pyrolysis of oil sludge and raw/torrefied biomass to enhance hydrocarbon production as well as evaluating the co-pyrolysis synergistic behavior among oil sludge and model biomass components; and (3) co-combustion of oil sludge char and raw/hydrothermally treated biomass are performed to promote combustion efficiency and evaluate the effect of alkali metals on co-combustion interactions, kinetics, and mechanisms.

## 1.7 Outline of the thesis

This thesis consists of 5 chapters and the details of each chapter are as follows:

### Chapter 1: Introduction

In this chapter, the background of this thesis is explained. The classification, characterization, and hazards of oil sludge are listed. Then, the oil sludge treatment methods are briefly introduced. It could be summarized that the pyrolysis technique has the advantage of good sample adaptability compared to other methods. Finally, the research gaps in existing studies and the research objectives of this work are clarified.

### Chapter 2: Effect of torrefaction on the structure and pyrolysis reactivity of rice straw

In **Chapter 2**, rice straw, a typical agricultural biomass waste, underwent torrefaction at 200, 250, and 300 °C. After torrefaction, the proportion of hemicellulose, cellulose, and lignin was significantly altered, where severe torrefaction (300 °C) resulted in lignin enrichment. Consequently, torrefaction led to enhancement in surface aromaticity and reduction in crystallinity. Thermogravimetric results indicated that severe torrefaction increased rice straw's main decomposition temperature range and weakened the pyrolysis reactivity as regarding the lowered comprehensive pyrolysis index. Torrefaction altered the pyrolysis pathway of rice straw to enhance char production and inhibit volatile (oil and gas) generation. Nonetheless, the hydrocarbon concentration in oil significantly increased.

**Chapter 3: Effect of torrefaction on synergistic behavior during co-pyrolysis of oil sludge with rice straw to enhance hydrocarbon production**

The physicochemical properties of rice straw before and after torrefaction were already characterized in **Chapter 2**. In **Chapter 3**, torrefied rice straw was continuously incorporated into co-pyrolysis with oil sludge to assist evaluating the pyrolysis synergistic effect between oil sludge and rice straw. Co-pyrolysis of oil sludge and rice straw yielded a synergistic impact on gas production and promoted char conversion to volatiles. The co-pyrolysis significantly promoted the formation of alkanes and olefins while suppressing the generation of oxygenates in oil. The incorporation of torrefied rice straw into co-pyrolysis yielded a positive synergistic effect on oil generation and further enhanced the production of alkanes and olefins. In addition, heavy-weight straight-chain alkanes were observed from co-pyrolysis of oil sludge and torrefied rice straw.

**Chapter 4: Co-combustion of oil sludge char with raw/hydrothermally treated biomass: interactions, kinetics, and mechanisms**

**Chapter 2** and **Chapter 3** demonstrated that biomass addition yielded higher oil production than oil sludge pyrolysis alone, and a positive synergistic effect was witnessed in hydrocarbon production, representing improved quality. This chapter aims at the disposal of oil sludge pyrolysis residue (char), simultaneously recycling its remaining economic value. Cherry blossom wood incorporation increased the combustion property and efficiency of oil sludge char regarding the values of several combustion indexes. Wood blending with oil sludge char resulted in negative interactions due to the inhibited diffusion of volatiles. The hydrothermal treatment developed porous structure of raw wood, promoting the gas diffusion and heat transfer; thereby its addition into oil sludge char yielded positive interaction. Moreover, diffusion models were the most efficient kinetic models for oil sludge char/raw wood combustion, while chemical reactions were found to be the rate-determining steps for oil sludge char/hydrothermally treated wood combustion. The interactions between raw/hydrothermally treated wood and oil sludge char resulted in opposite variation trend of apparent activation energies compared to individual biomass. The catalytic effect of inorganic elements and their physical influence on heat and mass transfer can control the co-combustion performance of oil sludge char and biomass.

### Chapter 5: Conclusions and recommendations

This chapter summarizes the important findings on co-pyrolysis/co-combustion of oil sludge/oil sludge char and biomass. In addition, practical implications of this research and recommendations for future work are provided.

The relationship between each chapter is illustrated in **Figure 1.5**:

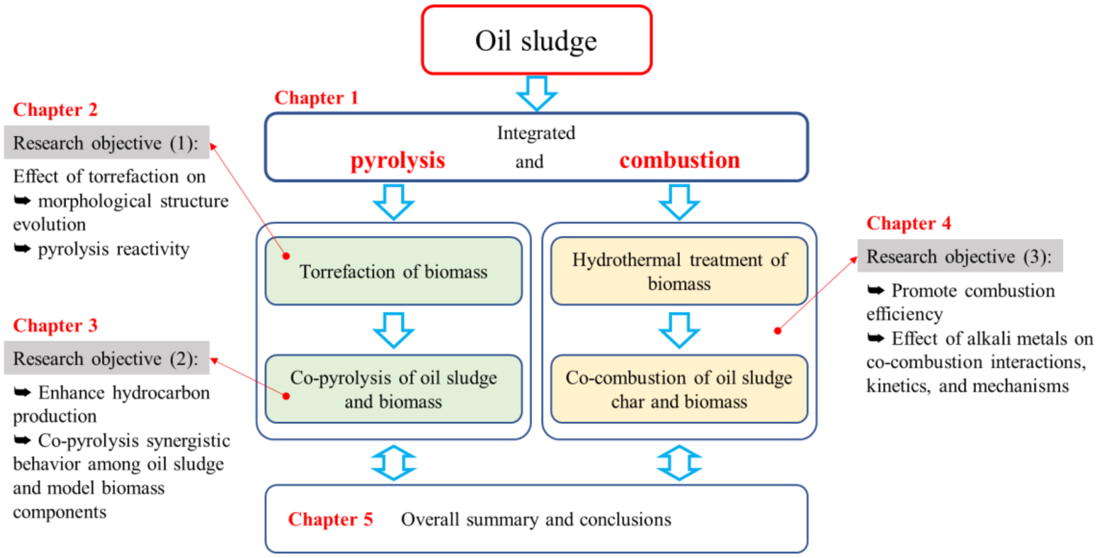

**Figure 1.5** The thesis contents and their relationship

## References

[1-1] Dimitriou, I., Goldingay, H., & Bridgwater, A. V. (2018). Techno-economic and uncertainty analysis of Biomass to Liquid (BTL) systems for transport fuel production. Renewable and sustainable energy reviews, 88, 160-175.

[1-2] Xu, N., Wang, W., Han, P., & Lu, X. (2009). Effects of ultrasound on oily sludge deoiling. Journal of hazardous materials, 171(1-3), 914-917.

[1-3] Li, J., Lin, F., Li, K., Zheng, F., Yan, B., Che, L., ... & Yoshikawa, K. (2021). A critical review on energy recovery and non-hazardous disposal of oily sludge from petroleum industry by pyrolysis. Journal of Hazardous Materials, 406, 124706.

[1-4] Hu, G., Li, J., & Zeng, G. (2013). Recent development in the treatment of oily sludge from petroleum industry: a review. Journal of hazardous materials, 261, 470-490.

[1-5] Cheng, S., Wang, Y., Fumitake, T., Kouji, T., Li, A., & Kunio, Y. (2017). Effect of steam and oil sludge ash additive on the products of oil sludge pyrolysis. Applied Energy, 185, 146-157.

[1-6] BP, BP Statistical Review of World Energy 2019, London, 2019, p. 17, 27.

[1-7] da Silva, L. J., Alves, F. C., & de França, F. P. (2012). A review of the technological solutions for the treatment of oily sludges from petroleum refineries. Waste Management & Research, 30(10), 1016-1030.

[1-8] National Bureau of Statistics. 2021 China Statistical Yearbook, 2021: China Statistics Press.

[1-9] Ma, Z., Xie, J., Gao, N., & Quan, C. (2019). Pyrolysis behaviors of oilfield sludge based on Py-GC/MS and DAEM kinetics analysis. Journal of the Energy Institute, 92(4), 1053-1063.

[1-10] Wang, Y., Dong, B., Fan, Y., Hu, Y., Zhai, X., Deng, C., ... & Dai, X. (2019). Nitrogen transformation during pyrolysis of oilfield sludge with high polymer content. Chemosphere, 219, 383-389.

[1-11] Hickenbottom, K. L., Hancock, N. T., Hutchings, N. R., Appleton, E. W., Beaudry, E. G., Xu, P., & Cath, T. Y. (2013). Forward osmosis treatment of drilling mud and fracturing wastewater from oil and gas operations. Desalination, 312, 60-66.

[1-12] De-qing, S., Jian, Z., Zhao-long, G., Jian, D., Tian-li, W., Murygina, V., & Kalyuzhnyi, S. (2007). Bioremediation of oil sludge in Shengli oilfield. Water, air, and

soil pollution, 185(1), 177-184.

[1-13] Gallego, J. L. R., García-Martínez, M. J., Llamas, J. F., Belloch, C., Peláez, A. I., & Sánchez, J. (2007). Biodegradation of oil tank bottom sludge using microbial consortia. Biodegradation, 18(3), 269-281.

[1-14] Liu, J., Jiang, X., Zhou, L., Han, X., & Cui, Z. (2009). Pyrolysis treatment of oil sludge and model-free kinetics analysis. Journal of hazardous materials, 161(2-3), 1208-1215.

[1-15] Mansur, A. A., Adetutu, E. M., Kadali, K. K., Morrison, P. D., Nurulita, Y., & Ball, A. S. (2014). Assessing the hydrocarbon degrading potential of indigenous bacteria isolated from crude oil tank bottom sludge and hydrocarbon-contaminated soil of Azzawiya oil refinery, Libya. Environmental Science and Pollution Research, 21(18), 10725-10735.

[1-16] Koolivand, A., Abtahi, H., Godini, K., Saeedi, R., Rajaei, M. S., & Parhamfar, M. (2019). Biodegradation of oil tank bottom sludge using a new two-phase composting process: Kinetics and effect of different bulking agents. Journal of Material Cycles and Waste Management, 21(6), 1280-1290.

[1-17] Roy, A., Dutta, A., Pal, S., Gupta, A., Sarkar, J., Chatterjee, A., ... & Kazy, S. K. (2018). Biostimulation and bioaugmentation of native microbial community accelerated bioremediation of oil refinery sludge. Bioresource technology, 253, 22-32.

[1-18] Marin, J. A., Hernandez, T., & Garcia, C. (2005). Bioremediation of oil refinery sludge by landfarming in semiarid conditions: Influence on soil microbial activity. Environmental research, 98(2), 185-195.

[1-19] Marín, J. A., Moreno, J. L., Hernandez, T., & García, C. (2006). Bioremediation by composting of heavy oil refinery sludge in semiarid conditions. Biodegradation, 17(3), 251-261.

[1-20] Ramaswamy, B., Kar, D. D., & De, S. (2007). A study on recovery of oil from sludge containing oil using froth flotation. Journal of environmental management, 85(1),

150-154.

[1-21] Azim, A. A. A. A., Abdul-Raheim, A. R. M., Kamel, R. K., & Abdel-Raouf, M. E. (2011). Demulsifier systems applied to breakdown petroleum sludge. Journal of Petroleum Science and Engineering, 78(2), 364-370.

[1-22] McLean, J. D., & Kilpatrick, P. K. (1997). Effects of asphaltene solvency on stability of water-in-crude-oil emulsions. Journal of colloid and interface science, 189(2), 242-253.

[1-23] Speight, J. G. (2006). The chemistry and technology of petroleum. CRC press.

[1-24] Chavan, S., Kini, H., & Ghosal, R. (2012). Process for sulfur reduction from high viscosity petroleum oils. International Journal of Environmental Science and Development, 3(3), 228.

[1-25] Da Rocha, O. R. S., Dantas, R. F., Duarte, M. M. M. B., Duarte, M. M. L., & Da Silva, V. L. (2010). Oil sludge treatment by photocatalysis applying black and white light. Chemical Engineering Journal, 157(1), 80-85.

[1-26] Admon, S., Green, M., & Avnimelech, Y. (2001). Biodegradation kinetics of hydrocarbons in soil during land treatment of oily sludge. Biorernediation Journal, 5(3), 193-209.

[1-27] Robertson, S. J., McGill, W. B., Massicotte, H. B., & Rutherford, P. M. (2007). Petroleum hydrocarbon contamination in boreal forest soils: a mycorrhizal ecosystems perspective. Biological reviews, 82(2), 213-240.

[1-28] Al-Mutairi, N., Bufarsan, A., & Al-Rukaibi, F. (2008). Ecorisk evaluation and treatability potential of soils contaminated with petroleum hydrocarbon-based fuels. Chemosphere, 74(1), 142-148.

[1-29] Wake, H. (2005). Oil refineries: a review of their ecological impacts on the aquatic environment. Estuarine, Coastal and Shelf Science, 62(1-2), 131-140.

[1-30] Liu, T., Wang, J., Yang, J., Huang, Q., Chi, Y., & Yan, J. (2017). Contamination

of fresh water by petroleum sludge. Petroleum Science and Technology, 35(4), 413-418.

[1-31] Wang, S. J., Yan, Z. G., Guo, G. L., Lu, G. L., Wang, Q. H., & Li, F. S. (2010). Ecotoxicity assessment of aged petroleum sludge using a suite of effects-based end points in earthworm Eisenia fetida. Environmental monitoring and assessment, 169(1), 417-428.

[1-32] Sankaran, S., Pandey, S., & Sumathy, K. (1998). Experimental investigation on waste heat recovery by refinery oil sludge incineration using fluidised-bed technique. Journal of Environmental Science & Health Part A, 33(5), 829-845.

[1-33] Ramaswamy, B., Kar, D. D., & De, S. (2007). A study on recovery of oil from sludge containing oil using froth flotation. Journal of environmental management, 85(1), 150-154.

[1-34] Taiwo, E. A., & Otolorin, J. A. (2009). Oil recovery from petroleum sludge by solvent extraction. Petroleum Science and Technology, 27(8), 836-844.

[1-35] Ávila-Chávez, M. A., Eustaquio-Rincón, R., Reza, J., & Trejo, A. (2007). Extraction of hydrocarbons from crude oil tank bottom sludges using supercritical ethane. Separation Science and technology, 42(10), 2327-2345.

[1-36] Li, W., Lin, H., Yang, Y., Shang, Z., Li, Q., Ma, Y., ... & Jiang, M. (2021). Enhanced Separation of Oil and Solids in Oily Sludge by Froth Flotation at Normal Temperature. Processes, 9(12), 2163.

[1-37] Mao, F., Han, X., Huang, Q., Yan, J., & Chi, Y. (2016). Effect of frequency on ultrasound-assisted centrifugal dewatering of petroleum sludge. Drying Technology, 34(16), 1948-1956.

[1-38] Gomez, V., Wright, K., Esquenazi, G. L., & Barron, A. R. (2019). Microwave treatment of a hot mill sludge from the steel industry: en route to recycling an industrial waste. Journal of Cleaner Production, 207, 182-189.

[1-39] Elektorowicz, M., & Muslat, Z. (2008). Removal of heavy metals from oil sludge

using ion exchange textiles. Environmental technology, 29(4), 393-399.

[1-40] Hu, G., Li, J., & Hou, H. (2015). A combination of solvent extraction and freeze thaw for oil recovery from petroleum refinery wastewater treatment pond sludge. Journal of hazardous materials, 283, 832-840.

[1-41] Jean, D. S., Chu, C. P., & Lee, D. J. (2001). Freeze/thaw treatment of oily sludge from petroleum refinery plant. Separation science and technology, 36(12), 2733-2746.

[1-42] Zhang, S., Yan, Y., Li, T., & Ren, Z. (2005). Upgrading of liquid fuel from the pyrolysis of biomass. Bioresource technology, 96(5), 545-550.

[1-43] Chang, C. Y., Shie, J. L., Lin, J. P., Wu, C. H., Lee, D. J., & Chang, C. F. (2000). Major products obtained from the pyrolysis of oil sludge. Energy & Fuels, 14(6), 1176-1183.

[1-44] Cheng, S., Chang, F., Zhang, F., Huang, T., Yoshikawa, K., & Zhang, H. (2018). Progress in thermal analysis studies on the pyrolysis process of oil sludge. Thermochimica acta, 663, 125-136.

[1-45] Wang, Z., Guo, Q., Liu, X., & Cao, C. (2007). Low temperature pyrolysis characteristics of oil sludge under various heating conditions. Energy & fuels, 21(2), 957-962.

[1-46] Qu, Y., Li, A., Wang, D., Zhang, L., & Ji, G. (2019). Kinetic study of the effect of in-situ mineral solids on pyrolysis process of oil sludge. Chemical Engineering Journal, 374, 338-346.

[1-47] Zhu, J., Zhu, L., Guo, D., Chen, Y., Wang, X., & Zhu, Y. (2020). Co-pyrolysis of petrochemical sludge and sawdust for syngas production by TG-MS and fixed bed reactor. International Journal of Hydrogen Energy, 45(55), 30232-30243.

[1-48] Milato, J. V., Franca, R. J., & Calderari, M. R. M. (2020). Co-pyrolysis of oil sludge with polyolefins: Evaluation of different Y zeolites to obtain paraffinic products. Journal of Environmental Chemical Engineering, 8(3), 103805.

[1-49] Lin, B., Huang, Q., & Chi, Y. (2018). Co-pyrolysis of oily sludge and rice husk for improving pyrolysis oil quality. Fuel processing technology, 177, 275-282.

[1-50] Gong, Z., Liu, C., Wang, M., Wang, Z., & Li, X. (2020). Experimental study on catalytic pyrolysis of oil sludge under mild temperature. Science of the Total Environment, 708, 135039.

[1-51] Wang, Z., Gong, Z., Wang, Z., Fang, P., & Han, D. (2018). A TG-MS study on the coupled pyrolysis and combustion of oil sludge. Thermochimica acta, 663, 137-144.

[1-52] Jiang, X. M., Han, X. X., & Cui, Z. G. (2007). New technology for the comprehensive utilization of Chinese oil shale resources. Energy, 32(5), 772-777.

[1-53] Golubev, N. (2003). Solid oil shale heat carrier technology for oil shale retorting. Oil Shale, 20(3), 324-332.

[1-54] Hu, J., Gan, J., Li, J., Luo, Y., Wang, G., Wu, L., & Gong, Y. (2017). Extraction of crude oil from petrochemical sludge: characterization of products using thermogravimetric analysis. Fuel, 188, 166-172.

[1-55] Zhou, X., Jia, H., Qu, C., Fan, D., & Wang, C. (2017). Low-temperature co-pyrolysis behaviours and kinetics of oily sludge: effect of agricultural biomass. Environmental technology, 38(3), 361-369.

[1-56] Wang, Z., Gong, Z., Wang, W., & Zhang, Z. (2020). Study on combustion characteristics and the migration of heavy metals during the co-combustion of oil sludge char and microalgae residue. Renewable Energy, 151, 648-658.

[1-57] Milato, J. V., França, R. J., Rocha, A. S., & Calderari, M. R. M. (2020). Catalytic co-pyrolysis of oil sludge with HDPE to obtain paraffinic products over HUSY zeolites prepared by dealumination and desilication. Journal of Analytical and Applied Pyrolysis, 151, 104928.

[1-58] Saidur, R., BoroumandJazi, G., Mekhilef, S., & Mohammed, H. A. (2012). A review on exergy analysis of biomass based fuels. Renewable and Sustainable Energy

Reviews, 16(2), 1217-1222.

[1-59] Sahu, S. G., Chakraborty, N., & Sarkar, P. (2014). Coal–biomass co-combustion: An overview. Renewable and Sustainable Energy Reviews, 39, 575-586.

[1-60] Mandegari, M., Farzad, S., & Görgens, J. F. (2018). A new insight into sugarcane biorefineries with fossil fuel co-combustion: Techno-economic analysis and life cycle assessment. Energy Conversion and Management, 165, 76-91.

[1-61] Gong, Z., Wang, Z., Wang, Z., Fang, P., & Meng, F. (2019). Study on the migration characteristics of nitrogen and sulfur during co-combustion of oil sludge char and microalgae residue. Fuel, 238, 1-9.

[1-62] Wang, Z., Gong, Z., Wang, W., & Zhang, Z. (2020). Study on combustion characteristics and the migration of heavy metals during the co-combustion of oil sludge char and microalgae residue. Renewable Energy, 151, 648-658.

[1-63] Dai, L., Wang, Y., Liu, Y., Ruan, R., He, C., Yu, Z., ... & Tian, X. (2019). Integrated process of lignocellulosic biomass torrefaction and pyrolysis for upgrading bio-oil production: A state-of-the-art review. Renewable and Sustainable Energy Reviews, 107, 20-36.

[1-64] Bach, Q. V., Tran, K. Q., Khalil, R. A., Skreiberg, Ø., & Seisenbaeva, G. (2013). Comparative assessment of wet torrefaction. Energy & Fuels, 27(11), 6743-6753.

[1-65] Bach, Q. V., Tran, K. Q., Skreiberg, Ø., Khalil, R. A., & Phan, A. N. (2014). Effects of wet torrefaction on reactivity and kinetics of wood under air combustion conditions. Fuel, 137, 375-383.

[1-66] Parshetti, G. K., Quek, A., Betha, R., & Balasubramanian, R. (2014). TGA–FTIR investigation of co-combustion characteristics of blends of hydrothermally carbonized oil palm biomass (EFB) and coal. Fuel processing technology, 118, 228-234.

# Chapter 2 Effect of torrefaction on the structure and pyrolysis property of rice straw

## 2.1 Introduction

The shortage of fossil fuels and the issue of global climate change necessitate the development of renewable and sustainable resources to replace fossil fuels. Among the alternatives, biomass is considered a good alternative due to its abundance, low cost, and eco-friendly characteristics, which have been extensively investigated. Among multiple utilization approaches of biomass, pyrolysis is an efficient method for converting biomass into liquid oil, gas, and char [2-1]. The liquid oil can potentially be employed as a substitute for conventional fuels after deoxygenation. High oxygen content in biomass pyrolysis oil renders it corrosive and chemically unstable, thus limiting the direct large-scale commercial application of pyrolysis technology [2-2]. Reducing bio-oil oxygenates via pretreatment is an efficient method to alleviate these undesirable properties [2-3].

Torrefaction is frequently used for upgrading biomass wastes to obtain solid biofuel. This moderate thermal process improves biomass's grindability, energy density, and hydrophobicity [2-4, 2-5]. It is well known that deoxygenation of biomass is the crucial goal of torrefaction pretreatment, and several reactions, like dehydration, decarboxylation, and decarbonylation, occur during this process [2-6, 2-7]. Consequently, the hydrocarbon content is selectively increased, improving bio-oil quality. Sabil et al. [2-8] found the oxygen content of palm skin and shell decreased from 47 to 38% and 50 to 43% after torrefaction at 300 °C, respectively. Chen et al. [2-4] reported that the oxygen content of cotton stalk decreased from 37.2 to 17.5% as torrefaction temperature increased from 0 to 280 °C, resulting in the reduction of water and acid contents in bio-oil. Zheng et al. [2-9] carried out torrefaction of pine wood at 240 – 320 °C and reported improvements in aromaticity, heating value, and bio-oil density.

In China, rice straw (RS) is widely generated but is usually directly abandoned and burned, causing tremendous environmental concerns. After proper processing, this agricultural waste can be converted into value-added biofuel. Accordingly, this chapter characterizes RS's morphological structure evolution and pyrolysis property under different torrefaction conditions, the structure of Chapter 2 is illustrated in **Figure 2.1**. The microstructure of rice straw before and after torrefaction was analyzed via Fourier transform infrared (FTIR) spectrometer, X-ray diffraction (XRD) pattern, and Scanning electron microscopy (SEM). The pyrolysis behavior was measured by a thermogravimetric (DTG) analyzer. The composition of oil products was determined by a gas chromatography-mass spectrometer (GC-MS). Finally, the effect of torrefaction on pyrolysis reactivity and oil properties of rice straw was discussed.

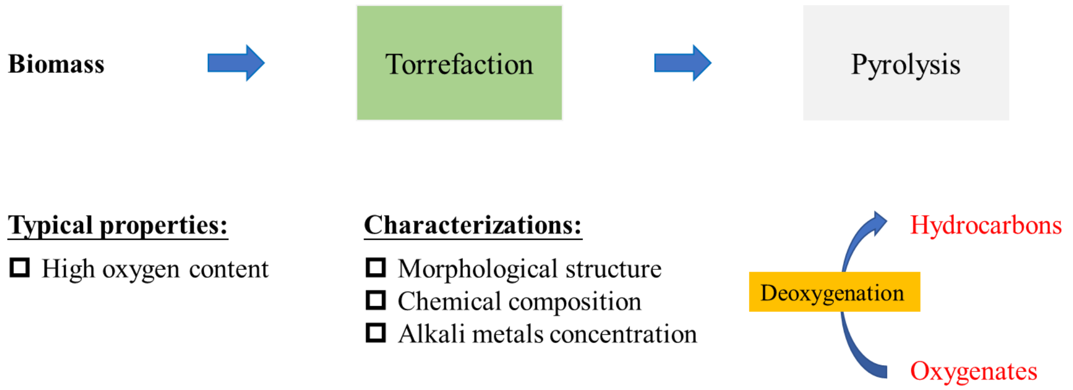

**Figure 2.1** Structure of Chapter 2.

## 2.2 Materials and methods

### 2.2.1 Materials and torrefaction pretreatment

The RS sample was purchased from a gardening market in Japan. As-received samples were firstly dried in an oven at 105 °C for 24 h, then milled and sieved smaller than 180 μm. Torrefied rice straw (TS) samples were obtained by torrefaction of RS in a laboratory-scale fixed bed reactor as described in **Figure 2.2**. Before torrefaction, around 10 g sample was put in a hanging basket (quartz material) and placed in the heating area; $N_2$ was then fed into the reactor with a flow rate of 300 mL/min for 10 min to create an air-free environment; thereafter, the reactor was heated from zoom temperature to 200, 250, and 300 °C and kept for 30 min, respectively. Torrefaction experiments at each temperature were repeated four times, and the solid residue obtained from each run was mixed for subsequent analysis. Torrefied samples were tagged as TS200, TS250, and TS300 representing TS received at each target temperature.

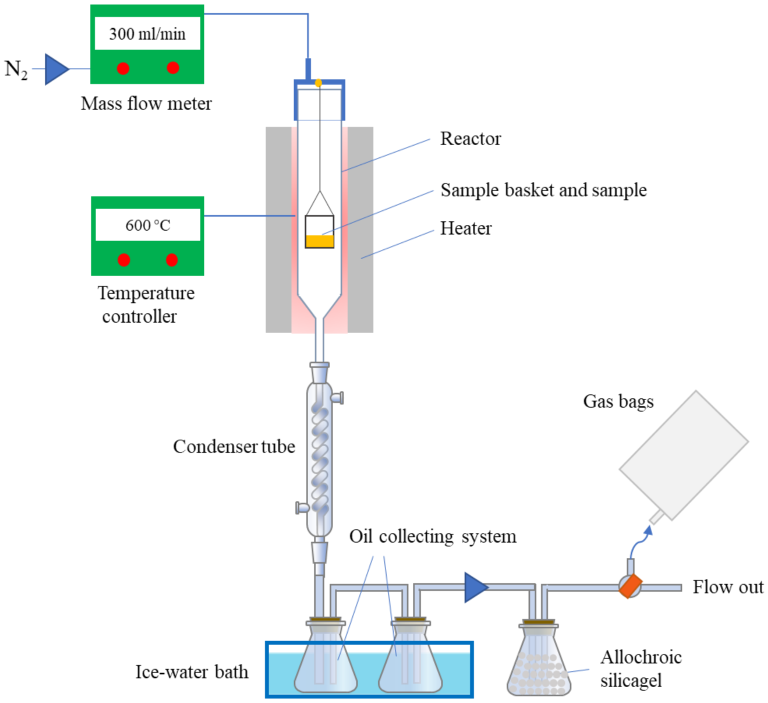

**Figure 2.2** Schematic diagram of the fixed bed reactor for torrefaction.

### 2.2.2 Characterization of RS and TS

The proximate analysis of samples was measured by a muffle furnace according to GB/T212-2008. The ultimate analysis was conducted by an elemental analyzer (Vario Microcube, Bruker, Germany), and the obtained results were used to calculate the higher heating value (HHV) via **eq 1** [2-10]:

$$\mathrm{HHV} = 357.8C + 1135.6H + 54.9N + 119.5S - 85.4O - 974 \tag{1}$$

Where C, H, N, S, and O represent the weight percentages of carbon, hydrogen, nitrogen, sulfur, and oxygen, respectively. The biochemical analysis of RS and TS (contents of hemicellulose, cellulose, and lignin) were determined according to the Van Soest method [2-11]. All these above results are listed in **Table 2.1**. The ash composition of RS and TS was determined using X-ray fluorescence spectrometry (XRF; S2 Ranger Bruker, Japan) analysis with X-ray tube of palladium anode and the results are tabulated in **Table 2.2**. Morphological surface characteristics of RS and TS were determined by scanning electron microscopy (SEM; JSM-6610LA, JEOL, Japan) with an acceleration voltage of 5 kV. The alkali metals concentration of RS and TS was measured with an inductively coupled plasma optical emission spectrometerit speculate (ICP-AES; ICPE-9000, Shimadzu, Japan). Powder X-ray diffraction analysis (XRD; Bruker D8, Japan) was performed to identify the crystalline structure of RS and TS with Cu Kα radiation in the scanning range of 2θ = 10 - 80°. To investigate the effect of torrefaction on the crystallinity of samples, crystallinity index (CrI) was calculated by **eq 2** [2-12]:

$$\mathrm{CrI} = \frac{I_{002} - I_{am}}{I_{002}} \tag{2}$$

Where $I_{002}$ (at 2θ around 22 °) is the maximum peak intensity, representing the crystal part of the sample, while $I_{am}$ (at 2θ around 18 °) is the minimum intensity, representing the amorphous part.

The functional groups of RS and TS were measured by an ATR-FTIR analyzer. The Fourier-transformed infrared (FTIR) spectra were measured from a collection of 32 scans per spectrum at a resolution of 4 $\mathrm{cm^{-1}}$ in the range of 4000 to 400 $\mathrm{cm^{-1}}$. Semi-quantitative analysis was performed with the integrated area (IA) from FTIR spectrum to further measure the macromolecular structure of RS and TS. A-factor, $CH_2/CH_3$, and $A_{ar}/A_{al}$ were calculated by the peak integrated area. The relevant equations are as follows:

$$\mathrm{A\text{-}factor} = (\mathrm{IA3000 - 2800cm^{-1}})/(\mathrm{IA3000 - 2800cm^{-1}} + \mathrm{IA1650 - 1520cm^{-1}}) \tag{3}$$

$$CH_2/CH_3 = (\mathrm{IA2920} + \mathrm{IA2860cm^{-1}})/(\mathrm{IA2950} + \mathrm{IA2890cm^{-1}}) \tag{4}$$

$$A_{ar}/A_{al} = (\mathrm{IA1650 - 1520cm^{-1}})/(\mathrm{IA3000 - 2800cm^{-1}}) \tag{5}$$

Where A-factor represents the hydrocarbon-generating potential, $CH_2/CH_3$ represents the length of aliphatic length, and $A_{ar}/A_{al}$ represents the aromaticity of samples.

### 2.2.3 Experimental apparatus and method

Thermogravimetric analysis of samples was conducted by a thermogravimetric analyzer (TG-DTA; TA-60WS, Shimadzu, Japan). For each run, around 10 mg sample of RS and TS was heated from 30 to 900 °C under a nitrogen gas flow rate of 100 ml/min. The heating rate was controlled at 20 °C/min.

Three typical temperature parameters, ignition temperature ($T_i$), burnout temperature ($T_b$), and peak temperature ($T_{max}$) were obtained from the thermogravimetry and differential thermogravimetry (TG-DTG) curves for pyrolysis performance analysis. The tangent method was employed to determine $T_i$ [2-13]. $T_b$ and $T_{max}$ corresponded to the temperature at 98% conversion rate and the maximum weight loss rate, respectively [2-14]. Three indexes, the ignition index ($D_i$), burnout index ($D_b$), and comprehensive pyrolysis index (CPI) were calculated to evaluate the pyrolysis properties of samples. These indexes were determined by **eqs 6-8** [2-15]:

$$D_i = \frac{-R_p}{t_i \times t_p} \tag{6}$$

$$D_b = \frac{-R_p}{\Delta t_{1/2} \times t_p \times t_b} \tag{7}$$

$$CPI = \frac{(-R_p) \times (-R_{mean})}{T_i^2 \times T_b} \tag{8}$$

where $R_p$ denotes the maximum weight loss rate (unit: %/min), $R_{mean}$ denotes the mean weight loss rate (unit: %/min), $t_i$, $t_p$, and $t_b$ represent the time corresponding to $T_i$, $T_{max}$, and $T_b$, and $\Delta t_{1/2}$ represents the time interval between half value of $R_p$ (unit: min).

Pyrolysis experiments were performed by the same reactor as torrefaction pretreatment (refer to **Figure 2.1**). The sample was placed in a quartz basket and hung in the heating area of the heater. Then the reactor was controlled to be air-free by 10 min's nitrogen gas purging with a flow rate of 300 mL/min. Afterward, the reactor was heated from room temperature to 600 °C at a heating rate of 20 °C/min and maintained for another 20 min. The volatile product was swept out through a condenser tube filled with ice-cooling water, and the liquid product was finally collected in an Erlenmeyer flask located in an ice-water bath. After the reaction time was completed, the reactor was naturally cooled to room temperature with nitrogen gas purging. The residue was removed, weighed, and stored in a sample bottle. The yield of liquid product (condensable volatile) was obtained by calculating the weight differences of the Erlenmeyer flask and the reactor before and after reaction. The yield of gas product was determined by mass balance. Duplicated experiments were performed to confirm the repeatability validation, and the average results were calculated for analysis.

### 2.2.4 Characterization of oil composition

Gas chromatography-mass spectrometer (GC/MS; Shimadzu QP 2010, Japan) was applied to determine the chemical composition of the oil products. Anhydrous sodium sulfate was added to the liquid product to remove the aqueous fraction prior to oil analysis. Then, the filtered oil product was diluted by dichloromethane at a ratio of 1:20 and further filtered through a 0.22 μm filter film; the obtained oil was injected into GC/MS for analysis. A Shimadzu SH-Rxi-5Sil MS Capacity Column (30 m, 0.25 mm, and 0.25 μm) was selected for chromatographic separation. The initial oven temperature was maintained at 40 °C for 10 min, then it was increased to 260 °C at a heating rate of 5 °C/min and then kept for 6 min. Helium (99.999%) was employed as the carrier gas at a flow rate of 1.0 mL/min, the split ratio was set as 50:1, and the solvent delay was set at 3 min. The chromatographic peaks were identified by referring to the National Institute of Standards and Technology (NIST) spectral library and literature data.

## 2.3 Results and discussion

### 2.3.1 Characterization of RS and TS

#### 2.3.1.1 Ultimate analysis, proximate analysis, and composition analysis

The main characteristics of RS and TS are presented in **Table 2.1**. Ultimate analysis indicates that the carbon content increased with increasing torrefaction temperature, whereas the hydrogen and oxygen contents decreased. As a consequence, the HHV of RS is enhanced after torrefaction, suggesting improved fuel properties. Meanwhile, H/C and O/C molar ratios of RS and TS both decreased as torrefaction intensified, implying that dehydration and deoxygenation reactions dominate the devolatilization of RS during torrefaction, as confirmed by the Van Krevelen diagram in **Figure 2.3**.

**Table 2.1** Ultimate analysis, proximate analysis, and composition of samples.

| | RS | TS200 | TS250 | TS300 |
|---|---|---|---|---|
| ***Ultimate analysis*** (wt. % dry basis) | | | | |
| H | 4.82 | 4.63 | 3.87 | 3.25 |
| C | 34.82 | 37.19 | 41.56 | 41.38 |
| N | 0.83 | 0.94 | 1.18 | 1.23 |
| S | 0.52 | 0.59 | 0.68 | 0.53 |
| O[1] | 39.23 | 34.43 | 21.1 | 15.34 |
| H/C | 1.66 | 1.49 | 1.12 | 0.94 |
| O/C | 0.84 | 0.69 | 0.38 | 0.28 |
| HHV[2] | 13.72 | 14.77 | 16.63 | 16.34 |
| ***Proximate analysis*** (wt. % as received basis) | | | | |
| Ash | 19.78 | 22.22 | 31.61 | 38.27 |
| Moisture | 6.63 | 2.52 | 0.96 | 0.55 |
| Volatile | 71.06 | 67.08 | 50.25 | 35.96 |
| Fixed carbon | 2.53 | 8.18 | 17.18 | 25.22 |
| ***Composition of RS and TS*** (wt. %) | | | | |
| Hemicellulose | 4.67 ± 0.6 | 2.36 ± 1.1 | 0 | 0 |
| Cellulose | 31.36 ± 1.21 | 33.98 ± 0.23 | 11.56 ± 0.44 | 1.98 ± 0.87 |
| Lignin | 33.55 ± 1.32 | 34.54 ± 0.93 | 46.18 ± 0.35 | 58.86 ± 1.83 |

[1] O%=100%-C%-H%-N%-S%-Ash%; [2] higher heating value (MJ/mol).

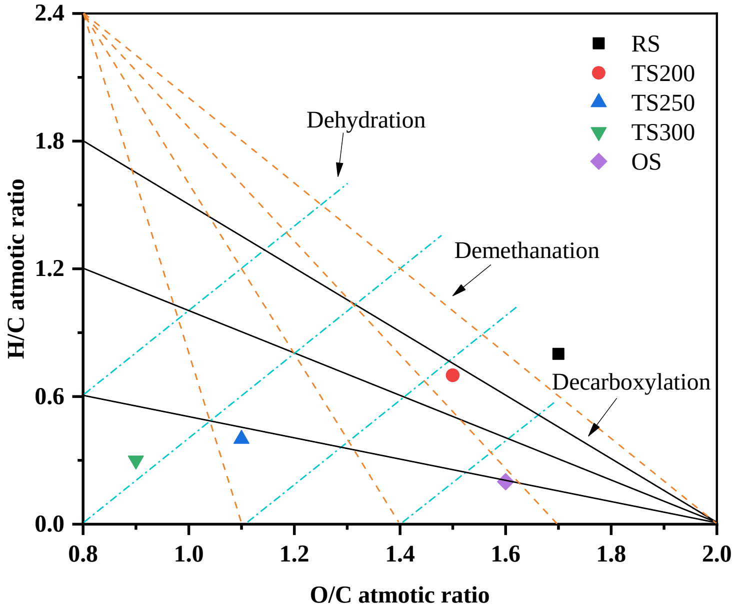

**Figure 2.3** Van Krevelen diagram of RS and TS.

According to proximate analysis, enhanced torrefaction reduced the volatile content of RS from 71.06 to 35.96%, which was attributed to the devolatilization reactions of RS under torrefaction, accompanied by the removal of light organic compounds and gases [2-9]; hence, in contrast, aggravated torrefaction conditions increased the contents of fixed carbon and ash. Lignocellulosic analyses of RS and TS show that severe torrefaction led to higher lignin content at the expense of hemicellulose and cellulose, which is consistent with previous studies [2-5, 2-9]. The lower proportion of hemicellulose and cellulose in TS250 and TS300 was ascribed to their chemical degradation as torrefaction processed. Furthermore, **Table 2.3** shows that torrefaction enhanced the concentration of alkali metals in TS. For example, Potassium (K), the main component of alkali metals, 300 °C torrefaction increased its concentration almost two times higher.

**Table 2.2** Ash composition of samples by XRF analysis.

| ***Main chemical components*** (wt. %) | | | | | | | | |
|---|---|---|---|---|---|---|---|---|
| | $SiO_2$ | $Fe_2O_3$ | $SO_3$ | $Al_2O_3$ | CaO | $K_2O$ | $Na_2O$ | Other |
| RS | 76.65 | 2.54 | 0.44 | 1.71 | 2.14 | 9.63 | 0.57 | 6.32 |
| TS200 | 76.63 | 2.56 | 0.46 | 1.73 | 1.96 | 9.05 | 0.46 | 7.15 |
| TS250 | 77.61 | 2.38 | 0.39 | 1.69 | 2.12 | 8.06 | 0.53 | 7.22 |
| TS300 | 75.71 | 2.37 | 0.45 | 1.75 | 2.03 | 10.82 | 0.48 | 6.39 |

**Table 2.3** Concentration of typical AAEMs in RS and TS by ICP analysis (mg/kg).

| | K | Ca | Mg | Al | Fe |
|---|---|---|---|---|---|
| RS | 13932.53 | 3080.39 | 1173.14 | 888.54 | 1675.92 |
| TS200 | 15503.52 | 3628.48 | 1331.76 | 1134.56 | 1987.63 |
| TS250 | 20950.75 | 3934.16 | 1831.97 | 1196.93 | 2661.11 |
| TS300 | 26960.65 | 4724.64 | 2348.16 | 1670.27 | 3590.37 |

### 2.3.1.2 Microstructure of RS and TS

The FTIR spectra of RS before and after torrefaction are displayed in **Figure 2.4 (a)**. It could be observed that the spectra of RS and TS shared similar trends under different torrefaction temperatures. Several characteristic peaks in area (1) 3030 to 3643 $cm^{-1}$, area (2) 2818 to 3000 $cm^{-1}$, area (3) 1535 to 1780 $cm^{-1}$, area (4) 864 to 1280 $cm^{-1}$, and area (5) 709 to 848 $cm^{-1}$ are detected, attributed to the vibration of -OH stretching, vibration of aliphatic carbon C-H stretching, vibration of aromatic C=O stretching, vibration of aliphatic ether C-O-C and alcohol C-O stretching, and vibration of C-H aromatic out-of-plane deformation, respectively. With increasing torrefaction temperature, the peak intensity of OH functional groups in area (1) became weaker, which confirmed the dehydration of RS during torrefaction. However, the peak intensity of aromatic-based functional groups in area (3) and (5) got enhanced, suggesting the enrichment of lignin. Variation in the deconvoluted peak area of different functional groups agreed well with the characteristics of RS and TS tabulated in **Table 2.1**.

**Figure 2.4 (a)** depicts the FTIR spectra of RS and TS, and **Figure 2.4 (b)** and **(c)** displays TS200’s infrared spectrum as examples for semi-quantitative analysis, where the assignments of the peaks obtained from previous literature are listed in **Table 2.4** [2-16, 2-17].

**Table 2.4** Parameters of fitted peaks from TS200's infrared spectrum.

| Peak | Center ($cm^{-1}$) | Assignment | Area (%) |
|---|---|---|---|
| ***1785-1485 $cm^{-1}$*** | | | |
| 1 | 1513.11 | Stretching vibration of C=C in aromatic rings | 0.1001 |
| 2 | 1550.38 | Stretching vibration of C=C in aromatic rings | 0.1769 |
| 3 | 1591.65 | Stretching vibration of C=C in aromatic rings | 0.2748 |
| 4 | 1639.06 | Stretching vibration of highly conjugated C=O (such as quinones) | 2.3053 |
| 5 | 1720.73 | Stretching vibration of C=O in carboxylic rings | 0.4442 |
| ***3000-2800 $cm^{-1}$*** | | | |
| 6 | 2828.49 | CH symmetric stretching | 0.0234 |
| 7 | 2851.24 | CH2 symmetric stretching in alkanes | 0.0845 |
| 8 | 2877.86 | CH3 symmetric stretching | 0.1967 |
| 9 | 2920.97 | CH2 symmetric stretching in alkanes | 0.4043 |
| 10 | 2966.69 | CH3 symmetric stretching | 0.0394 |

Several structural parameters obtained from curve fitting of FTIR spectra of RS and TS are listed in **Table 2.5** to further evaluate the effect of torrefaction temperature on the evolution of functional groups in RS and TS. The A factor value of RS gradually decreased from 0.21 to 0.12% as the intensity of torrefaction increased, implying that severe torrefaction weakened the hydrocarbon-generating potential of TS, which was attributed to the enhanced devolatilization of RS during torrefaction. The $CH_2/CH_3$ value significantly increased from 0.48 to 2.07% when torrefaction temperature was set at 200 °C, whereas it decreased as temperature further increased. This can be explained as follows: under mild torrefaction, the ring structures of polysaccharides in hemicellulose are opened to generate aliphatic intermediates, and these intermediates will combine with each other to form longer aliphatic chains, therefore behaving in a higher $CH_2/CH_3$ value under 200 °C torrefaction [2-18]. As torrefaction temperature continuously increases, depolymerization and fragmentation of nascent aliphatic chains get exacerbated, such as the degradation of the side chains and chain end scissions, leading to shorter aliphatic chains of molecules, thereby resulting in a lower $CH_2/CH_3$ value [2-19, 2-20]. Furthermore, higher torrefaction temperature promotes the enrichment of lignin and its dealkylation (side chains) assists in increasing the content of aromatic compounds. Consequently, the aromaticity index ($A_{ar}/A_{al}$) of TS got enhanced under severe torrefaction.

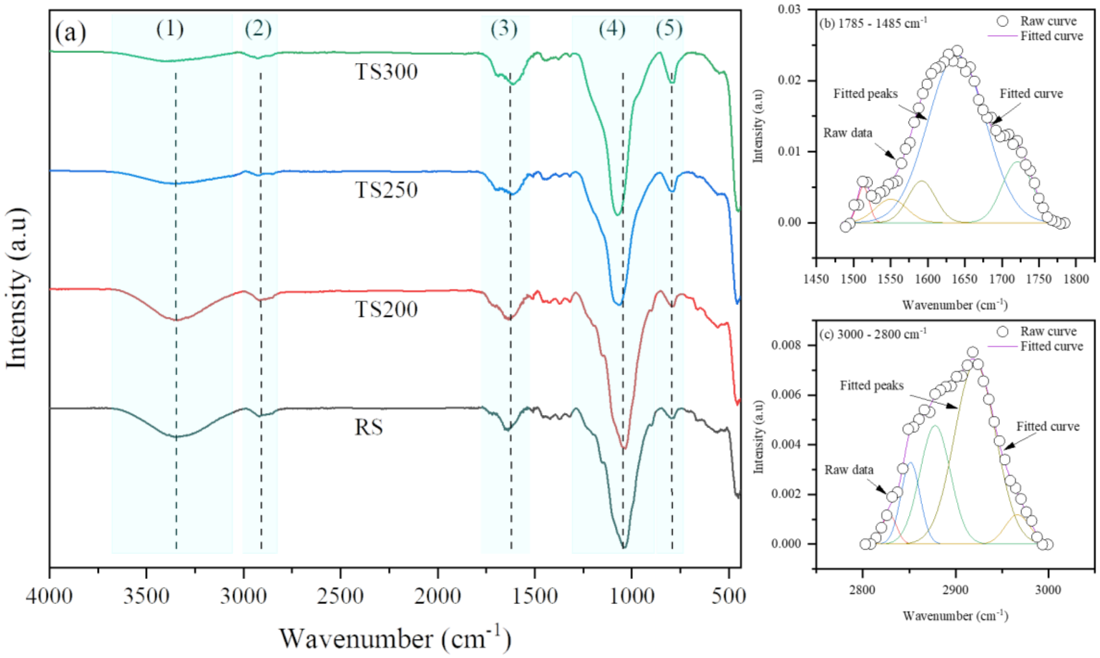

**Figure 2.4** (a) FTIR spectra of RS and TS, (b) curve fitting of TS200 in 1785-1485 cm$^{-1}$, and (c) curve fitting of TS200 in 3000-2800 cm$^{-1}$.

**Table 2.5** FTIR indexes deduced from FTIR spectra of RS and TS (%).

| | RS | TS200 | TS250 | TS300 |
|---|---|---|---|---|
| A factor | 0.21 | 0.20 | 0.13 | 0.12 |
| $CH_2/CH_3$ | 0.48 | 2.07 | 1.75 | 0.83 |
| $A_{ar}/A_{al}$ | 3.83 | 3.68 | 6.27 | 7.27 |

The SEM images are shown in **Figure 2.5** for an in-depth investigation of the surface morphology of RS and TS. The surface of RS is characterized by a flat morphology with relatively smooth epidermis. TS suggests that torrefaction removes or facilitates the removal of the epidermis, resulting in a rough and fluffy structure. However, the inner skeletal morphology is not considerably altered, even under severe torrefaction (300 °C). The SEM results demonstrate that the surface microstructure of RS/TS is associated with the devolatilization intensity during torrefaction.

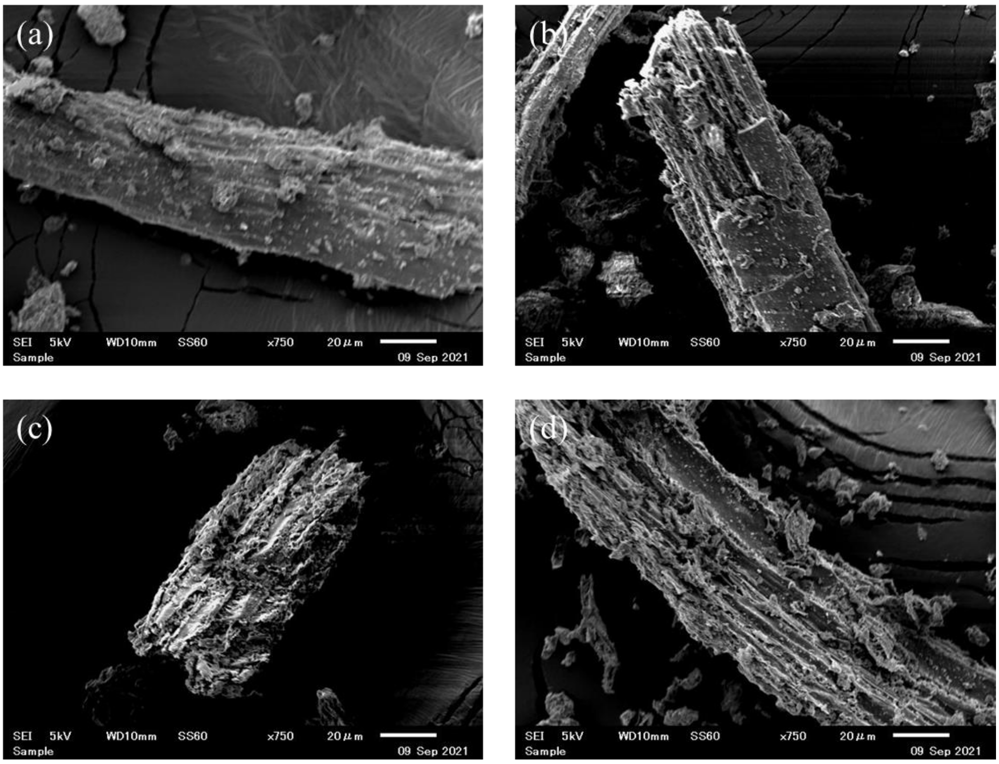

**Figure 2.5** SEM images of samples: (a) RS, (b) TS200, (c) TS250, and (d) TS300.

### 2.3.1.3 Crystallinity of RS and TS

**Figure 2.6** illustrates the XRD patterns of RS and TS, and their calculated Crystallinity Index (CrI) is also listed. As torrefaction temperature increased, the peak intensity at $2\theta = 22°$ gradually decreased; simultaneously, several sharp peaks occurred at $2\theta$ = 24°, 28°, 41°, and 51° on XRD patterns, representing the appearance of potassium chloride, which is in accord with the increasing concentration of potassium in TS obtained under severe torrefaction. It was reported that the variation of CrI value was predominantly determined by the competitive decomposition of crystalline cellulose and amorphous cellulose in biomass [2-12]. As a result, the initial rise of CrI value at a torrefaction temperature of 200 °C could be due to the recrystallization of amorphous cellulose before being decomposed under intensified torrefaction. Then, when the torrefaction temperature was set higher than 200 °C, the CrI value of TS decreased from 30.03 to 7.41%, implying the constant loss of crystalline components, especially crystalline cellulose, in TS. Similar results were well documented in previous literature [2-21].

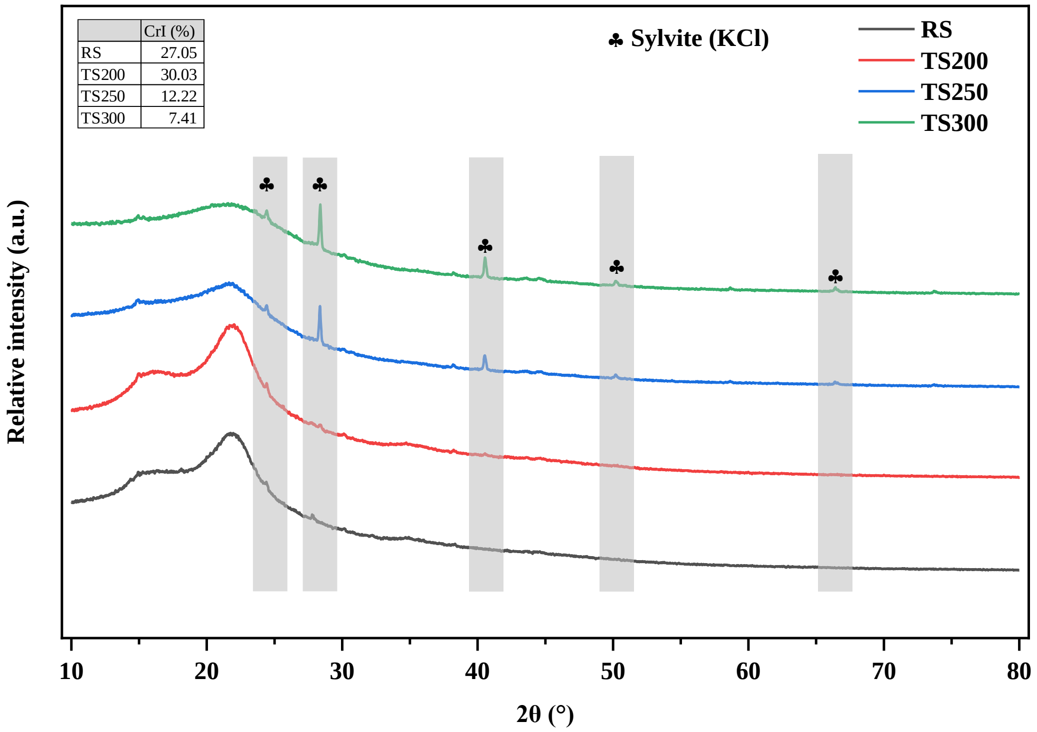

**Figure 2.6** XRD patterns of RS and TS.

### 2.3.2 Thermal decomposition characteristics of RS and TS

The thermal decomposition curves of RS and TS are depicted in **Figure 2.7** and the corresponding pyrolysis characteristics are summarized in **Table 2.6**. TG profiles represent the weight loss of samples, and DTG profiles reflect its corresponding weight loss rate. As shown in **Figure 2.7 (b)**, the entire thermal decomposition process of RS and TS mainly exhibited one weight loss peak, representing the overlapped decomposition of hemicellulose, cellulose, and lignin. Generally, there should be a shoulder peak occurring at 200 °C before the predominant weight loss peak of biomass, representing the decomposition of hemicellulose which has low thermal stability [2-20]. In current work, this shoulder peak was difficult to distinguish, probably due to the relatively low hemicellulose content in RS (refer to **Table 2.1**) and a relatively high heating rate. Intensified torrefaction led to the degradation of components with low thermal stability, in the sequence of hemicellulose, cellulose, and lignin, leaving enrichment of recalcitrant portion in TS and hence enhancing its thermal resistance [2-2]. As a result of this, the pyrolysis properties of TS deteriorated according to the pyrolysis performance indexes listed in **Table 2.6**. Meanwhile, the main weight loss region of TS was moved to higher temperature ranges as torrefaction intensified, as shown in **Figure 2.7 (b)**. It is worth noting that the maximum weight loss rate of TS200 (-11.73 %/min) was slightly higher than that of RS (-11.24 %/min), which might be due to the following two reasons. Firstly, the maximum decomposition rate of biomass between 300 and 390 ° C is attributed to the depolymerization of crystalline components in biomass [2-22]; Secondly, hemicellulose decomposes earlier than cellulose owing to its lower thermal stability, furnished with a liquid film covering the surface of residues, hindering the subsequent decomposition of cellulose [2-23]. Therefore, the higher crystallinity degree and the weaker inhibition from hemicellulose in TS200 promoted the maximum decomposition rate.

**Table 2.6** Pyrolysis characteristics of RS and TS.

| Sample | $T_i$ | $T_b$ | $T_p$ | $R_p$ | $R_{mean}$ | $D_i$ | $D_b$ | CPI |
|---|---|---|---|---|---|---|---|---|
| RS | 269.13 | 850.25 | 324.56 | 11.24 | 1.65 | 58.38 | 45.54 | 30.11 |
| TS200 | 283.02 | 853.17 | 329.98 | 11.73 | 1.57 | 59.46 | 55.78 | 26.95 |
| TS250 | 294.52 | 872.93 | 336.08 | 4.93 | 1.17 | 23.44 | 17.98 | 7.62 |
| TS300 | 342.43 | 881.58 | 463.20 | 1.72 | 0.85 | 4.92 | 1.23 | 1.48 |

$T_i$: ignition temperature (°C); $T_b$: burnout temperature (°C); $T_P$: peak temperature corresponding to maximum weight loss rate (°C); $R_p$: maximum weight loss rate; $R_{mean}$: mean weight loss rate; $D_i$: ignition index ($10^{-3}$%/min$^{-3}$); $D_b$: burnout index ($10^{-4}$%/min$^{-4}$); CPI: comprehensive pyrolysis index ($10^{\wedge-8}$min$^{-2}$°C$^{-3}$)

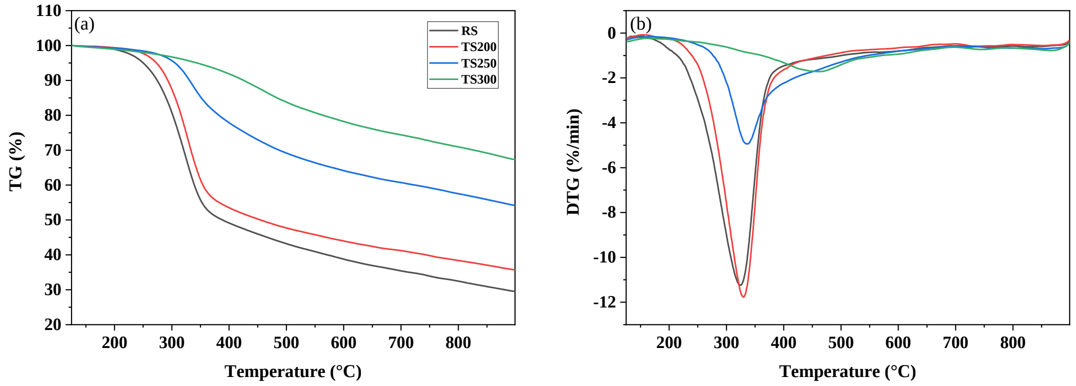

**Figure 2.7** (a) TG and (b) DTG curves of RS and TS.

## 2.3.3 Effect of torrefaction on pyrolysis of RS

### 2.3.3.1 Product yields distribution

**Figure 2.8** shows the product yield distribution of individual pyrolysis. As torrefaction temperature increased from 0 to 300 °C, the char yield increased from 37.42 to 73.83%, whereas the oil and gas yield decreased from 27.45 to 6.54% and 35.13 to 19.63 %, respectively. The pyrolysis product yields of RS and TS align with their proximate analysis results, as listed in **Table 2.1**. During torrefaction, RS underwent devolatilization, cross-linking, and carbonization, leaving TS with accumulated alkali metals and enhanced surface aromaticity, which altered TS's decomposition pathways to promote char formation and reduce volatilization. On one hand, enriched alkali metals in TS catalyzed the pyrolysis reactions, resulting in an increase in char and gas yields at the expense of oil compared to RS. On the other hand, severe torrefaction led to TS being covered by thermal stable aromatic structures, impeding the diffusion of volatiles [2-24]. Similar results on biomass torrefaction are reported elsewhere [2-23, 2-25]. Interestingly, the gas yield of TS200 (36.85%) was higher than that of RS (35.13%) though an insignificant difference was observed, which is consistent with the relatively higher maximum decomposition rate of TS200 compared to RS. Firstly, slight torrefaction partially removed hemicellulose and marginally altered the composition of RS (refer to **Table 2.1**), thus the hindering effect of hemicellulose decomposition on gas release was undermined [2-23, 2-25, 2-26]. Secondly, TS200 contained more alkali metals, especially K, posing a more substantial catalytic effect for opening glycosidic rings to produce light compounds and gases [2-27]. Previous studies also found that slight torrefaction might increase the pyrolysis gas yield to some extent [2-24].

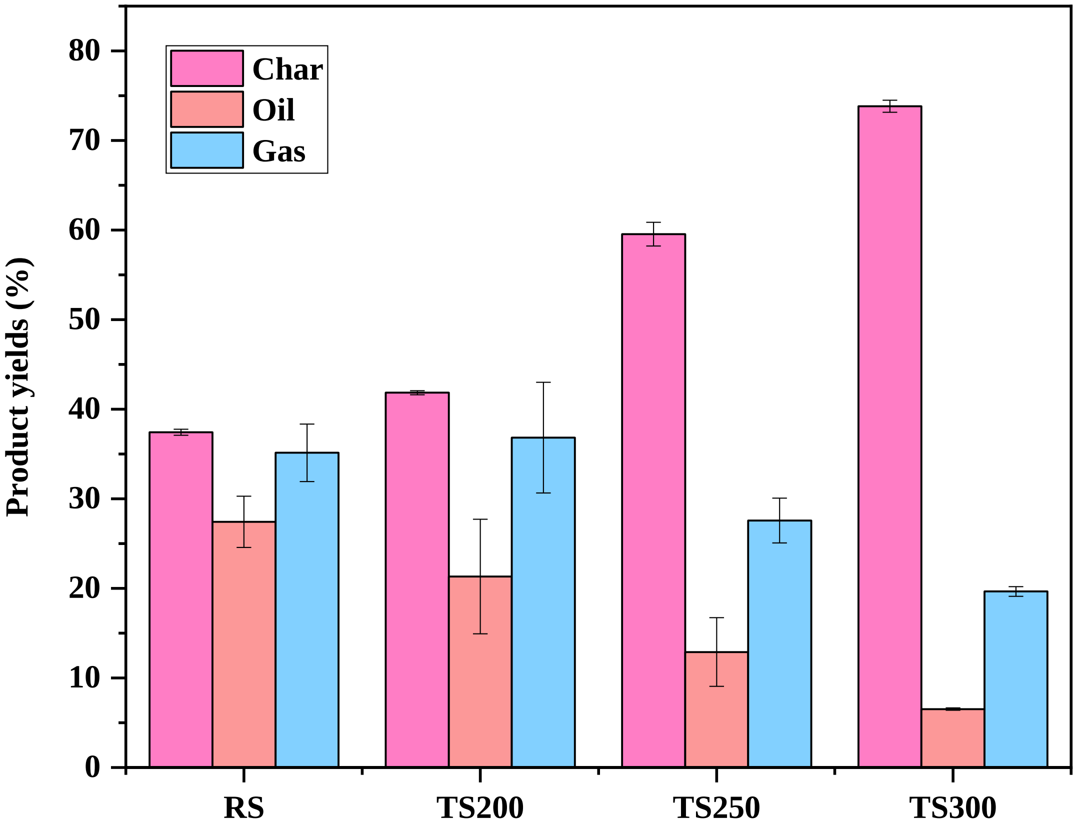

**Figure 2.8** Product yields from individual pyrolysis of RS and TS.

### 2.3.3.2 Oil composition

The chemical composition of oil derived from pyrolysis of RS and TS is displayed in **Figure 2.9**. Detected chemical compounds are mainly divided into two categories: hydrocarbons and oxygenates. It should be noted that neither hydrocarbons nor oxygenates in this study contain hetero elements other than C, H, and O. Oil generated from RS pyrolysis was of poor quality as it was dominated by oxygenates, accounting for 77.79%. The high concentration of oxygenates was resulted from the high oxygen content and low carbon content in RS. After torrefaction, the property of oil was significantly improved with a decreasing concentration of oxygenates (from 77.79 to 24.06%). **Table 2.7** summarizes the concentrations of typical groups of oxygenated compounds. As indicated, torrefaction pronouncedly reduced the concentrations of acid, alcohol, aldehyde, anhydrosugar, ester, furan, and ketone in oil products. These oxygenated compounds mainly evolved from the dehydration, depolymerization, and rearrangement during pyrolysis of holocellulose (hemicellulose and cellulose) [2-2, 2-

19], which concentration therefore extremely decreased as torrefaction consumed the holocellulose content in TS. Besides, accumulated alkali metals in TS were prone to promote carbonization reactions and formation of the lignin-derived char during TS pyrolysis, suppressing the conversion of levoglucosan into light oxygenates [2-17, 2-23]. In contrast, the production of phenol was promoted with increasing torrefaction temperature. This is associated with the increase in relative content of lignin, precursor of phenols, in TS.

**Table 2.7** Relative concentrations of oxygenates in oil from individual pyrolysis of RS and TS.

| | RS | TS200 | TS250 | TS300 |
|---|---|---|---|---|
| acid | 14.72 | 13.39 | 7.83 | 0.78 |
| alcohol | 4.8 | 4.42 | 3.65 | 1.65 |
| aldehyde | 12.99 | 10.34 | 3.52 | 0 |
| anhydrosugars | 2.02 | 1.8 | 1.27 | 0 |
| ester | 5.52 | 4.22 | 0 | 0.57 |
| furan | 11.99 | 10.88 | 4.77 | 0 |
| ketone | 15.35 | 14.25 | 10.05 | 0.61 |
| phenol | 10.2 | 14.75 | 18.2 | 20.45 |
| ***Sum*** | 77.59 | 74.05 | 49.29 | 24.06 |

Contrary to the reduction of oxygenates, torrefaction enhanced the production of hydrocarbons from 17.08 to 65.81%. As displayed in **Figure 2.9 (a-1)**, **(a-2)**, and **(a-3)**, the concentrations of alkane, aromatic, and olefin hydrocarbons all gradually increased as torrefaction intensified, and the former two contributed to the main increase of total hydrocarbons. Alkane and olefin hydrocarbons are principally generated from the rearrangement of hydrocarbon radicals produced from ring-opening and deoxygenation of holocellulose, and the cleavage of alkyl side chains of lignin [2-19, 2-28]. Aromatic hydrocarbons are mainly produced through depolymerization, oligomerization, and demethylation from the aromatic structure of lignin. Therefore, enriched lignin content in TS promoted the formation of hydrocarbons.

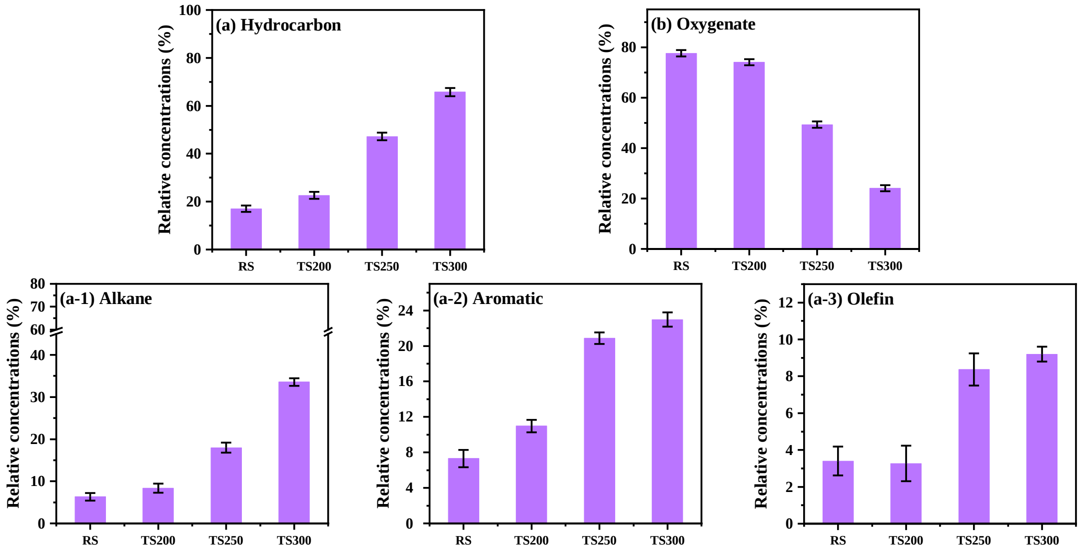

**Figure 2.9** Relative concentration of (a) hydrocarbon, (b) oxygenate, (a-1) alkane, (a-2) aromatic, and (a-3) olefin in oil products from pyrolysis of RS and TS.

## 2.4 Conclusions

The effect of torrefaction on morphological structure evolution and pyrolysis properties of rice straw are comprehensively investigated in this chapter.

(1) Intensified torrefaction led to enhanced surface aromaticity, rougher surface structure, and decreased crystallinity of RS.

(2) The pyrolysis reactivity of RS was weakened after torrefaction, and the decomposition temperature ranges of TS were shifted to higher temperatures with increasing torrefaction temperature.

(3) Torrefaction altered the pyrolysis pathway of TS to enhance char production at the expense of oil and gas.

(4) Torrefaction pretreatment enhanced hydrocarbon production, especially alkanes and aromatics.

## References

[2-1] Kan, T., Strezov, V., & Evans, T. J. (2016). Lignocellulosic biomass pyrolysis: A review of product properties and effects of pyrolysis parameters. Renewable and

sustainable energy reviews, 57, 1126-1140.

[2-2] Dai, L., Wang, Y., Liu, Y., Ruan, R., He, C., Yu, Z., ... & Tian, X. (2019). Integrated process of lignocellulosic biomass torrefaction and pyrolysis for upgrading bio-oil production: A state-of-the-art review. Renewable and Sustainable Energy Reviews, 107, 20-36.

[2-3] Saraeian, A., Nolte, M. W., & Shanks, B. H. (2019). Deoxygenation of biomass pyrolysis vapors: Improving clarity on the fate of carbon. Renewable and Sustainable Energy Reviews, 104, 262-280.

[2-4] Chen, W. H., Peng, J., & Bi, X. T. (2015). A state-of-the-art review of biomass torrefaction, densification and applications. Renewable and Sustainable Energy Reviews, 44, 847-866.

[2-5] Chen, D., Li, Y., Deng, M., Wang, J., Chen, M., Yan, B., & Yuan, Q. (2016). Effect of torrefaction pretreatment and catalytic pyrolysis on the pyrolysis poly-generation of pine wood. Bioresource technology, 214, 615-622.

[2-6] Chen, W. H., Lin, B. J., Lin, Y. Y., Chu, Y. S., Ubando, A. T., Show, P. L., ... & Pétrissans, M. (2021). Progress in biomass torrefaction: Principles, applications and challenges. Progress in Energy and Combustion Science, 82, 100887.

[2-7] Van der Stelt, M. J. C., Gerhauser, H., Kiel, J. H. A., & Ptasinski, K. J. (2011). Biomass upgrading by torrefaction for the production of biofuels: A review. Biomass and bioenergy, 35(9), 3748-3762.

[2-8] Sabil, K. M., Aziz, M. A., Lal, B., & Uemura, Y. (2013). Effects of torrefaction on the physiochemical properties of oil palm empty fruit bunches, mesocarp fiber and kernel shell. Biomass and Bioenergy, 56, 351-360.

[2-9] Zheng, A., Zhao, Z., Chang, S., Huang, Z., He, F., & Li, H. (2012). Effect of torrefaction temperature on product distribution from two-staged pyrolysis of biomass. Energy & Fuels, 26(5), 2968-2974.

[2-10] Cordero, T., Marquez, F., Rodriguez-Mirasol, J., & Rodriguez, J. J. (2001). Predicting heating values of lignocellulosics and carbonaceous materials from proximate analysis. Fuel, 80(11), 1567-1571.

[2-11] Van Soest, P. V., Robertson, J. B., & Lewis, B. A. (1991). Methods for dietary fiber, neutral detergent fiber, and nonstarch polysaccharides in relation to animal nutrition. Journal of dairy science, 74(10), 3583-3597.

[2-12] Zhang, C., Yang, W., Chen, W. H., Ho, S. H., Pétrissans, A., & Pétrissans, M. (2022). Effect of torrefaction on the structure and reactivity of rice straw as well as life cycle assessment of torrefaction process. Energy, 240, 122470.

[2-13] Li, X. G., Ma, B. G., Xu, L., Hu, Z. W., & Wang, X. G. (2006). Thermogravimetric analysis of the co-combustion of the blends with high ash coal and waste tyres. Thermochimica Acta, 441(1), 79-83.

[2-14] Seggiani, M., Vitolo, S., Pastorelli, M., & Ghetti, P. (2007). Combustion reactivity of different oil-fired fly ashes as received and leached. Fuel, 86(12-13), 1885-1891.

[2-15] Wang, C. A., Zhang, X., Liu, Y., & Che, D. (2012). Pyrolysis and combustion characteristics of coals in oxyfuel combustion. Applied Energy, 97, 264-273.

[2-16] Qiu, S., Zhang, S., Zhou, X., Zhang, Q., Qiu, G., Hu, M., ... & Bai, C. (2019). Thermal behavior and organic functional structure of poplar-fat coal blends during co-pyrolysis. Renewable Energy, 136, 308-316.

[2-17] Zhao, Y., Liu, L., Qiu, P. H., Xie, X., Chen, X. Y., Lin, D., & Sun, S. Z. (2017). Impacts of chemical fractionation on Zhundong coal's chemical structure and pyrolysis reactivity. Fuel Processing Technology, 155, 144-152.

[2-18] Shen, D. K., Gu, S., & Bridgwater, A. V. (2010). Study on the pyrolytic behaviour of xylan-based hemicellulose using TG–FTIR and Py–GC–FTIR. Journal of analytical and applied pyrolysis, 87(2), 199-206.

[2-19] Chen, D., Gao, A., Cen, K., Zhang, J., Cao, X., & Ma, Z. (2018). Investigation of biomass torrefaction based on three major components: Hemicellulose, cellulose, and lignin. Energy conversion and management, 169, 228-237.

[2-20] Collard, F. X., & Blin, J. (2014). A review on pyrolysis of biomass constituents: Mechanisms and composition of the products obtained from the conversion of cellulose, hemicelluloses and lignin. Renewable and Sustainable Energy Reviews, 38, 594-608.

[2-21] Neupane, S., Adhikari, S., Wang, Z., Ragauskas, A. J., & Pu, Y. (2015). Effect of torrefaction on biomass structure and hydrocarbon production from fast pyrolysis. Green Chemistry, 17(4), 2406-2417.

[2-22] Leng, E., Zhang, Y., Peng, Y., Gong, X., Mao, M., Li, X., & Yu, Y. (2018). In situ structural changes of crystalline and amorphous cellulose during slow pyrolysis at low temperatures. Fuel, 216, 313-321.

[2-23] Khan, S. R., Zeeshan, M., & Masood, A. (2020). Enhancement of hydrocarbons production through co-pyrolysis of acid-treated biomass and waste tire in a fixed bed reactor. Waste Management, 106, 21-31.

[2-24] Zheng, A., Zhao, Z., Chang, S., Huang, Z., Wang, X., He, F., & Li, H. (2013). Effect of torrefaction on structure and fast pyrolysis behavior of corncobs. Bioresource technology, 128, 370-377.

[2-25] Khan, S. R., & Zeeshan, M. (2022). Catalytic potential of low-cost natural zeolite and influence of various pretreatments of biomass on pyro-oil up-gradation during co-pyrolysis with scrap rubber tires. Energy, 238, 121820.

[2-26] Xue, Y., & Bai, X. (2018). Synergistic enhancement of product quality through fast co-pyrolysis of acid pretreated biomass and waste plastic. Energy Conversion and Management, 164, 629-638.

[2-27] Dong, C. Q., Zhang, Z. F., Lu, Q., & Yang, Y. P. (2012). Characteristics and mechanism study of analytical fast pyrolysis of poplar wood. Energy conversion and

Management, 57, 49-59.

[2-28] Tang, C. Y., & Zhang, D. X. (2016). Mechanisms of aliphatic hydrocarbon formation during co-pyrolysis of coal and cotton stalk. Chinese Chemical Letters, 27(10), 1607-1611.

# Chapter 3 Effect of torrefaction on synergistic behavior during co-pyrolysis of oil sludge with rice straw to enhance hydrocarbon production

## 3.1 Introduction

Co-pyrolysis is regarded as a simple and effective method to improve the quantity and quality of pyrolysis oil, which has attracted increasing attention [3-1]. Biomass is frequently selected by researchers for co-pyrolysis with organic wastes due to its abundant, renewable, and carbon neutral characteristics [3-2]. Wang et al. [3-3] found the interactions between sewage sludge and rice straw converted char products into pyrolysis gas and oil, and a 60% blending ratio of rice straw yielded the strongest interaction. Zhang et al. [3-4] noticed the addition of rice husk into co-pyrolysis with sewage sludge enhanced gas production, and the calorific value of gas products was significantly increased. Martinez et al. [3-5] obtained a more stable oil product with lower oxygen content and higher calorific value through co-pyrolysis of wood chips and waste tires.

The results in **Chapter 2** indicated that torrefaction pretreatment altered the physicochemical properties of rice straw, especially increasing the concentration of hydrocarbons in pyrolysis oil. Recently, combining torrefaction and co-feeding with petroleum-based feedstock to improve the quality of pyrolysis oil from biomass has attracted researchers' attention [3-6]. For example, Bu et al. [3-7] fed low-density polyethylene (LDPE) as a hydrogen source into microwave pyrolysis of microwave torrefied lignin (MTL). Their results demonstrated that the hydrocarbon concentration in the oil obtained from co-pyrolysis increased to around 80%, especially the aromatic hydrocarbons rose from 1.9% to 22.8%. Huang et al. [3-8] conducted co-pyrolysis of Chinese herb residues (CHR) and low-density polyethylene (LDPE), and the results indicated that torrefaction of CHR stimulated synergism between reactants, simultaneously increased aliphatic hydrocarbons in the oil products. Lee et al. [3-9]

also observed that torrefaction of cork oak enhanced the synergistic formation of mono aromatic hydrocarbons in the catalytic co-pyrolysis of Oak and HDPE over HY zeolites.

Nevertheless, to the best of the author’s knowledge, research on co-pyrolysis of torrefied biomass with oil sludge (OS) is yet to be studied, although sole pyrolysis of torrefied biomass or co-pyrolysis of biomass and OS are discussed extensively. Therefore, combining torrefaction of biomass and co-pyrolysis with OS to enhance hydrocarbon production in oil deserves in-depth investigation. On one hand, the alkali metals in biomass and the ash in OS pose catalytic reactivities, synergistically promoting pyrolysis behavior and improving the oil quality. On the other hand, torrefaction increased the content of lignin in biomass at the expense of holocellulose (hemicellulose and cellulose); for example, 300 °C torrefied rice straw (refer to **Chapter 2**) was mainly consisted of lignin. As a result, co-pyrolysis of OS and rice straw/torrefied rice straw can represent the co-pyrolysis of oil sludge and model biomass compounds, such as oil sludge and holocellulose, oil sludge and lignin. Selecting rice straw in this study for co-treatment with oil sludge is because agricultural waste is generated closer to where oil sludge is generated. Their co-processing is rational and economical, saving transportation costs. In this chapter, the fundamental characteristics of RS and TS in **Chapter 2** are included for comparative analysis, and the structure of **Chapter 3** is shown in **Figure 3.1**.

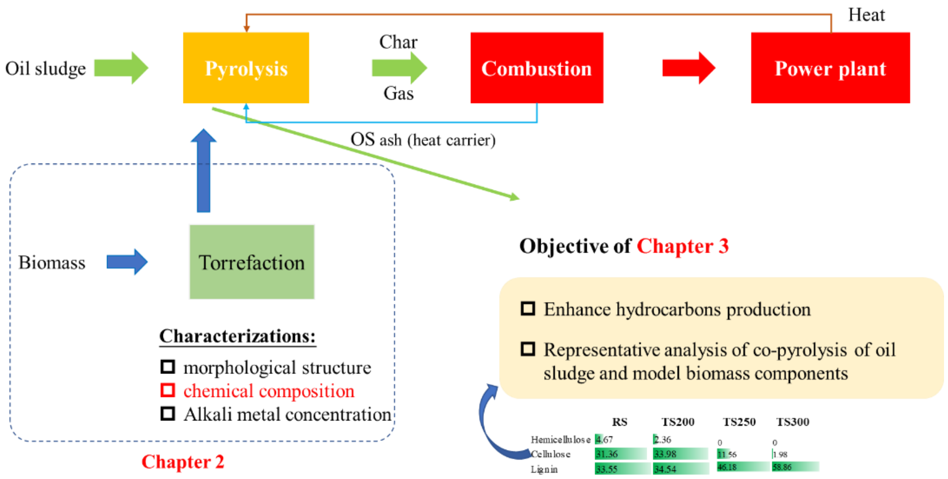

**Figure 3.1** Structure of Chapter 3.

## 3.2 Materials and methods

### 3.2.1 Materials and torrefaction pretreatment

The oil sludge (OS) sample was supplied by Zhejiang Eco-Environmental Technology Co., Ltd, China. The rice straw (RS) sample was purchased from a gardening market in Japan. Details of sample pretreatment and torrefaction experiments are listed in **Chapter 2**. It should be noted that the oil sludge sample used in this study is oilfield sludge, generated during oilfield exploitation, drilling, and other operations, including oil-contaminated soil at oil wells (falling sludge), sediments from the separation system of union stations, and drilling mud. The optimal way to deal with oilfield sludge is on-site disposal. Rice is mainly grown in the suburbs, near oil fields or oil sludge disposal sites, thus rice straw can be easily transported to the processing site, saving transportation costs. As a large rice-growing country, the annual production of rice straw is huge in China. Therefore, co-pyrolysis of oilfield sludge and rice straw can improve the pyrolysis efficiency of oilfield sludge and relieve the pressure resulted from the urgent need for treatment of rice straw.

### 3.2.2 Characterization of samples

The proximate analysis and ultimate analysis of OS were characterized by the same method as RS and TS (refer to **Section 2.2.2**), and the results are listed in **Table 3.1**. The ash composition of OS was measured by an XRF (XRF; S2 Ranger Bruker, Japan) analyzer, and the result is displayed in **Table 3.2**. It should be noted that **Table 3.1** and **Table 3.2** were modified based on **Table 2.1** and **Table 2.2**. XRD (XRD; Bruker D8, Japan) analysis was performed to identify the crystalline status of OS and char samples with Cu Kα radiation in the scanning range of 2θ = 10 - 80°.

### 3.2.3 Experimental apparatus and method

Thermogravimetric analysis was performed on a thermogravimetric analyzer (TG-DTA; TA-60WS, Shimadzu, Japan). For each run, around 10 mg sample of OS and its mixtures with RS or TS under 1:1 ratio was heated from 30 to 900 °C under a nitrogen gas flow rate of 100 ml/min. The heating rate was controlled at 20 °C/min.

The method for evaluating the pyrolysis characteristics of OS and the mixtures were the same as **Chapter 2** in **section 2.2.3**. Pyrolysis and co-pyrolysis experiments were conducted in a fixed bed reactor, as shown in **Figure 2.2**. The experimental procedure for (co) pyrolysis was the same as that in **section 2.2.3**.

For co-pyrolysis experiments, OS and RS/TS were mixed with blending ratios of 3:1, 1:1, and 1:3, respectively. For example, OS:RS = 3:1 denotes the blending ratio of OS and RS is 3:1, and OS:TS = 3:1 denotes the blending ratio of OS and TS is 3:1. Before adding RS/TS into OS, OS was put in an oven at 50 °C for 1h at first to reduce its viscosity, and finally, a uniform mixture was obtained.

### 3.2.4 Characterization of oil composition

Gas chromatography-mass spectrometer (GC/MS; Shimadzu QP 2010, Japan) was applied to determine the chemical composition of the oil products. The characterization method was the same as that in **section 2.2.4**.

## 3.3 Results and discussion

### 3.3.1 Characterization of samples

The main characteristics of OS, RS and TS, and are presented in **Table 3.1**. Compared to RS and TS, the carbon, hydrogen, oxygen, and volatile in OS are much less, whereas OS contains higher ash particles. As seen in **Table 3.2**, the ash particles in OS contain more than 30% metal oxides and approximately 12.97% $SO_3$, which has been reported to act as catalysts during pyrolysis of OS [3-10, 3-11].

**Table 3.1** Ultimate analysis, proximate analysis, and composition of samples.

| | RS | TS200 | TS250 | TS300 | OS |
|---|---|---|---|---|---|
| ***Ultimate analysis*** (wt. % dry basis) | | | | | |
| H | 4.82 | 4.63 | 3.87 | 3.25 | 2.76 |
| C | 34.82 | 37.19 | 41.56 | 41.38 | 19.73 |
| N | 0.83 | 0.94 | 1.18 | 1.23 | 0.38 |
| S | 0.52 | 0.59 | 0.68 | 0.53 | 0.96 |
| O[1] | 39.23 | 34.43 | 21.1 | 15.34 | 3.67 |
| H/C | 1.66 | 1.49 | 1.12 | 0.94 | 1.68 |
| O/C | 0.84 | 0.69 | 0.38 | 0.28 | 0.14 |
| HHV[2] | 13.72 | 14.77 | 16.63 | 16.34 | 8.86 |
| ***Proximate analysis*** (wt. % as received basis) | | | | | |
| Ash | 19.78 | 22.22 | 31.61 | 38.27 | 72.50 |
| Moisture | 6.63 | 2.52 | 0.96 | 0.55 | 1.55 |
| Volatile | 71.06 | 67.08 | 50.25 | 35.96 | 21.74 |
| Fixed carbon | 2.53 | 8.18 | 17.18 | 25.22 | 4.21 |
| ***Composition of RS and TS*** (wt. %) | | | | | |
| Hemicellulose | 4.67 ± 0.6 | 2.36 ± 1.1 | 0 | 0 | |
| Cellulose | 31.36 ± 1.21 | 33.98 ± 0.23 | 11.56 ± 0.44 | 1.98 ± 0.87 | |
| Lignin | 33.55 ± 1.32 | 34.54 ± 0.93 | 46.18 ± 0.35 | 58.86 ± 1.83 | |

[1] O%=100%-C%-H%-N%-S%-Ash%; [2] higher heating value (MJ/mol).

**Table 3.2** Ash composition of samples by XRF analysis.

| | | | | | | | | |
|---|---|---|---|---|---|---|---|---|
| ***Main chemical components*** (wt. %) | | | | | | | | |
| | $SiO_2$ | $Fe_2O_3$ | $SO_3$ | $Al_2O_3$ | CaO | $K_2O$ | $Na_2O$ | Other |
| RS | 76.65 | 2.54 | 0.44 | 1.71 | 2.14 | 9.63 | 0.57 | 6.32 |
| TS200 | 76.63 | 2.56 | 0.46 | 1.73 | 1.96 | 9.05 | 0.46 | 7.15 |
| TS250 | 77.61 | 2.38 | 0.39 | 1.69 | 2.12 | 8.06 | 0.53 | 7.22 |
| TS300 | 75.71 | 2.37 | 0.45 | 1.75 | 2.03 | 10.82 | 0.48 | 6.39 |
| OS | 49.42 | 13.55 | 12.97 | 8.86 | 7.68 | 3.58 | 1.47 | 2.47 |
| ***Metal element analysis*** (wt. %) | | | | | | | | |
| **Continue of Table 3.2** | | | | | | | | |
| | Fe | Al | Ca | Ni | V | | | |
| OS | 2.56 | 4.28 | 0.69 | 0.0056 | 0.0067 | | | |

## 3.3.2 Thermal decomposition characteristics of RS, TS, OS, and blends

The thermal decomposition curves of OS, RS, TS, and blends are depicted in **Figure 3.2** and the corresponding pyrolysis characteristics are summarized in **Table 3.3** (modified by **Table 2.6**).

The pyrolysis process of OS could be divided into three stages based on weight loss peaks, as indicated in **Figure 3.2 (c)**. The weight loss rates of two valleys (404.91 and 524.12 °C) among three peaks did not drop to zero, suggesting competitive reactions among these three stages. The first stage (151.54-404.95 °C) was attributed to the evaporation of remaining moisture and the degradation of light fractions. Then, the middle and heavy fractions were thermally decomposed into low-molecular-weight substances, as displayed in stage 2 (404.95-524.24 °C) and stage 3 (524.24-854.58 °C). In addition, stage 3 was also associated with the decomposition of inorganic matters such as carbonate and sulfur minerals (e.g., $CaCO_3 \rightarrow CaO + CO_2$ and $K_2SO_4 \rightarrow K_2O + CO_2 + 1/2O_2$). The thermal decomposition characteristic of OS in this work is in good agreement with previous literature [3-12, 3-13]. **Table 3.3** indicates the pyrolysis property of OS was extremely poor compared to RS, while torrefaction narrowed the gap between TS and OS.

The decomposition characteristics of RS and TS are also shown in **Figure 3.2**, which were already discussed in **section 2.3.2**.

**Figure 3.2 (b)** and **(d)** display the decomposition curves of blends. As observed, the TG profiles and DTG profiles (especially 170 – 400 °C) of blends shared similar trends with those of RS and TS, implying that the primary decomposition characteristics were dominated by RS and TS because of their relatively higher volatile content. However, OS blending introduced inert ash, which hindered the transfer of external energy and the release of volatiles, thus leading to poor pyrolysis performance compared to RS/TS alone, as shown in **Table 3.3**. When the temperature was higher than 400 °C, multiple overlapping peaks occurred on the DTG profiles of blends, especially during co-pyrolysis of OS/TS250 and OS/TS300. For example, a peak could be observed between 400 and 520 °C during co-pyrolysis of OS and TS250, which might come from the competitive reactions by OS, as the main decomposition region of OS located in this temperature range. Furthermore, the decomposition characteristic of OS was more pronounced when it is blended into TS300, behaving as the interaction interval moved to a lower temperature range: a weight loss peak between 170 and 360 °C appeared during co-pyrolysis of OS and TS300. This can be explained by the fact that they have similar volatile contents and weight loss temperature ranges. Therefore, it can be speculated that during co-pyrolysis of OS/TS250 and OS/TS300, the contribution of OS to the interactions gradually increased.

Overall, based on the information obtained from current thermogravimetric analysis, the interactions during co-pyrolysis of OS and RS/TS can be summarized as: In the first interval (170 - 400 °C), RS/TS decomposed at first and dominated the reactions; then as temperature increases to the second interval (> 400 °C), the degradation of OS became pronounced and conversely affected the co-pyrolysis process. The result in this work about co-pyrolysis of OS and RS is consistent with relevant literature for co-pyrolysis of RS and other types of petroleum-derived materials [3-14, 3-15], and it further illustrates that the interactions between OS and TS might be altered due to the increasingly severe competitive reactions.

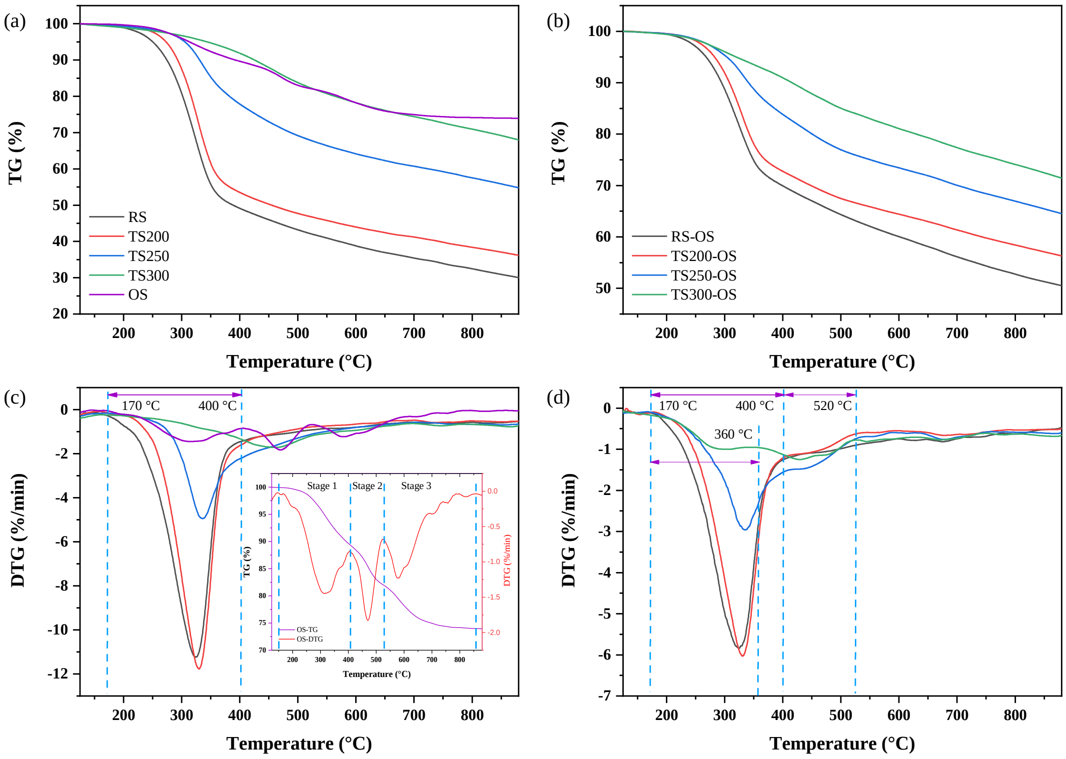

**Figure 3.2** (a) TG and (c) DTG curves individual samples; (b) TG and (d) DTG curves of mixtures.

**Table 3.3** Pyrolysis characteristics of OS, RS, TS, and the blends.

| Sample | $T_i$ | $T_b$ | $T_p$ | $R_p$ | $R_{mean}$ | $D_i$ | $D_b$ | CPI |
|---|---|---|---|---|---|---|---|---|
| RS | 269.13 | 850.25 | 324.56 | 11.24 | 1.65 | 58.38 | 45.54 | 30.11 |
| TS200 | 283.02 | 853.17 | 329.98 | 11.73 | 1.57 | 59.46 | 55.78 | 26.95 |
| TS250 | 294.52 | 872.93 | 336.08 | 4.93 | 1.17 | 23.44 | 17.98 | 7.62 |
| TS300 | 342.43 | 881.58 | 463.20 | 1.72 | 0.85 | 4.92 | 1.23 | 1.48 |
| OS | 330.85 | 747.64 | 470.12 | 1.76 | 0.68 | 5.23 | 5.08 | 1.46 |
| RS/OS | 263.76 | 858.53 | 324.73 | 5.86 | 1.26 | 31.74 | 21.19 | 12.36 |
| TS200/OS | 276.73 | 864.66 | 330.35 | 6.04 | 1.06 | 32.25 | 25.18 | 9.67 |
| TS250/OS | 277.64 | 875.38 | 335.14 | 2.98 | 0.85 | 15.23 | 6.25 | 3.75 |
| TS300/OS | 278.98 | 881.76 | 428.79 | 1.23 | 0.72 | 4.82 | 0.64 | 1.29 |

$T_i$: ignition temperature (°C); $T_b$: burnout temperature (°C); $T_P$: peak temperature corresponding to maximum weight loss rate (°C); $R_p$: maximum weight loss rate; $R_{mean}$: mean weight loss rate; $D_i$: ignition index ($10^{-3}$%/min$^{-3}$); $D_b$: burnout index ($10^{-4}$%/min$^{-4}$); CPI: comprehensive pyrolysis index (10^$^{-8}$min$^{-2}$°C$^{-3}$)

### 3.3.3 Pyrolysis of individual samples

#### 3.3.3.1 Product yields distribution

**Figure 3.3** shows the product yield distribution of individual samples. As discussed in **section 2.3.3.1**, intensified torrefaction altered the pyrolysis pathway of TS to enhance char formation, consistent with the enrichment of lignin in TS 300. Whereas, slight torrefaction (200 °C) led to higher yield of gas product than RS due to the weakened interactions between hemicellulose and cellulose, and the catalytic effect from accumulated alkali metals. As opposite to RS/TS pyrolysis, char dominated the pyrolysis products distribution of OS, up to 79.91%, because of its high ash content.

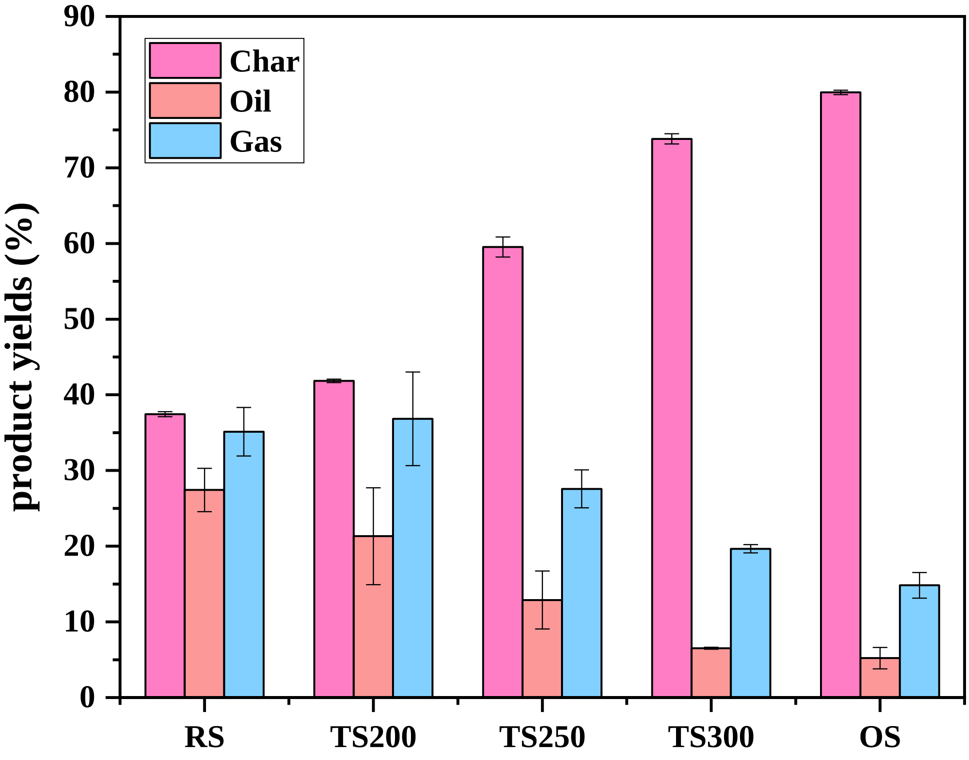

**Figure 3.3** Product yields from individual pyrolysis of RS, TS, and OS (modified from **Figure 2.8**).

### 3.3.3.2 Oil composition

The chemical composition of oil derived from pyrolysis of OS, RS, and TS is displayed in **Figure 3.4**. As discussed in **section 2.3.3.2**, torrefaction enhanced the conversion of oxygenates into hydrocarbons, such as alkanes, aromatics, and olefins, due to the removal of holocellulose and the catalytic effect of enriched alkali metals.

**Table 3.4** Relative concentrations of oxygenates in oil from OS, RS, and TS (modified from **Table 2.7**).

| | RS | TS200 | TS250 | TS300 | OS |
|---|---|---|---|---|---|
| acid | 14.72 | 13.39 | 7.83 | 0.78 | 0.62 |
| alcohol | 4.8 | 4.42 | 3.65 | 1.65 | 11.92 |
| aldehyde | 12.99 | 10.34 | 3.52 | 0 | 0.37 |
| anhydrosugars | 2.02 | 1.8 | 1.27 | 0 | 0 |
| ester | 5.52 | 4.22 | 0 | 0.57 | 0.86 |
| furan | 11.99 | 10.88 | 4.77 | 0 | 0 |
| ketone | 15.35 | 14.25 | 10.05 | 0.61 | 0.33 |
| phenol | 10.2 | 14.75 | 18.2 | 20.45 | 0 |
| ***Sum*** | 77.59 | 74.05 | 49.29 | 24.06 | 14.1 |

For pyrolysis of OS, the obtained oil was mainly compounded of hydrocarbons, up to 84.81%, exhibiting a considerably high quality compared to RS-derived oil. Meanwhile, alkane hydrocarbon was the predominant component in OS pyrolysis oil, accounting for 74.12%. Besides, some typical petroleum compounds were detected such as Cholestane and 15-Isobutyl-(13. alpha. H)-isocopalane. The concentration of oxygenated compounds in OS pyrolysis oil was relatively low and most of them were alcohol, as shown in Table 3.4.

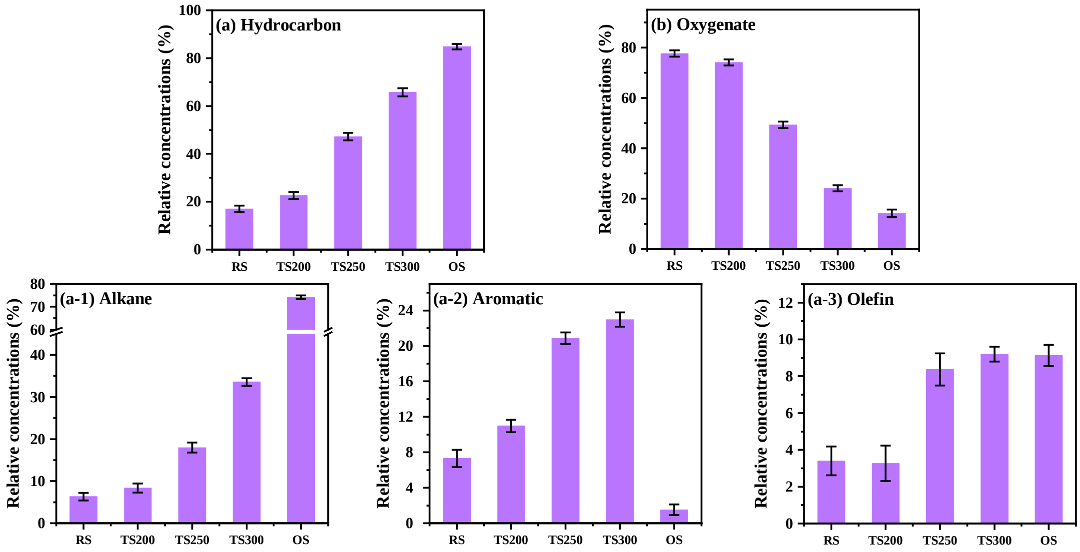

**Figure 3.4** Relative concentration of (a) hydrocarbon, (b) oxygenate, (a-1) alkane, (a-2) aromatic, and (a-3) olefin in oil products from pyrolysis of OS, RS, and TS (modified from **Figure 2.9**).

### 3.3.4 Effect of OS blending on pyrolysis of RS

#### 3.3.4.1 Product yield distribution

As mentioned in **section 3.3.3.2**, OS pyrolysis oil contained significantly higher concentration of hydrocarbons than RS pyrolysis oil. Therefore, during co-pyrolysis of OS and RS, we focus on the effect of OS blending on pyrolysis of RS (and TS in **section 3.3.5**), especially the synergistic effect on enhancing hydrocarbon production.

**Figure 3.5** shows the product yields from individual pyrolysis and co-pyrolysis of RS and OS. Meanwhile, the theoretical product yields obtained by linear calculation of individual pyrolysis results are also depicted in **Figure 3.5**. The differences between experimental yields and calculated yields were employed to investigate the interactions between RS and OS. It is observed that with increasing OS proportion in the mixture of RS and OS, the char yields increased from 47.91 to 68.63%, whereas the oil and gas yields respectively decreased from 17.82 to 10.95%, and 34.27 to 20.42%. Higher blending ratio of OS led to higher ash content in the mixture and hence, char production was enhanced while volatiles (oil and gas) generation was suppressed.

As illustrated in **Figure 3.5**, the experimental char yields were slightly lower than the calculated values, suggesting a synergy in the generation of volatiles. Moreover, the experimental oil yield was lower than the calculated yield, whereas the experimental gas yield was greater than the calculated yield, indicating the synergistic effect between RS and OS promoted the formation of gas at the expense of char and oil. Lin et al. [3-16] also reported that the synergistic effect during co-pyrolysis of rice husk and oil sludge resulted in an increase in gas products and a decrease in oil products. The synergy for enhanced gas production is primarily attributed to the radical reactions between RS and OS derivatives. RS decomposed earlier than OS (refer to **section 3.3.2**) and released a mass of free reactive radicals, such as hydroxyl radical (OH), due to the higher H/C molar ratio and abundant -OH functional group in RS; these radicals initiated the devolatilization of OS and promoted the cracking of OS-derived hydrocarbon intermediates by hydrogen abstraction, thereby the generation of light-weight components or gas was enhanced [3-17, 3-18]. The synergistic promotion of gas formation could also be ascribed to the catalytic effect from OS ash. The minerals in OS ash like CaO and MgO, were conducive to separating the organic fractions and solids and further converting organic fractions into light gases [3-19]. Meanwhile, the steam reforming reactions, and carbon reduction of metal oxides in OS (e.g., $C + H_2O \rightarrow CO + H_2$, $2Fe_3O_4 + 2CO \rightarrow 6FeO + 2CO_2$, $FeO + CO \rightarrow Fe + CO_2$, $2Fe_3O_4 + 2H_2 \rightarrow 6FeO + 2H_2O$, and $FeO + H_2 \rightarrow Fe + H_2O$) were enhanced since the presence of RS increased the carbon and oxygen content in mixtures, thereby gas production was favored [3-20]. Furthermore, alkali metals in RS, such as K and calcium (Ca), could act as catalytic agents to facilitate the secondary cracking of hydrocarbons, increasing the yield of gas products. The catalytic cracking effect of alkali metals has been widely investigated in related literature reporting co-pyrolysis of biomass and OS [3-16, 3-21].

As the blending ratio of OS increased from 25 to 75%, the synergistic reduction of char production got enhanced. This might be because a higher amount of OS introduced more minerals with catalytic ability, assisting the cracking of coke precursor into light fractions [3-11]. However, a higher proportion of OS seemed to weaken the synergistic effect between volatiles, either enhancing gas formation or inhibiting oil formation, as the differences between experimental and calculated values of oil and gas yields both decreased. A higher percentage of OS in the blends produced more hydrocarbon intermediates, however these intermediates were apt to couple together to form stable compounds as less RS provided insufficient oxygen-containing radicals to promote depolymerization of OS derivatives. Additionally, increasing amount of OS introduced excess inert ash particles, which enhanced the thermal resistance of reactants, covered the surface of reactants, and blocked the nascent pores during pyrolysis, inhibiting mass transfer and gas release. Yang et al. [3-22] also observed that a higher blending ratio of high ash coal conversely inhibited the gas production during its co-pyrolysis with cotton stalk.

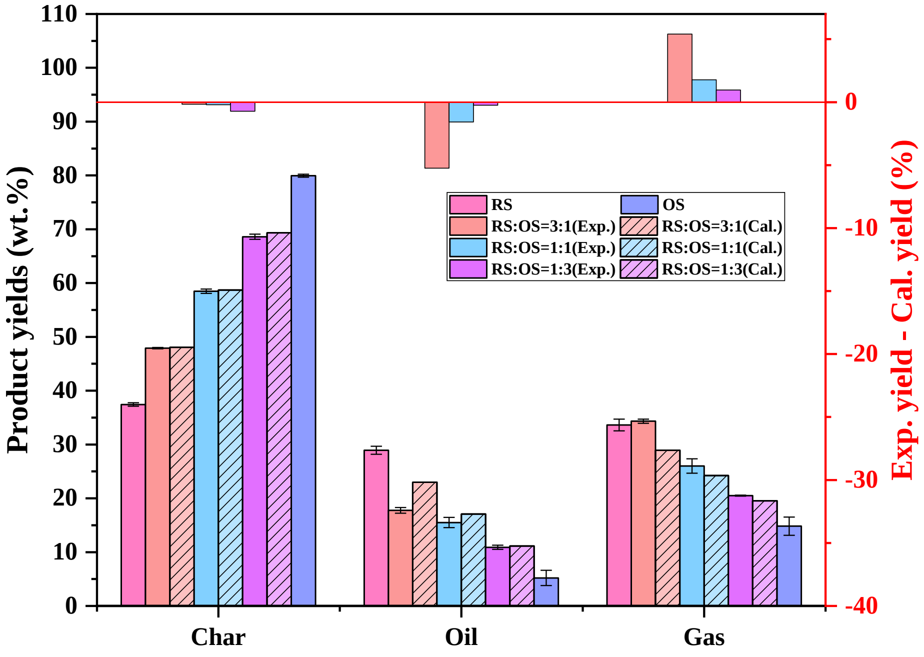

**Figure 3.5** Product yields from co-pyrolysis of OS and RS.

### 3.3.4.2 Oil composition

When OS was co-pyrolyzed with RS, an improved oil was obtained which contained higher concentration of hydrocarbons compared to RS alone, as shown in **Figure 3.6**. The incorporation of RS resulted in an increased concentration of total hydrocarbons from 53.25 to 82.27%, accompanied by a declining concentration of oxygenates from 45.99 to 17.71%. OS addition also yielded interactions that favored the production of hydrocarbons and suppressed the formation of oxygenates, as can be seen from the comparison of experimental and calculated values in **Figure 3.6 (a)** and **(b)**. The concentrations of specific oxygen-containing components obtained from co-pyrolysis of RS and OS are listed in **Table A.1** in **Appendix**. It is observed that the concentrations of acid, aldehyde, anhydrosugar, ester, furan, ketone, and phenol got reduced with increasing blending ratio of OS; concurrently, their experimental values were also basically lower than the calculated values, as depicted in **Figure 3.7**. The metal oxides such as $Al_2O_3$, $Fe_2O_3$, and CaO in OS ash could act as catalysts during pyrolysis, promoting the reduction of oxygenates in pyrolysis oil via decarboxylation, and decarbonylation reactions [3-11]. Additionally, hydrocarbon radicals evolved from OS degradation would also interact with oxygen-containing radicals (such as OH radical) from RS decomposition to yield oxygenated compounds [3-18], which could explain the enhanced alcohol formation (refer to **Figure 3.7**).

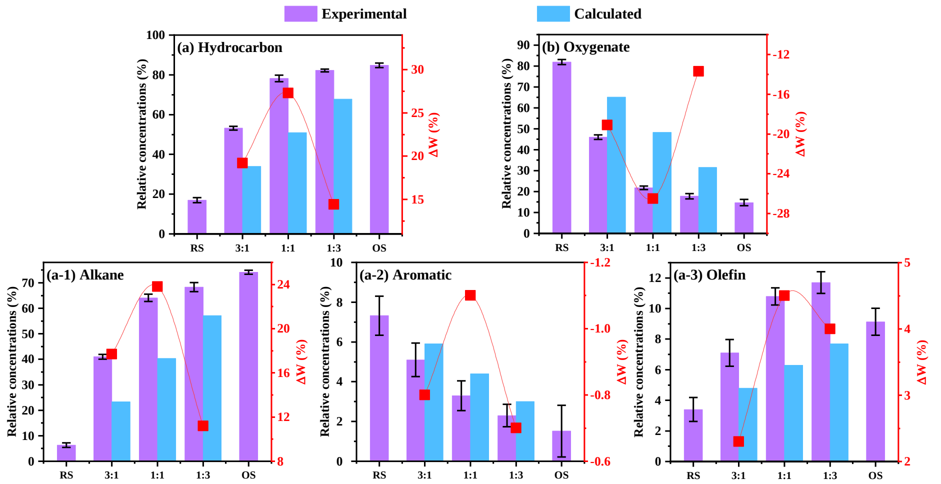

**Figure 3.6** Relative concentration of (a) hydrocarbon, (b) oxygenate, (a-1) alkane, (a-2) aromatic, and (a-3) olefin in oil products from co-pyrolysis of OS and RS.

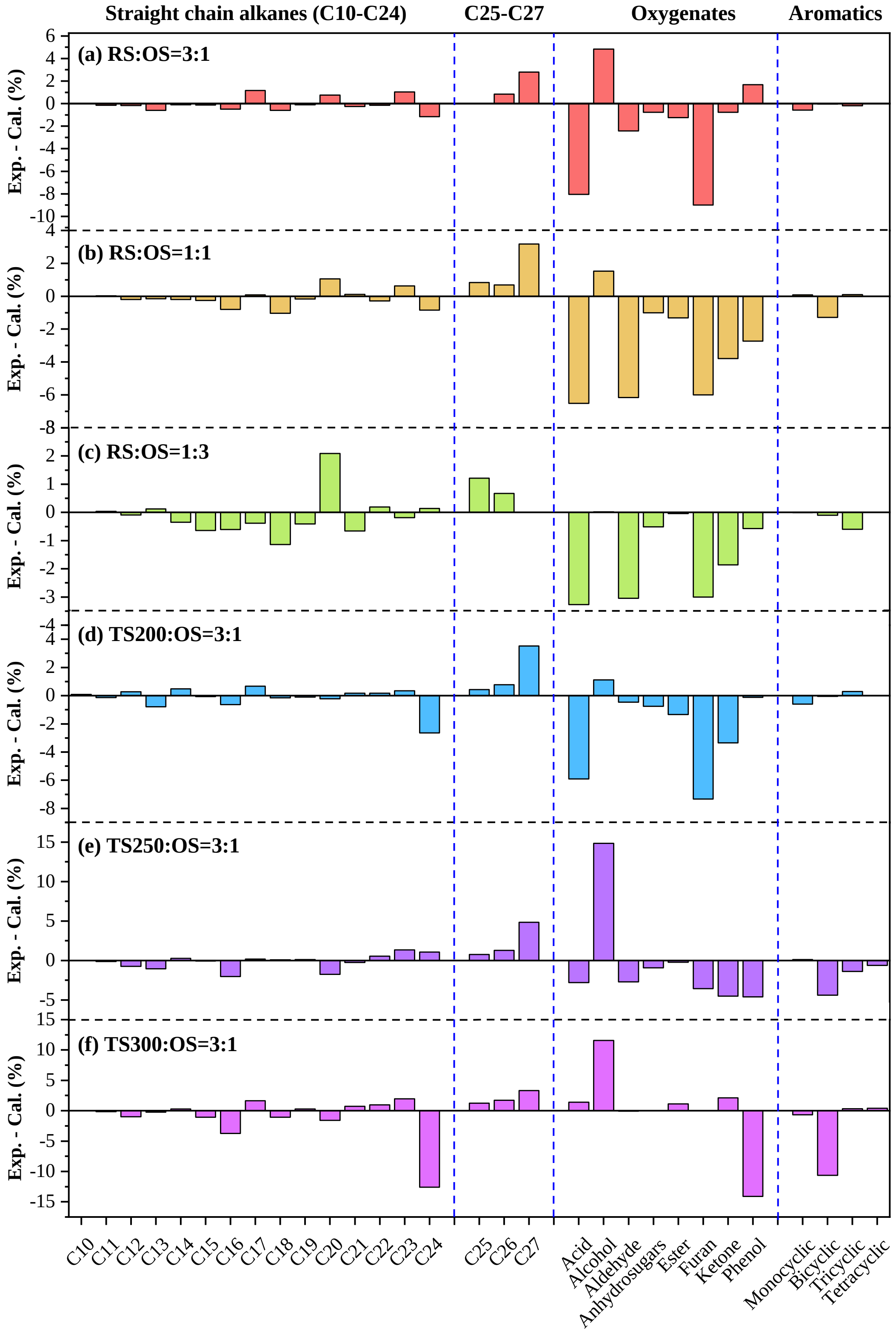

**Figure 3.7** Deviations between experimental and calculated concentrations of straight chain alkanes, oxygenates, and aromatics: (a) RS:OS=3:1, (b) RS:OS=1:1, (c) RS:OS=1:3, (d) TS200:OS=3:1, (e) TS250:OS=3:1, and (f) TS300:OS=3:1.

Among hydrocarbons, alkane dominated, and its concentration increased from 41.01

to 68.32% with an increasing proportion of OS. The addition of OS also enhanced olefin production, whereas the concentration of aromatic hydrocarbon gradually decreased from 5.05 to 2.26% when more OS particles were introduced. Overall, the composition of co-pyrolysis oil resembled that of OS oil as the blending ratio of OS increased. However, although OS addition promoted the generation of total hydrocarbons, it yielded different synergistic effects on the production of specific hydrocarbon components. As can be seen in **Figure 3.6 (a-1), (a-2),** and **(a-3)**, the experimental concentrations of alkane and olefin were higher than their calculated values, whereas the observed concentration of aromatic was lower than the calculated value under different mixing ratios, entailing that OS blending promoted the production of alkane and olefin, while inhibited the formation of aromatic. The fundamental reason was that the RS-derived oxygen-containing radicals facilitated the cracking and chain scission of OS primary pyrolysis vapors via dehydrogenation reaction, leading to enhanced formation of alkane and olefin [3-18]. Conversely, the hydrogen atoms from OS decomposition promoted the deoxidation reactions of RS-derived oxygenated compounds and enhanced hydrocarbon production [3-23]. As shown in **Table A.1** and **A.2** in **Appendix**, the experimental concentrations of light-weight straight-chain alkanes (Carbon number: C10 – C24) was lower than their calculated concentrations; in contrast, the production of heavy-weight straight-chain alkanes (Carbon number: C25 – C27) was enhanced (refer to **Figure 3.7**), implying that co-pyrolysis of RS and OS favored heavy fractions formation in oil. This could be attributed to the re-polymerization of OS-derived hydrocarbon intermediates and RS-derived hydrocarbon fragments.

**Table A.1** and **A.2** in **Appendix** also tabulate the concentration of specific aromatic hydrocarbons based on the number of aromatic rings. As observed, feeding OS into RS suppressed the formation of aromatics, either monocyclic aromatic hydrocarbons (MAHs) or polycyclic aromatic hydrocarbons (PAHs) (refer to **Figure 3.7**). It should be noted that the result in this work, OS addition inhibits aromatics production, is not in line with some relevant literature conducting co-pyrolysis of biomass and petroleum-based products, for example, cotton stalk and waste tires (WT) [3-14], and corn stalk and high-density polyethylene (HDPE) [3-23]. Their work pointed out that lignin derivatives (from biomass site) were provided with hydrogen from WT or HDPE, which suppressed their coupling and promoted the depolymerization of lignin, thereby enhancing aromatic production. Although OS blending was found to reduce aromatic production, it did not mean that OS did not supply hydrogen to accelerate the decomposition of lignin. Because these nascent aromatics may continue to undergo hydrogenation reaction with OS-derived hydrogen radicals, and then these aromatics were converted to naphthenes or olefins. Besides, OS ash contains high content of Ni element, which could catalytically promote hydrogenation of aromatics, as Ni/$SiO_2$ catalysts have been widely used for hydrogenation of heavy oil and vacuum residuum [3-24]. Previous work seldom mentioned the inherent catalytic effect of additives; therefore, the result in this work does not contradict their work.

It should be noted that in addition to Ni/$SiO_2$, some metal oxides in oil sludge ash, especially $Fe_2O_3$ (the main component of red mud), also entail outstanding hydrogenation characteristics. For example, Serrano et al. [3-25] noticed that the presence of $Fe_2O_3$ and $TiO_2$ in red mud resulted in the formation of ethylbenzene from styrene. Klopries et al. [3-26] evaluated the catalytic property of red mud for the hydro-liquefaction of rye straw via hydrogenation experiment. It was found that red mud could catalyze the liquefaction of biomass in the presence of sulfur, yielding a more significant number of C1-C4 hydrocarbons, gasoline, and heavy oils.

The RS-to-OS mass ratio plays a vital role in the degree and nature of interactions during co-pyrolysis process. The synergistically promoted generation of total hydrocarbons, alkane, and olefin increased at first and then decreased at 50% OS blending. Likewise, one to one blending ratio of RS and OS yielded the most prominent synergy facilitating the consumption of oxygenates and aromatic hydrocarbon. These results demonstrated that a 50% addition of OS might be the optimal blending ratio for higher synergy in enhanced hydrocarbon production. A higher blending ratio of OS entailed fewer oxygen-containing radicals from RS, and hence, the radical reactions were suppressed, and hydrocarbon formation cannot be promoted. On the other hand, excess OS inevitably introduced a large number of inert ash particles other than hydrocarbon intermediates and catalytic metal oxides, which inhibited the mass and energy transfer; this result was consistent with the severe hindering of gas production at 75% OS addition.

### 3.3.5 Combined effect of torrefaction and OS blending on pyrolysis of RS

#### 3.3.5.1 Product yield distribution

The combined effect of torrefaction and OS blending (RS/TS:OS = 3:1) on product yield distribution is illustrated in **Figure 3.8**. As torrefaction temperature increased from 0 to 300 °C, the char yield of the blends proportionally increased from 47.91 to 75.93%, while the oil yield and gas yield decreased from 17.82 to 6.23% and 34.27 to 17.85%, respectively. Obviously, OS addition did not change the effect of torrefaction temperature on the product yield distribution (refer to **Figure 3.3**). It is noticed that the experimental char yields under different torrefaction temperatures were close to the calculated values, demonstrating weak interaction. However, the deviations between experimental values and calculated values of oil and gas products were apparent, and the synergistic effect can be classified into two groups: (1) the interactions between RS/OS and TS200/OS inhibited oil production while promoted gas formation, and conversely (2) the interactions between TS250/OS and TS300/OS promoted oil production while inhibited gas formation. It is reasonably inferred that torrefaction conditions determined the synergistic effect in product yields, and severe torrefaction turned the synergistic effect from favoring gas products to promoting oil generation.

As discussed in **section 3.3.4.1**, the radical reactions between RS-derived oxygenates and OS-derived hydrocarbon intermediates, the catalytic effect from metal oxides in OS ash and alkali metals in RS promoted gas production. Torrefaction under 200 °C marginally altered the properties of RS, resulting in similar fundamental properties in TS200 and RS, thus, the interactions remained the same as that between RS and OS.

Nonetheless, 200 °C torrefaction slightly lowered the degree of synergy since the partial removal of holocellulose undermined the radical reactions enhancing gas formation.

When OS was blended into co-pyrolysis with TS250 or TS300, contrary synergy was obtained. Severe torrefaction significantly altered the properties of biomass, lowering the volatile content, reducing H/C molar ratio, and decreasing the intensity of -OH functional group. Herein, the radical reactions favoring gas production were weakened. Intensified torrefaction led to accumulation of lignin in TS250 and TS300; accordingly, the decomposition of lignin was predominant during pyrolysis of TS250 and TS300, and a lot of phenolic radicals were produced due to aryl ether linkage cleavage. Thereafter, these radicals were prone to combine with each other via rearrangement reactions and form stable C-C bonds if insufficient hydrogen radicals were provided nearby, leading to a higher degree of reticulation and to a higher thermal residence of the residue, and thereby the further degradation of lignin was hindered [3-14]. The thermogravimetric analysis in **section 3.3.2** revealed that the main decomposition temperature ranges of TS250 and TS300 were close to that of OS compared to RS and TS200, implying intense radical reactions between TS250/OS and TS300/OS. The decomposition of OS provided free hydrogen radicals due to its relatively higher H/C molar ratio than TS250 and TS300. These free hydrogen radicals stabilized phenolic radicals, preventing their mutual combination, which promoted depolymerization of lignin and enhanced oil production. As for the promoting effect of minerals (alkali metals in RS) on gas generation, it might be weakened due to their reactions with $SiO_2$ to form aluminosilicates, which conversely suppressed the synergistic effect. Qin et al. [3-27] observed that alkali metals in corn straw reacted with $SiO_2$ and $Al_2O_3$ in coal ash under 600 °C, producing $K(AlSi_3O_8)$, $Ca(Al_2Si_2O_8)$, and $KAl(SO_4)_2(H_2O)_{12}$, inhibiting gas formation. **Figure 3.9** shows the XRD patterns of OS and char samples. The peak intensity of $SiO_2$ in OS got weakened after its co-pyrolysis with biomass, especially with TS under severe torrefaction, which confirmed the reactions between alkali metals and $SiO_2$.

In general, higher torrefaction temperature led to more minor differences between experimental and calculated oil and gas yields, entailing weaker interactions. Intensified torrefaction resulted in increased ash and reduced volatiles, which further inhibited mass and gas transfer, thereby suppressing the interactions.

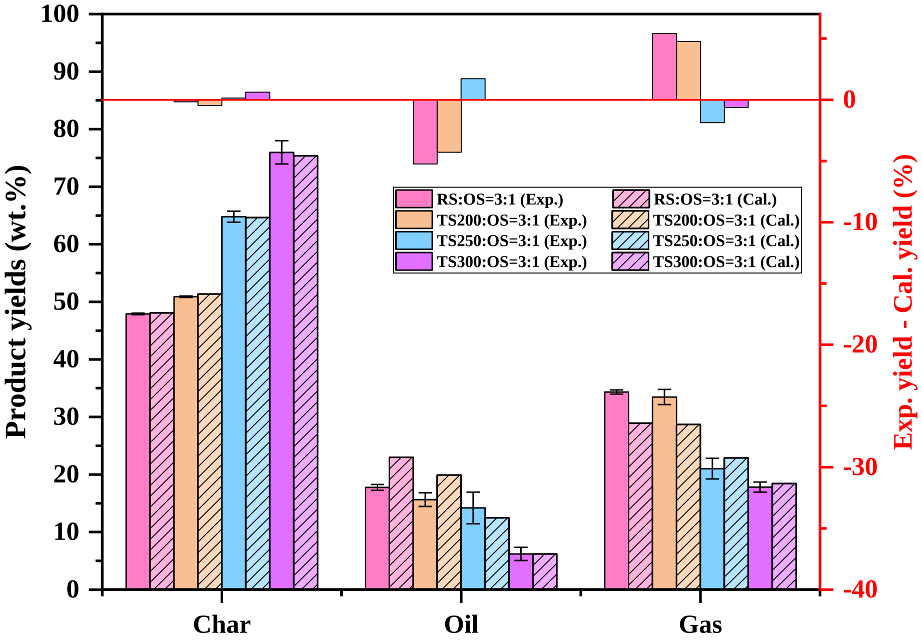

**Figure 3.8** Product yields from co-pyrolysis of RS-OS mixture and TS-OS mixtures.

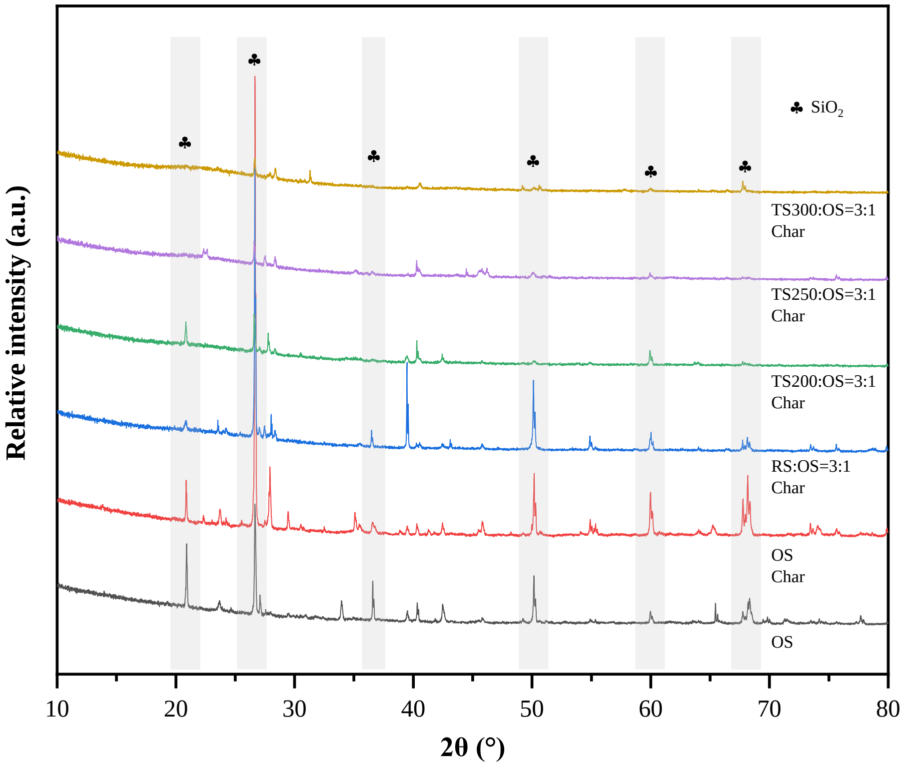

**Figure 3.9** XRD patterns of OS and char samples.

### 3.3.5.2 Oil composition

**Figure 3.10** indicates that enhanced torrefaction led to an increase in the concentration of total hydrocarbons and to a decline in the concentration of oxygenates compared to co-pyrolysis of RS and OS, which followed the effect of torrefaction on RS pyrolysis oil composition. The experimental concentration of total hydrocarbons was superior to the calculated values, whereas the experimental concentration of oxygenates was inferior to the calculated values, indicating that torrefaction did not alter the promoting effect of OS blending on the conversion of oxygenates to hydrocarbons. However, higher torrefaction temperature weakened the synergy in hydrocarbon production, as the differences between experimental and calculated values became smaller. This is because severe torrefaction significantly reduced the amount of holocellulose, leading to insufficient oxygen-containing radical sinks, and hence, fewer hydrocarbons were generated via radical reactions or deoxygenation reactions. As listed in **Table A.2** in **Appendix**, the reduction of acid, aldehyde, anhydrosugars, ester, furan, ketone, and phenol were witnessed with increasing torrefaction temperature due to the promotion of deoxygenation from torrefaction and OS blending (refer to **section 2.3.3.2** and **3.3.4.2**).

As shown in **Figure 3.10 (a-1)**, Compared to RS/OS co-pyrolysis, oil derived from TS/OS co-pyrolysis contained a higher concentration of alkanes while with a gradually declined synergy in alkane production as torrefaction intensified, following the same variation trend as the concentration of total hydrocarbons. Moreover, **Figure 3.7** and **Table A.2** in **Appendix** indicate the deviations between experimental and calculated concentrations of heavy-weight straight-chain alkanes in TS/OS-derived oil were more prominent than in RS/OS-derived oil, implying enhanced radical reactions resulted from torrefaction. **Figure 3.10 (a-2)** and **(a-3)** demonstrate that OS blending altered the variation trend of aromatic and olefin concentration in TS under the studied torrefaction temperature range. As shown in **Figure 3.10 (a-3)**, the oil obtained from co-pyrolysis of TS200/OS and TS250/OS had slightly lower concentrations of olefins than that from RS/OS-derived co-pyrolysis oil; concurrently, the corresponding synergy for olefins production decreased from 2.32 to -3.71%, suggesting hindering effects. This might be because TS-derived olefin radicals were consumed via Diels-Alder reactions with OS-derived hydrocarbon intermediates to form alkanes [3-23]. As indicated in **Figure 3.10 (a-2)**, inhibition in aromatic production was observed, and higher torrefaction temperature yielded stronger inhibition as their experimental concentrations were exceedingly lower than the calculated values. Therefore, it could be reasoned that severe torrefaction (300 ° C) enhanced the hydrogenation and ring-opening of aromatics to form alkanes and olefins during co-pyrolysis of RS and OS.

This work aims to recover high-quality oil products (hydrocarbon-rich) from oil sludge and biomass using thermochemical treatments. To achieve this, we measured the content of oil yields and the concentration of typical components in the oil. As shown in **Table 3.5**, the specific masses of hydrocarbons were obtained according to the mass of raw samples, oil yields, and hydrocarbon concentrations. It could be noticed that torrefaction promoted the hydrocarbon recovery rate, whereas severe torrefaction (300 °C) limited the recovery rate due to the meager oil yield. Similarly, co-pyrolysis of TS300 and OS under a blending ratio of 3:1 resulted in a relatively low hydrocarbon recovery rate compared to other cases of co-pyrolysis. The addition of OS significantly increased the concentration of hydrocarbons in oil products, thereby enhancing the hydrocarbon recovery rate at least two times higher. Under the same blending ratio of 3:1, torrefaction (200 and 250 °C) led to a higher concentration of hydrocarbons with a lower oil yield; thus, the hydrocarbon recovery rate marginally altered. Overall, co-pyrolysis of RS and OS under a 1:1 blending ratio yielded the highest hydrocarbon recovery rate, which can be determined as the optimal parameter for hydrocarbon recovery.

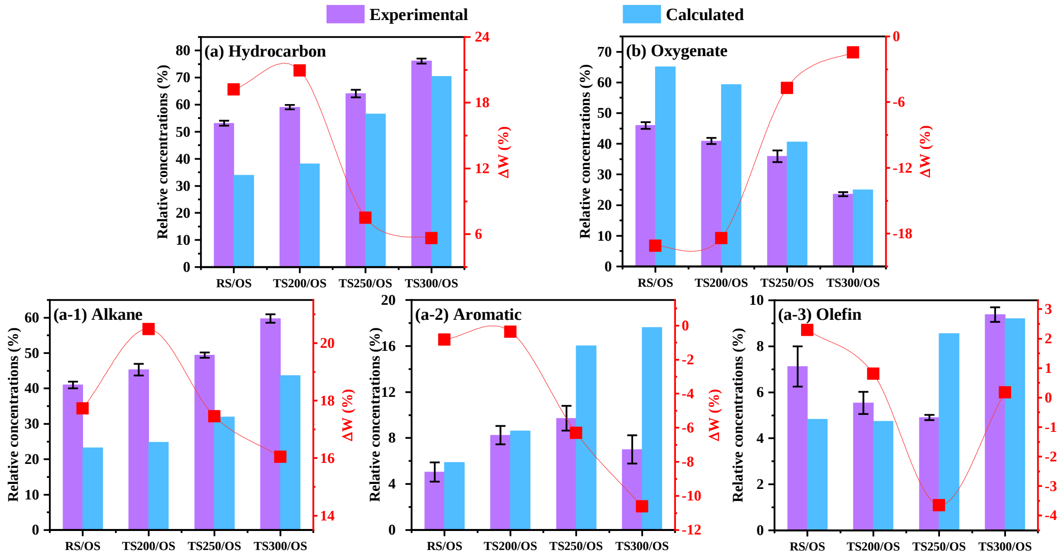

**Figure 3.10** Relative concentration of (a) hydrocarbon, (b) oxygenate, (a-1) alkane, (a-2) aromatic, and (a-3) olefin in oil products from co-pyrolysis of RS-OS mixture and TS-OS mixtures.

**Table 3.5** Mass distribution of oil and hydrocarbons

| | Mass of raw sample (g) | Oil yield (%) | Hydrocarbon concentration (%) | Mass of hydrocarbons (g) [a] | Hydrocarbon recovery rate (%) [b] |
|---|---|---|---|---|---|
| RS | 5.00 | 27.43 | 17.03 | 0.234 | 1 |
| TS200 | 5.00 | 21.33 | 22.61 | 0.241 | 102.93 |
| TS250 | 5.01 | 12.89 | 47.20 | 0.305 | 130.13 |
| TS300 | 4.99 | 6.52 | 65.75 | 0.214 | 91.32 |
| OS | 4.99 | 5.21 | 84.80 | 0.220 | 94.22 |
| RS:OS=3:1 | 5.01 | 17.76 | 53.20 | 0.473 | 202.33 |
| RS:OS=1:1 | 5.00 | 15.50 | 78.20 | 0.605 | 258.70 |
| RS:OS=1:3 | 5.00 | 10.90 | 82.20 | 0.448 | 191.25 |
| TS200:OS=3:1 | 5.02 | 15.63 | 59.08 | 0.464 | 198.15 |
| TS250:OS=3:1 | 4.97 | 14.19 | 64.09 | 0.452 | 193.14 |
| TS300:OS=3:1 | 5.00 | 6.21 | 76.13 | 0.236 | 100.87 |

[a] Mass of hydrocarbons = Mass of raw sample × Oil yield × Hydrocarbon concentration × 10-4

[b] Hydrocarbon recovery rate = Mass of hydrocarbons (exclude RS) / mass of hydrocarbons (RS) *100

## 3.6 Possible reaction mechanism during co-pyrolysis of RS/OS and TS/OS

Based on the above analyses and the results of previous work, the possible synergistic mechanism and reaction pathways during co-pyrolysis of RS/TS and OS were summarized in **Figure 3.11**. Low thermal stability led to earlier decomposition of RS during co-pyrolysis of RS and OS, releasing adequate oxygen-containing radicals (such as OH radicals), which stimulated the degradation of OS; moreover, these radicals could accelerate the cracking of OS-derived primary vapors via dehydrogenation reaction (Pathway 1), thereby enhancing the production of light gases, alkanes, and olefins. Thereafter, the hydrogen atoms from OS degradation conversely facilitated the deoxidation of RS-derived oxygenates; the metal oxides such as $Al_2O_3$, $Fe_2O_3$, and CaO in OS ash could also catalytically enhance decarboxylation, and decarboxylation reactions of RS-evolved oxygenates, converting oxygenates to hydrocarbons (Pathway 2). Simultaneously, the hydrocarbon intermediates evolved from OS would interact with RS-derived oxygen-containing radicals or hydrocarbon fragments to form oxygenates or heavy-weight straight-chain alkanes (Pathway 3). When the temperature increased above 400 °C, decomposition of OS dominated, and multiple hydrocarbon radicals and hydrogen atoms were produced. These radicals interacted with RS derivatives, suppressing their coupling to form oxygenates, MAHs, or PAHs. For example, the hydrogen atoms supplied by OS stabilized the phenolic radicals from RS, promoting the depolymerization of lignin (Pathway 4). Moreover, these hydrogen atoms significantly strengthened the hydrogenation and ring-opening reactions of aromatic structures (Pathway 5), leading to enhanced production of alkanes and olefins at the expense of aromatics. The synergistic Pathway 5 was also catalytically enhanced by $Ni/SiO_2$ particles in OS ash. Besides, OS-derived hydrocarbon intermediates and lignin-derived alkyl radicals were re-polymerized to form heavy-weight straight-chain alkanes (Pathway 6). A higher blending ratio of OS yielded weaker synergy for gas production and hydrocarbon formation due to the introduced excessive inert ash particles acting as physical barriers to mass and heat transfer during co-pyrolysis.

Torrefaction partially removed hemicellulose and cellulose in RS, accompanied by the enrichment of lignin and alkali metals. Consequently, TS pyrolysis yielded a higher concentration of hydrocarbons, and their co-pyrolysis with OS further enhanced hydrocarbon production. However, fewer organics in TS provided insufficient oxygen-containing radicals (mainly derived from the decomposition of holocellulose), weakening the radical reactions between TS and OS. Hence, the gas formation and the synergy for hydrocarbon production were suppressed. Severe torrefaction resulted in close decomposition temperature ranges between TS300 and OS, entailing an intensive interaction. As a consequence, the depolymerization of lignin was promoted, the hydrogenation and ring-opening of lignin-derived aromatic structure got enhanced, and the re-polymerization of OS-evolved hydrocarbon intermediates and lignin-derived alkyl radicals were strengthened, leading to the increase in production of alkanes and olefins and the decrease in generation of aromatics.

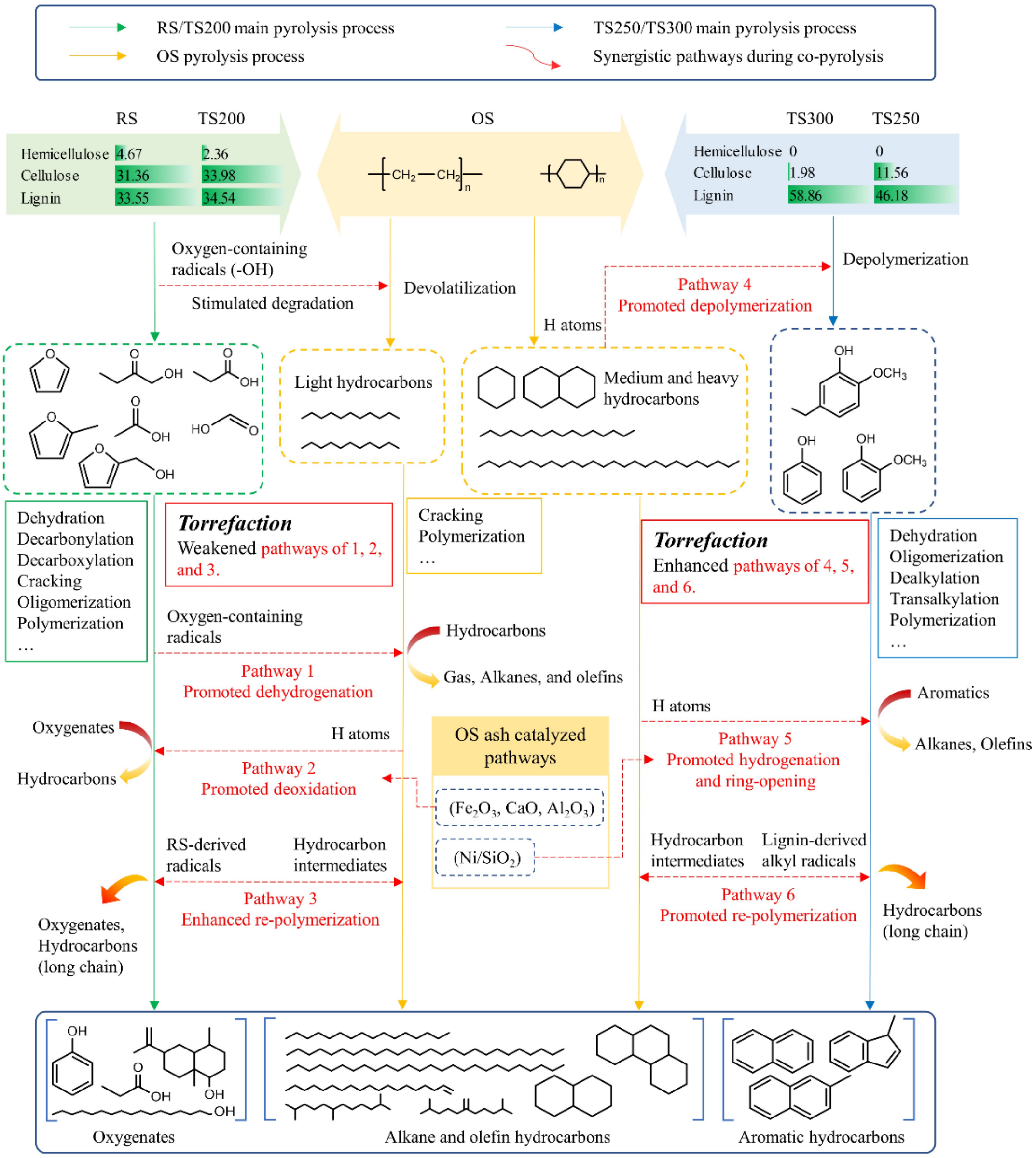

**Figure 3.11** Possible synergistic pathways in co-pyrolysis of RS and OS, TS and OS.

## 3.4 Conclusions

In this work, pyrolysis of OS and RS/TS in a thermogravimetric analyzer and a fixed bed reactor was investigated.

(1) Co-pyrolysis of OS and RS promoted char conversion to volatiles, especially gas products.

(2) The incorporation of OS into either RS or TS promoted hydrocarbon production at the expense of oxygenates. A significant synergistic effect was witnessed in

enhancing hydrocarbon production after OS addition.

(3) RS/OS mass ratio of 1:1 was a critical point considering the degree of promoting the formation of hydrocarbons. A higher blending ratio of OS hindered mass and heat transfer, thereby suppressing the gas formation and lowering the synergy for hydrocarbon generation.

(4) Severe torrefaction increased TS's main decomposition temperature range close to that of OS, and positive synergistic effects for oil generation were observed when OS was blended into TS obtained at 250 and 300 °C.

(5) A notable result in this work is that OS addition supplied ample hydrogen atoms and Ni/$SiO_2$ minerals, which further promoted the hydrogenation and ring-opening of aromatic structures, enhancing alkane and olefin formation at the consumption of aromatics.

## References

[3-1] Chen, W., Chen, Y., Yang, H., Xia, M., Li, K., Chen, X., & Chen, H. (2017). Co-pyrolysis of lignocellulosic biomass and microalgae: products characteristics and interaction effect. Bioresource technology, 245, 860-868.

[3-2] Kan, T., Strezov, V., & Evans, T. J. (2016). Lignocellulosic biomass pyrolysis: A review of product properties and effects of pyrolysis parameters. Renewable and sustainable energy reviews, 57, 1126-1140.

[3-3] Wang, X., Deng, S., Tan, H., Adeosun, A., Vujanović, M., Yang, F., & Duić, N. (2016). Synergetic effect of sewage sludge and biomass co-pyrolysis: a combined study in thermogravimetric analyzer and a fixed bed reactor. Energy conversion and management, 118, 399-405.

[3-4] Zhang, W., Yuan, C., Xu, J., & Yang, X. (2015). Beneficial synergetic effect on gas production during co-pyrolysis of sewage sludge and biomass in a vacuum reactor. Bioresource Technology, 183, 255-258.

[3-5] Martínez, J. D., Veses, A., Mastral, A. M., Murillo, R., Navarro, M. V., Puy, N., ... & García, T. (2014). Co-pyrolysis of biomass with waste tyres: Upgrading of liquid bio-fuel. Fuel Processing Technology, 119, 263-271.

[3-6] Lee, H. W., Kim, Y. M., Jae, J., Jeon, J. K., Jung, S. C., Kim, S. C., & Park, Y. K. (2016). Production of aromatic hydrocarbons via catalytic co-pyrolysis of torrefied cellulose and polypropylene. Energy Conversion and Management, 129, 81-88.

[3-7] Bu, Q., Chen, K., Xie, W., Liu, Y., Cao, M., Kong, X., ... & Mao, H. (2019). Hydrocarbon rich bio-oil production, thermal behavior analysis and kinetic study of microwave-assisted co-pyrolysis of microwave-torrefied lignin with low density polyethylene. Bioresource technology, 291, 121860.

[3-8] Huang, S., Qin, J., Chen, T., Yi, C., Zhang, S., Zhou, Z., & Zhou, N. (2022). Co-pyrolysis of different torrefied Chinese herb residues and low-density polyethylene: Kinetic and products distribution. Science of The Total Environment, 802, 149752.

[3-9] Lee, H. W., Kim, Y. M., Lee, B., Kim, S., Jae, J., Jung, S. C., ... & Park, Y. K. (2018). Catalytic copyrolysis of torrefied cork oak and high density polyethylene over a mesoporous HY catalyst. Catalysis Today, 307, 301-307.

[3-10] Cheng, S., Takahashi, F., Gao, N., Yoshikawa, K., & Li, A. (2016). Evaluation of oil sludge ash as a solid heat carrier in the pyrolysis process of oil sludge for oil production. Energy & Fuels, 30(7), 5970-5979.

[3-11] Cheng, S., Wang, Y., Gao, N., Takahashi, F., Li, A., & Yoshikawa, K. (2016). Pyrolysis of oil sludge with oil sludge ash additive employing a stirred tank reactor. Journal of Analytical and Applied Pyrolysis, 120, 511-520.

[3-12] Liu, H., Hong, R., Xiang, C., Wang, H., Li, Y., Xu, G., ... & Zhu, K. (2020). Thermal decomposition kinetics analysis of the oil sludge using model-based method and model-free method. Process Safety and Environmental Protection, 141, 167-177.

[3-13] Singh, B., Singh, S., & Kumar, P. (2021). In-depth analyses of kinetics,

thermodynamics and solid reaction mechanism for pyrolysis of hazardous petroleum sludge based on isoconversional models for its energy potential. Process Safety and Environmental Protection, 146, 85-94.

[3-14] Khan, S. R., Zeeshan, M., & Masood, A. (2020). Enhancement of hydrocarbons production through co-pyrolysis of acid-treated biomass and waste tire in a fixed bed reactor. Waste Management, 106, 21-31.

[3-15] Khan, S. R., & Zeeshan, M. (2022). Catalytic potential of low-cost natural zeolite and influence of various pretreatments of biomass on pyro-oil up-gradation during co-pyrolysis with scrap rubber tires. Energy, 238, 121820.

[3-16] Lin, B., Huang, Q., & Chi, Y. (2018). Co-pyrolysis of oily sludge and rice husk for improving pyrolysis oil quality. Fuel processing technology, 177, 275-282.

[3-17] Song, Y., Tahmasebi, A., & Yu, J. (2014). Co-pyrolysis of pine sawdust and lignite in a thermogravimetric analyzer and a fixed-bed reactor. Bioresource technology, 174, 204-211.

[3-18] Liu, X., Burra, K. R. G., Wang, Z., Li, J., Che, D., & Gupta, A. K. (2021). Towards enhanced understanding of synergistic effects in co-pyrolysis of pinewood and polycarbonate. Applied Energy, 289, 116662.

[3-19] Li, J., Zheng, F., Li, Q., Farooq, M. Z., Lin, F., Yuan, D., ... & Chen, G. (2022). Effects of inherent minerals on oily sludge pyrolysis: Kinetics, products, and secondary pollutants. Chemical Engineering Journal, 431, 133218.

[3-20] Zhu, J., Zhu, L., Guo, D., Chen, Y., Wang, X., & Zhu, Y. (2020). Co-pyrolysis of petrochemical sludge and sawdust for syngas production by TG-MS and fixed bed reactor. International Journal of Hydrogen Energy, 45(55), 30232-30243.

[3-21] Hu, G., Li, J., Zhang, X., & Li, Y. (2017). Investigation of waste biomass co-pyrolysis with petroleum sludge using a response surface methodology. Journal of environmental management, 192, 234-242.

[3-22] Yang, P., Zhao, S., Zhang, Q., Hu, J., Liu, R., Huang, Z., & Gao, Y. (2021). Synergistic effect of the cotton stalk and high-ash coal on gas production during co-pyrolysis/gasification. Bioresource Technology, 336, 125336.

[3-23] He, T., Zhong, S., Liu, C., Shujaa, A., & Zhang, B. (2021). Enhancing hydrocarbon production via ex-situ catalytic co-pyrolysis of biomass and high-density polyethylene: Study of synergistic effect and aromatics selectivity. Waste Management, 128, 189-199.

[3-24] Cheng, S., Li, A., & Yoshikawa, K. (2015). High quality oil recovery from oil sludge employing a pyrolysis process with oil sludge ash catalyst. International Journal of Waste Resources, 5(2), 656-660.

[3-25] Serrano, D. P., Aguado, J., & Escola, J. M. (2000). Catalytic conversion of polystyrene over HMCM-41, HZSM-5 and amorphous $SiO_2$–$Al_2O_3$: comparison with thermal cracking. Applied Catalysis B: Environmental, 25(2-3), 181-189.

[3-26] Klopries, B., Hodek, W., & Bandermann, F. (1990). Catalytic hydroliquefaction of biomass with red mud and CoO MoO3 catalysts. Fuel, 69(4), 448-455.

[3-27] Qin, Q., Zhou, J., Lin, B., Xie, C., & Zhou, L. (2020). Influence of coal ash on the characteristics of corn straw pyrolysis products. Bioresource Technology, 318, 124055.

# Chapter 4 Co-combustion of oil sludge char with raw/hydrothermally treated biomass: interactions, kinetics, and mechanisms

## 4.1 Introduction

The results in **Chapter 2** and **Chapter 3** demonstrated that adding biomass/torrefied biomass into co-pyrolysis with oil sludge (OS) could enhance the oil production and the hydrocarbon concentration in oil was synergistically promoted. Consequently, the economic value of oil was improved, and its utilization could compensate for the energy consumption of the integrated pyrolysis and combustion system. Moreover, the second section of this approach, combustion of oil sludge char (OSC), is also an inevitable and effective means of harmless disposal and energy production. Previous studies pointed out that recycling oil sludge ash as a catalyst for oil sludge pyrolysis and incorporating steam injection could potentially allow the integrated process to be a self-sufficient system, as well as realizing efficient energy recovery [4-1]. However, OSC itself poses a low calorific value, and a large amount of additional energy is consumed for combustion treatment, which reduces this approach's economic benefit. To address the limitation, co-combustion with biomass is cost-effective and promising.

Nonetheless, to the best of the author’s knowledge, current research on the co-combustion of OSC and biomass is limited to raw biomass utilization to improve the combustion characteristics of OSC [4-2, 4-3]. The interactive mechanisms of OSC/biomass co-combustion, such as the nature of synergy/inhibition that occurs during co-combustion of OSC/biomass, are still uncertain. Furthermore, the alkali metals in biomass could also act as catalysts during co-combustion in addition to causing fouling and slagging problems [4-4]. Hydrothermal treatment (HTT) can partially remove alkali metals and convert materials into hydrochars with ameliorated homogeneity and higher fuel properties [4-5]. Therefore, the incorporation of hydrochars into co-combustion with OSC could improve the combustion efficiency, and the removal of alkali metals after HTT might help identify the interactive mechanisms of OSC co-combustion with biomass when compared with OSC solo-combustion and OSC/rawbiomass co-combustion. On the other hand, kinetic analysis of OSC/biomass co-combustion is a prerequisite to understanding reaction-based mechanisms and scaling them up for industrial applications, which still needs more in-depth investigation.

Thermogravimetric analysis (TGA) is one of the most used techniques to rapidly investigate and provide a quantitative method for detailed observation of thermal events and kinetics during solid fuel combustion, such as coal and biomass [4-6, 4-7]. The information obtained from TGA combustion profiles could be used to predict industrial-scale combustion. Although TGA cannot be directly extrapolated to other equipment at a larger scale, it is beneficial to offer fundamental referential opinions for implementing and optimizing the co-combustion field [4-8]. In this Chapter, the TGA analysis was used to analyze the combustion behaviors of OSC, biomass, hydrochar, and their respective blends (OSC/biomass and OSC/hydrochar). As illustrated in **Figure 4.1**, the morphological structure and alkali metals concentration of biomass before and after hydrothermal treatment was evaluated to investigate the effect of alkali metal on co-combustion. The interactions between two blends were studied under different blending ratios. The interactive mechanisms of OSC co-combustion were analyzed via kinetics and discussed to further comprehend biomass-supported combustion of poorly combustible materials like OSC.

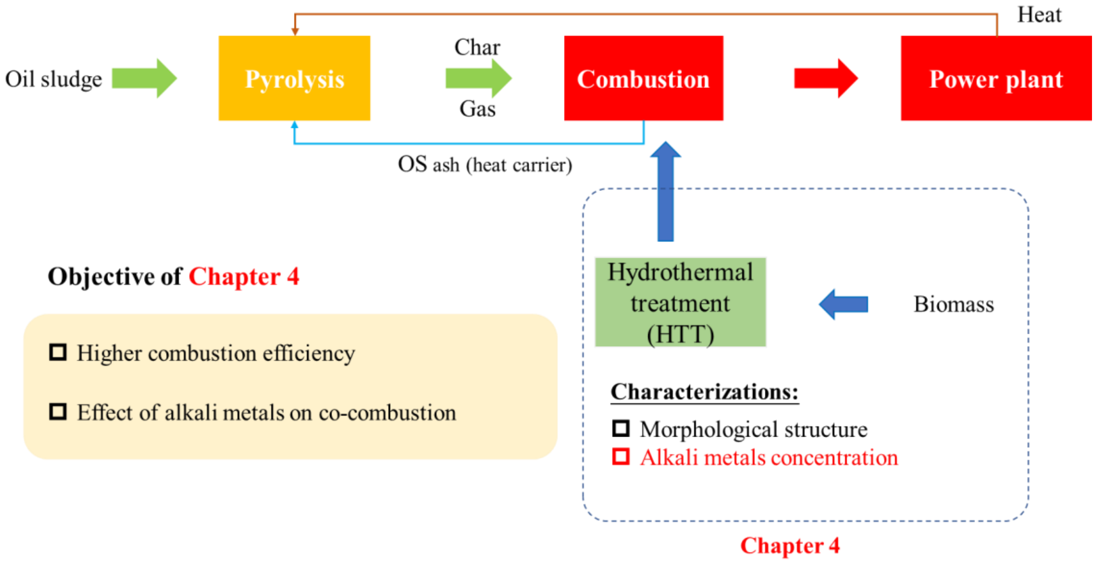

**Figure 4.1** Structure of Chapter 4.

## 4.2 Materials and methods

### 4.2.1 Sample preparation

OS samples were supplied by Zhejiang Eco-Environmental Technology Co., Ltd, China. OSC samples were obtained by pyrolysis of OS. Pyrolysis experiments were performed in a vertical tube furnace and details were outlined in **Chapter 2** and **3**. In each experiment, 20 g of OS was first placed in the pyrolysis reactor and then nitrogen gas was purged for 20 min to create an oxygen-free environment. Thereafter, the reactor was heated from room temperature to 450 °C at 10 °C/min and maintained for 20 min. When the heating process was finished, the reactor was naturally cooled to room temperature with the continuous nitrogen purge, and finally the OSC was taken out and stored in a desiccator. Our previous research indicated that 450 °C was an optimal temperature for OS pyrolysis to obtain high-quality oil and save energy [4-9]. Cherry blossom wood chips, purchased from a gardening market in Japan, was selected for its low moisture, low ash, and high volatile content. The addition of woody biomass can significantly improve the combustion efficiency of oil sludge char, simultaneously mitigating the ash-related problems.

### 4.2.2 Sample characterizations

All OSC, RW, and hydrothermally treated wood (HW) samples were crushed and sieved smaller than 200 μm for subsequent experiments. The proximate analysis was performed on an elemental analyzer (Vario Microcube, Bruker, Germany), and the ultimate analysis was measured by a muffle furnace according to GB/T212-2008. The higher heating value of samples were calculated using **eq 1** which was developed by Francis and Lloyd [4-10]:

$$HHV = 357.8C + 1135.6H + 54.9N + 119.5S - 85.4O - 974 \qquad (1)$$

Where C, H, N, O, and S denoted the weight percentages of carbon, hydrogen, nitrogen, sulfur, and oxygen, respectively.

The ash composition of samples was measured by XRF (S2 Ranger Bruker, Japan) analysis with X-ray tube of Palladium. The morphological surface characteristics of samples were observed via a scanning electron microscopy (JSM-6510LA, JEOL Ltd., Japan) with an acceleration voltage of 6 kV.

For convenience, the blend of OSC and RW were named OSC/RW. OSC/HW represents the blend of OSC and HW. According to blending ratio, OSC/RW blends were tagged as OSC/RW28 (20% OSC and 80% RW), OSC/RW55 (50% OSC and 50% RW), and OSC/RW82 (80% OSC and 20% RW), respectively. OSC/HW blends were also tagged as OSC/HW28, OSC/HW55, and OSC/HW82, respectively. Pyrolysis led to the evaporation of most organic components and accumulation of ash in OS, therefore, the combustion efficiency of OSC was extremely low. In this study, the analyses of OSC/RW82 and OSC/HW82 were still performed for a comprehensive understanding of the interactive mechanisms during co-combustion, though the combustion efficiency was lower due to the high proportion of OSC.

### 4.2.3 Experimental equipment and methods

As shown in **Figure 4.2**, HTT experiments were conducted in a 400 ml stainless steel reactor, and HTT steps were reported in detail previously [4-11, 4-12]. 6 g of RW and 60 g of pure water were mixed as raw samples. The hydrolysis of lignocellulose interfered with the carbonization process when the hydrothermal temperature was lower than 200 °C, whereas the hydrochar yield was reduced at a temperature above 250 °C [4-13]. Therefore, the reaction temperature was set at 220 °C in this study.

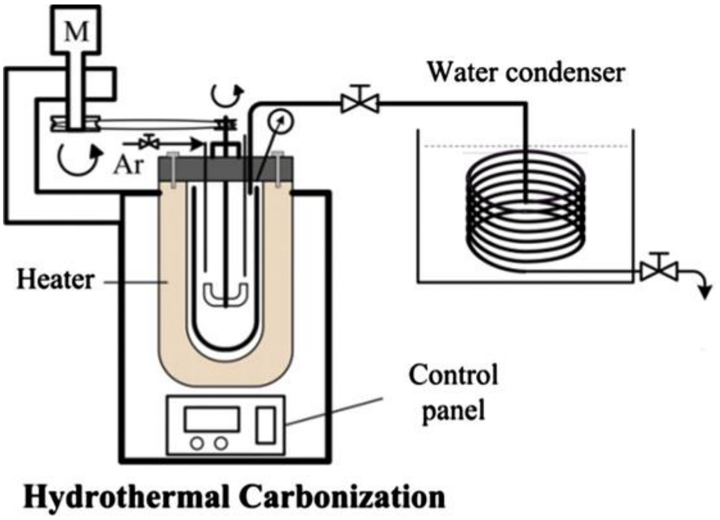

**Figure 4.2** Schematic diagram of HTT reactor [modified from Ref. 4-12]

Non-isothermal experiments were performed using a differential thermogravimetric analyzer (TA-60WS, Shimadzu, Japan). 10 ± 0.5 mg of a sample was put on the bottom of an $Al_2O_3$ crucible and then set in the TGA analyzer with an empty $Al_2O_3$ reference for baseline calibration. The sample was heated from ambient temperature to 1000 °C under an air atmosphere at 60 ml/min flow rate and different heating rates (5, 10, 40, and 50 °C/min). Each experiment was conducted twice or more for repeatability validation.

### 4.2.4 Combustion performance analysis

For combustion performance analysis, ignition temperature ($T_i$), burnout temperature ($T_b$), and peak temperature ($T_{max}$) were obtained from the thermogravimetry and differential thermogravimetry (TG-DTG) curves. $T_i$ was determined by the tangent method [4-14]. $T_b$ and $T_{max}$ represented the temperature at the conversion rate of 98% and the maximum weight loss rate, respectively [4-15]. Moreover, the ignition index

($D_i$), burnout index ($D_b$), and comprehensive combustion index (CCI) were determined to evaluate the combustion performance of tested samples. These indexes were calculated by following formulas (**eqs 2-4**) [4-16]:

$$D_i = \frac{-R_p}{t_i \times t_p} \tag{2}$$

$$D_b = \frac{-R_p}{\Delta t_{1/2} \times t_p \times t_b} \tag{3}$$

$$CCI = \frac{(-R_p) \times (-R_{mean})}{T_i^2 \times T_b} \tag{4}$$

where $R_p$ was the maximum weight loss rate (unit: %/min), $R_{mean}$ was the average weight loss rate (unit: %/min), and $t_i$, $t_p$, $t_b$, and $\Delta t_{1/2}$ represented ignition time, peak time, burnout time, and time interval between half value of $R_p$, respectively (unit: min).

### 4.2.5 Interaction analysis

To evaluate the interactions between two blends during the co-combustion, the theoretical DTG curves were calculated based on their decomposition data and compared with experimental curves. The theoretical DTG curves were calculated by the average weight of the individual samples, according to **eq 5**:

$$DTG_{cal} = Xrw \cdot DTG_{RW}\ (Xhw \cdot DTG_{HW}) + Xosc \cdot DTG_{OSC} \tag{5}$$

$$\Delta W = DTG_{exp} - DTG_{cal} \tag{6}$$

$$MR = \frac{\left(\sum_{i=1}^{n}\left(x_{i,exp} - x_{i,cal}\right)\right)}{n \cdot x_{mean,\ cal}} \tag{7}$$

where $DTG_{RW}$, $DTG_{HW}$, and $DTG_{OSC}$ were the weight loss rate of RW, HW, and OSC, respectively (unit: %/min). The $Xrw$, $Xhw$, and $Xosc$ were the proportion of RW, HW, and OSC in the blends, respectively (unit: %). The interaction index, $\Delta W$, was the difference between experimental and theoretical weight loss rate (unit: %/min). If $\Delta W < 0$, it indicates a positive interaction for combustion at a specific temperature.

The interaction index MR (mean of the absolute error between experimental and calculated value divided by the mean of the calculated value) was used to analyze that the interaction during the whole process is positive or not. If MR > 0, representing a positive interaction, otherwise, a negative interaction.

### 4.2.6 Kinetic analysis

#### 4.2.6.1 Introduction of conventional kinetic analysis

The reaction rate of samples was described as [4-17]:

$$\frac{d\alpha}{dt} = k(T)\ f(\alpha) \tag{8}$$

where $d\alpha/dt$ was the conversion rate; $\alpha$ was the conversion degree; t was the reaction time; $T$ was the reaction temperature; $f(\alpha)$ was the differential form of reaction model; $k(T)$ was the rate constant relating to temperature and was determined by the Arrhenius equation [4-17]:

$$k(T) = A\exp(-\frac{E}{RT}) \tag{9}$$

where E, A, and R were the apparent activation energy, the pre-exponential factor, and the universal gas constant (8.314 J/(K·mol)), respectively.

The conversion degree of each stage was described as [4-18]:

$$\alpha_s = \frac{m_s - m_t}{m_s - m_{s+1}}\ (s = 1, 2) \tag{10}$$

where $m_s$, $m_t$, and $m_{s+1}$ were the initial weight, the weight at time t, and the final weight in a certain stage, respectively.

Combining **eqs 8** and **9**, the reaction rate could be transformed into:

$$\beta\frac{d\alpha}{dT} = A\exp(-\frac{E}{RT})f(\alpha) \tag{11}$$

where $\beta$ represented the heating rate and $\beta = dT/dt$.

Thereafter, **eq 11** could be transferred into:

$$G(\alpha) = \int_0^{\alpha} \frac{d\alpha}{f(\alpha)} = \frac{A}{\beta} \int_{T_0}^{T} \exp(-\frac{E}{RT})\, dT \tag{12}$$

where $G(\alpha)$ represented the integral form of the reaction function $f(\alpha)$, as exhibited in **Table 4.1**.

**Table 4.1** Most frequently used models of solid-state processes.

| **Models** | **Symbol** | $f(\alpha)$ | $G(\alpha)$ |
|---|---|---|---|
| ***Order of reaction*** | | | |
| First order | $F_1$ | $1-\alpha$ | $-\ln(1-\alpha)$ |
| Second order | $F_2$ | $(1-\alpha)^2$ | $(1-\alpha)^{-1}-1$ |
| Third order | $F_3$ | $(1-\alpha)^3$ | $[(1-\alpha)^{-2}-1]/2$ |
| ***Diffusion*** | | | |
| One-way transport | $D_1$ | $0.5\alpha$ | $\alpha^2$ |
| Two-way transport | $D_2$ | $[-\ln(1-\alpha)]^{-1}$ | $(1-\alpha)\ln(1-\alpha)+\alpha$ |
| Three-way transport | $D_3$ | $1.5(1-\alpha)^{2/3}[1-(1-\alpha)^{1/3}]^{-1}$ | $[1-(1-\alpha)^{1/3}]^2$ |
| Ginstling-Brounshtein equation | $D_4$ | $1.5[(1-\alpha)^{-1/3}-1]^{-1}$ | $(1-2\alpha/3)-(1-\alpha)^{2/3}$ |
| ***Limiting surface reaction between both phase*** | | | |
| One dimension | $R_1$ | $1$ | $\alpha$ |
| Two dimensions | $R_2$ | $2(1-\alpha)^{1/2}$ | $1-(1-\alpha)^{1/2}$ |
| Three dimensions | $R_3$ | $3(1-\alpha)^{2/3}$ | $1-(1-\alpha)^{1/3}$ |
| ***Exponential nucleation*** | | | |
| Power law, n=1/2 | $P_2$ | $2\alpha^{1/2}$ | $\alpha^{1/2}$ |
| Power law, n=1/3 | $P_3$ | $3\alpha^{2/3}$ | $\alpha^{1/3}$ |
| Power law, n=1/4 | $P_4$ | $4\alpha^{3/4}$ | $\alpha^{1/4}$ |
| ***Random nucleation and nuclei growth*** | | | |
| Two-dimensional | $A_2$ | $2(1-\alpha)[-\ln(1-\alpha)]^{1/2}$ | $[-\ln(1-\alpha)]^{1/2}$ |
| Three-dimensional | $A_3$ | $3(1-\alpha)[-\ln(1-\alpha)]^{2/3}$ | $[-\ln(1-\alpha)]^{1/3}$ |

### 4.2.6.2 Model-free methods

The iso-conversional methods had been frequently used to estimate the reaction kinetics of solid fuels without referring to the reaction mechanism. In this study, Flynn-Wall-Ozawa (FWO) method and Kissinger-Akahira-Sunose (KAS) method were applied to calculate the apparent activation energy for combustion.

The FWO method was expressed as:

$$\ln(\beta) = \ln[\frac{AE}{RG(\alpha)}] - 5.331 - 1.052\frac{E}{RT} \tag{13}$$

The KAS method was described as:

$$\ln(\frac{\beta}{T^2}) = \ln[\frac{AR}{EG(\alpha)}] - \frac{E}{RT} \tag{14}$$

For a certain α, the apparent activation energy, E, was calculated depending on the slopes of the fitted straight line by plotting $\ln(\beta)$ versus $1/T$ for the FWO method and $\ln(\beta/T^2)$ versus $1/T$ for the KAS method, respectively.

### 4.2.6.3 Master plot methods

In this study, the integral master plot method was employed to determine the kinetic model of various decomposition stages for samples. The starting decomposition rate of samples was slow, and thus the conversion degree $\alpha$ was close to zero at the initial temperature $T_0$, so **eq 12** could be transferred as follows:

$$G(\alpha) = \int_0^\alpha \frac{d(\alpha)}{f(\alpha)} = \frac{A}{\beta}\int_{T_0}^{T} \exp\left(-\frac{E}{RT}\right)dT \approx \frac{A}{\beta}\int_0^T \exp\left(-\frac{E}{RT}\right)dT = \frac{AE}{\beta R}P(u) \tag{15}$$

where $u = E/RT$ and $P(u)$ was determined by the empirical equation, $P(u) = \exp(-u)/u \times (1.00198882u + 1.87391198)$ [4-19]. From iso-conversional methods, the $E$ value was estimated and used to determine a proper reaction model by simulating TG data. Taking $\alpha = 0.5$ as a reference, **eq 15** could be transformed into:

$$G(0.5) = \frac{AE}{\beta R}P(u_{0.5}) \tag{16}$$

Where $G(0.5)$ denoted the integral of reaction model at $\alpha=0.5$, $u_{0.5}=E/RT_{0.5}$, $T_{0.5}$ was the temperature at $\alpha=0.5$. Dividing **eq 15** by **eq 16**, the integral master plots can be further converted to:

$$\frac{G(\alpha)}{G(0.5)} = \frac{P(u)}{P(u_{0.5})} \tag{17}$$

On the left side of **eq 17**, the theoretical master plots, $G(\alpha)/G(0.5)$ versus $\alpha$, were obtained from various $G(\alpha)$ functions. The experimental plots, $P(u)/P(u_{0.5})$ versus

$\alpha$, were calculated from TG data and located on the right side of **eq 17**. By calculating the deviation between experimental plots and theoretical plots, the best fitted model was identified to determine the dominant combustion mechanisms of different samples.

## 4.3 Results and discussion

### 4.3.1 Characterization of samples

The proximate and ultimate analysis results are shown in **Table 4.2**. HW had higher fixed carbon and lower volatile content compared to RW due to the hydrolysis of hemicellulose, which enriched energy-dense cellulose and lignin during HTT [4-20]. The ultimate analysis indicated that the C and H contents increased at the expense of O after HTT. Correspondingly, the O/C and H/C ratios of HW both decreased, which indicated that HW had a higher energy density due to the lower bonding energies of C-H and C-O bonds than that of C-C bonds [4-21]. The Van Krevelen's diagram further illustrated that the dehydration reaction was the governing reaction pathway, as shown in **Figure 4.3**. Moreover, it could be observed that the S content in HW was significantly reduced, consequently the reduction of $SO_x$ emission during HW combustion was expected. These results were consistent with previous studies [4-20, 4-22]. Compared to raw OS samples, OSC contained much lower C, H, O, volatiles, and fixed carbon due to the expulsion of petroleum hydrocarbons and oxygenates during pyrolysis process. However, the S content in OSC was still higher because some of S-containing substances remain in the form of sulfides in the char products [4-23].

**Table 4.2** Proximate and ultimate analyses of samples.

| Analysis | OS | OSC | RW | HW |
|---|---|---|---|---|
| Ultimate analysis (wt%, dry basis) | | | | |
| C | 19.67 | 4.90 | 47.38 | 52.78 |
| H | 2.66 | 0.67 | 5.46 | 5.57 |
| N | 0.29 | 0.10 | 0.06 | 0.14 |
| S | 0.85 | 0.78 | 0.10 | 0.02 |
| O[1] | 4.13 | 2.15 | 46.70 | 41.29 |
| Ash[2] | 72.40 | 91.40 | 0.30 | 0.20 |
| O/C | 0.16 | 0.33 | 0.74 | 0.59 |
| H/C | 1.62 | 1.64 | 1.38 | 1.27 |
| HHV[3] | 8.85 | 1.46 | 18.21 | 20.72 |
| Proximate analysis (wt%, as received basis) | | | | |
| Moisture content | 1.51 | 0 | 8.59 | 1.97 |
| Volatiles | 21.73 | 6.77 | 86.07 | 81.61 |
| Fixed carbon | 4.27 | 0.85 | 5.17 | 15.88 |
| Ash content | 72.49 | 92.38 | 0.17 | 0.54 |

[1] O%=100%-C%-H%-N%-S%-Ash%; [2] obtained from elemental analyzer; [3] higher heating value (MJ/mol).

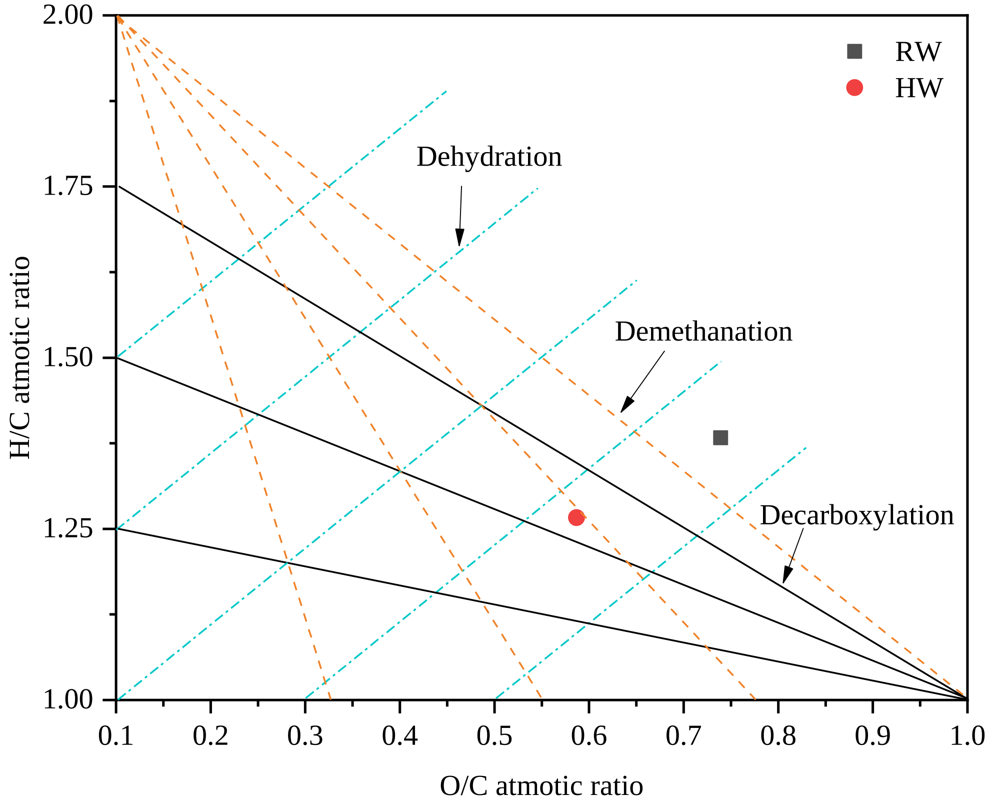

**Figure 4.3** Van Krevelen diagram of RW and HW.

### 4.3.2 Combustion behavior of OSC, RW, and HW

The combustion experiments were performed at a heating rate of 40 °C/min, and their

TG and DTG curves were presented in **Figure 4.4 (a-1)**. It should be noted that the combustion profiles obtained from TGA referred to the volatile release. **Figure 4.4 (a-2)** shows the combustion process of OSC could be divided into three stages. The first stage (280-600 °C) represented the evaporation of volatiles mainly consisting of heavy organic components. Light compounds were already decomposed and evaporated from oil sludge in the previous pyrolysis process [4-24]. The second stage (600-750°C) was ascribed to the combustion of non-volatile compounds (high-boiling point) and fixed carbons. Moreover, calcium carbonate ($CaCO_3$) undergoes thermal decomposition between 650 and 800 °C (**eq 18**), forming calcium oxide (CaO) and carbon dioxide ($CO_2$), which was consistent with the CaO content in **Table 4.4** [4-25]. The last stage (750-940°C) was associated with the decomposition of inorganic matters like carbonate or sulfate minerals, such as potassium carbonate and potassium sulfate, as shown in below reactions [4-25, 4-26].

$$CaCO_3\ (s) \rightarrow CaO\ (s) + CO_2\ (s) \tag{18}$$

$$K_2CO_3\ (s) \rightarrow K_2O\ (s) + CO_2\ (g) \tag{19}$$

$$K_2SO_4\ (s, l) \rightarrow K_2O\ (s) + CO_2\ (g) + \frac{1}{2}O_2\ (g) \tag{20}$$

**Table 4.3** Ash composition of samples by XRF analysis (wt%).

| | $SiO_2$ | $Fe_2O_3$ | $SO_3$ | $Al_2O_3$ | CaO | $K_2O$ | $Na_2O$ | Other |
|---|---|---|---|---|---|---|---|---|
| OSC | 50.41 | 12.50 | 11.93 | 9.84 | 7.62 | 3.51 | 1.37 | 2.82 |

| | K | Fe | S | Cu | Other |
|---|---|---|---|---|---|
| RW | 23.60 | 6.43 | 5.35 | 6.22 | 58.40 |
| HW | 7.71 | 5.12 | 5.80 | 1.11 | 80.26 |

**Figure 4.4 (a-1)** indicated that the combustion of RW and HW proceeded along two main stages, identified by two prominent DTG peaks, where the first stage and the second stage (stage 1 and stage 2) were associated to the devolatilization and the combustion of fixed carbon, respectively. The slight slope of the decomposition peak at around 300 °C for RW combustion was disappeared for HW due to the degradation of hemicellulose during HTT [4-20]. Correspondingly, HW had slightly higher ignition temperature, lower peak temperature, and lower weight loss rate in stage 1, as listed in

**Table 4.4**. However, the second stage of HW combustion was extended to higher temperature region with an increasing burnout temperature compared to RW, even though the corresponding weight loss rates of the two showed little difference. It was resulted from the formation of hard solid substances containing strongly bonded cellulose, lignin, and insoluble particles through recombination reactions during HTT [4-20]. It should be noted that the temperature range of stage 1 and stage 2 of RW or HW were within that of OSC. Therefore, HW could continuously release heat during co-combustion, representing a more adequate synergistic behavior, which was beneficial for the co-combustion. Compared with RW and HW, OSC exhibited inferior combustion properties with a lower degradation rate and longer reaction time. Therefore, the addition of RW and HW can effectively address the drawbacks of OSC combustion.

**Table 4.4** Combustion characteristics of OSC, RW, HW, and blends at 40 °C/min.

| Sample | $T_i$ | $T_b$ | S1 | | S2 | | $(dw/dt)_{mean}$ |
|---|---|---|---|---|---|---|---|
| | | | $T_1$ | $(dw/dt)_1$ | $T_2$ | $(dw/dt)_2$ | |
| RW | 307.14 | 536.82 | 343.94 | 49.71 | 490.74 | 9.70 | 4.10 |
| OSC/RW28 | 309.84 | 542.03 | 343.89 | 41.19 | 486.74 | 7.66 | 3.38 |
| OSC/RW55 | 312.22 | 651.77 | 344.43 | 23.70 | 510.27 | 4.08 | 1.90 |
| OSC/RW82 | 315.22 | 704.65 | 347.22 | 12.87 | 498.62 | 2.70 | 1.12 |
| HW | 308.54 | 620.60 | 326.51 | 49.20 | 563.36 | 9.44 | 4.10 |
| OSC/HW28 | 308.32 | 593.87 | 325.97 | 40.46 | 545.16 | 8.63 | 3.28 |
| OSC/HW55 | 308.08 | 606.95 | 325.94 | 26.08 | 553.64 | 6.82 | 2.31 |
| OSC/HW82 | 314.43 | 724.32 | 333.54 | 10.16 | 513.14 | 3.38 | 1.10 |
| OSC | 420.34 | 916.64 | 485.46 | 1.73 | / | / | 0.31 |

S1: stage 1; S2: stage 2; $T_i$: ignition temperature (°C); $T_b$: burnout temperature (°C); $T_1$ and $T_2$: peak temperature in stage 1 and stage 2 (°C); $(dw/dt)_1$, $(dw/dt)_2$, and $(dw/dt)_{mean}$: the maximum weight loss rate in stage 1, the maximum weight loss rate in stage 2, and the mean weight loss rate during the whole combustion process, respectively.

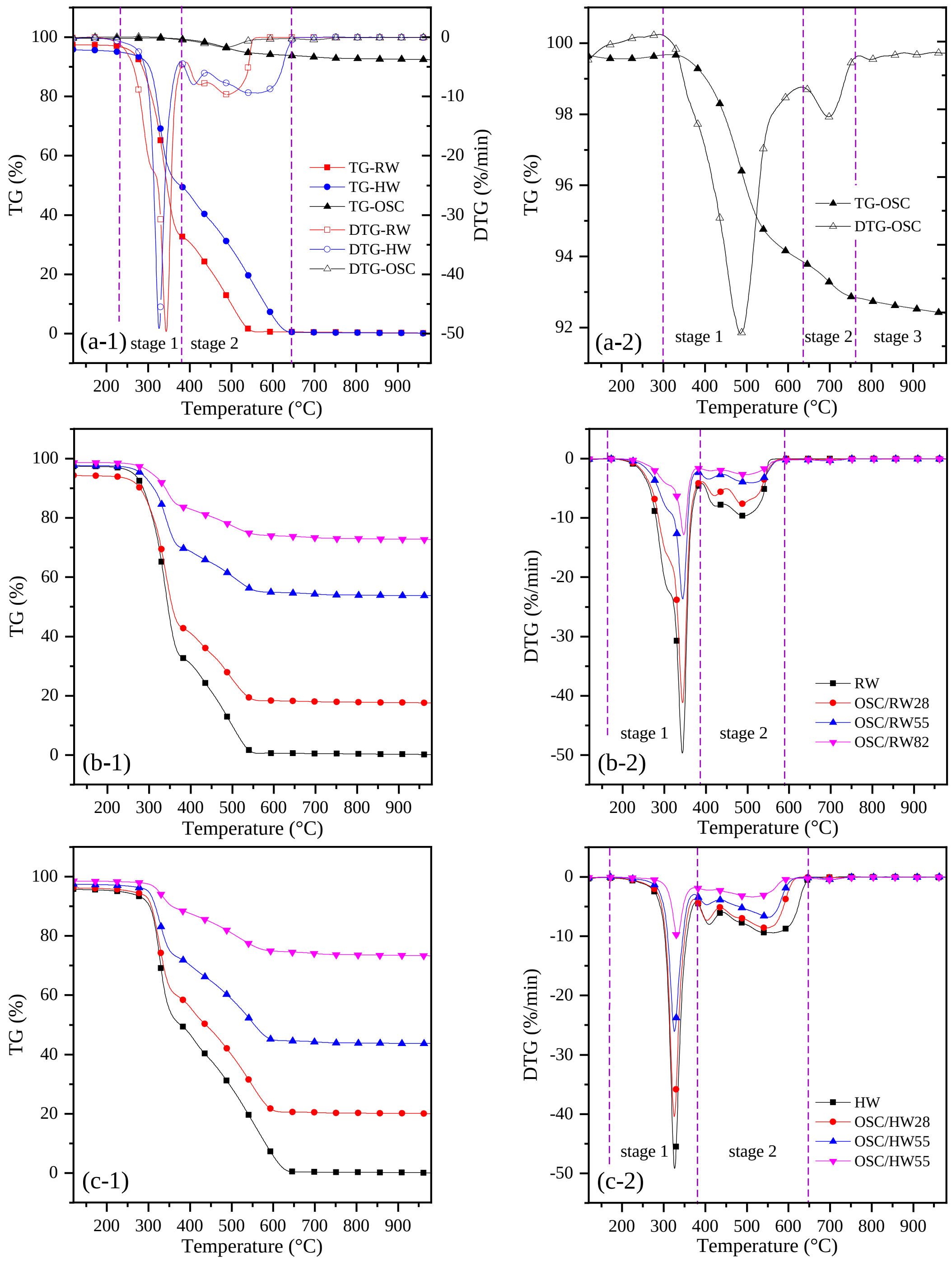

**Figure 4.4** TG and DTG curves of OSC, RW, HW, and their respective blends at 40 ° C/min (a-1) TG and DTG of RW, HW, and OSC; (a-2) TG and DTG of OSC; (b-1) TG of RW and OSC/RW; (b-2) DTG of RW and OSC/RW; (c-1) TG of HW and OSC/HW; (c-2) DTG of HW and OSC/HW.

### 4.3.3 Combustion behavior of the blends

Combustion of the blends was performed at the heating rate of 40 °C/min, and the decomposition curves were shown in **Figure 4.4**. According to **Figures 4.4 (b-1)** and

**(b-2)**, OSC/RW blends showed similar degradation curves with RW. The decomposition rates of OSC/RW blends decreased with the increase of OSC proportion both in stage 1 and stage 2. Meanwhile, the peak temperature in stage 1 remained constant within 343.89 to 347.22 °C. Moreover, **Figure 4.4 (b-2)** indicated that the OSC addition prolonged the reaction time in stage 2 and resulted in a higher burnout temperature (see **Table 4.4**). As presented in **Figures 4.4 (c-1)** and **(c-2)**, the OSC addition gave a similar effect on HW's thermal decomposition with that on RW combustion, lowering the decomposition rate and reducing the combustion reactivity. The reduction of combustion efficiency for OSC/RW and OSC/HW might be ascribed to the ash originally contained in OSC, which accounted for extra energy consumption. It is noteworthy that the reaction time of OSC/HW was shortened compared with HW, and the burnout temperature of OSC/HW28 (593.87°C) and OSC/HW55 (606.95°C) was lower than that of HW (620.6°C).

**Table 4.5** Combustion performance parameters of OSC, RW, HW, and blends at 40 °C/min.

| Sample | $D_i$ | $D_b$ | CCI |
|---|---|---|---|
| RW | 9.54 | 62.58 | 40.25 |
| OSC/RW28 | 7.83 | 56.12 | 26.76 |
| OSC/RW55 | 4.46 | 29.18 | 7.09 |
| OSC/RW82 | 2.37 | 14.89 | 2.06 |
| HW | 9.97 | 66.77 | 34.14 |
| OSC/HW28 | 8.23 | 61.32 | 23.51 |
| OSC/HW55 | 5.31 | 33.45 | 10.46 |
| OSC/HW82 | 1.96 | 11.25 | 1.56 |
| OSC | 0.16 | 0.25 | 0.03 |

$D_i$: ignition index ($10^{-1}$%/min$^3$); $D_b$: burnout index ($10^{-2}$%/min$^4$); CCI: comprehensive combustion index ($10^{-7}$%$^2$/min$^2$°C$^3$).

**Table 4.5** presented several combustion performance parameters to comprehensively illustrate combustion behaviors of blended samples. The ignition index ($D_i$), burnout index ($D_b$), and comprehensive combustion index (CCI) values of OSC were increased after blending with RW or HW, suggesting a promoting effect of RW and HW on OSC combustion performance. On the other hand, no significant differences in the combustion performance parameters were found between OSC/RW and OSC/HW, which implied that hemicellulose decomposition and partial removal of alkali metals by HTT gave an insignificant impact on the co-combustion performance evaluated by these indices. This proposed that similar interactions in OSC co-combustion between RW and HW were expected. It would be discussed in the next section.

### 4.3.4 Interactions during combustion of the blends

#### 4.3.4.1 The interaction between OSC and RW

According to **Figure 4.5 (a-1)**, experimental curves of weight loss rate in stage 1 were mostly above the calculated curves. It means that experimental weight loss rate was smaller than the predicted rate at specified temperature range. **Figure 4.5 (a-2)** further shows the $\Delta W$ ($\Delta W = \mathrm{DTG}_{\mathrm{exp}} - \mathrm{DTG}_{\mathrm{cal}}$) values of OSC/RW with different OSC proportions were mainly positive in stage 1 and stage 2, suggesting negative interactions to the co-combustion. Zhang et al. [4-27] reported similar results for co-combustion between coal gangue and pine sawdust. It was noteworthy that the $\Delta W$ values at the temperature range of 530-575 °C were exceptionally negative, representing a positive interaction at this temperature range. According to **Figure 4.5 (a-1)**, however, the reaction time was prolonged in this temperature interval, which indicated more energy consumption. Therefore, it could be concluded that interactions between OSC/RW co-combustion were mostly negative. Alkali metals in RW were regarded as positive for co-combustion owing to their catalytic properties [4-28, 4-29]. However, this study demonstrated that the promoting effect of alkali metals during co-combustion might be weakened by ash-rich materials like OSC. The alkali metals easily reacted with the ash and formed amorphous matrices such as aluminosilicate. It would decrease the catalytic performance of alkali metals, block pore structure of reactants, and subsequently decrease heat transfer and gas penetration [4-28]. Yao et al. [4-30] observed the similar phenomenon during co-combustion of oil shale and its hydrothermally treated hydrochar. High contents of alkali metals could react with ash to produce eutectic substances leading to melt-inducing slagging, which reduced the weight loss rate and lowered the corresponding temperature. Furthermore, **Figure 4.5 (c-1)** indicates that OSC/RW55 posed the lowest MR value in stage 1 and stage 2, exhibiting the strongest inhibiting interaction behaviors. This was resulted from the maximum formation of non-catalytic aluminosilicate in OSC/RW55. It consumed catalytic alkali metals in RW and catalytic metal oxides in the ash of OSC, thus finally reduced co-combustion support from alkali metals and metal oxides. When RW or OSC blending ratio is higher (OSC/RW28 or OSC/RW82), alkali metals or metal oxides, which were not consumed after aluminosilicate formation, could support co-combustion. It would mitigate negative interaction in co-combustion. Negative interaction between OSC and RW is discussed further in **section 4.3.6**.

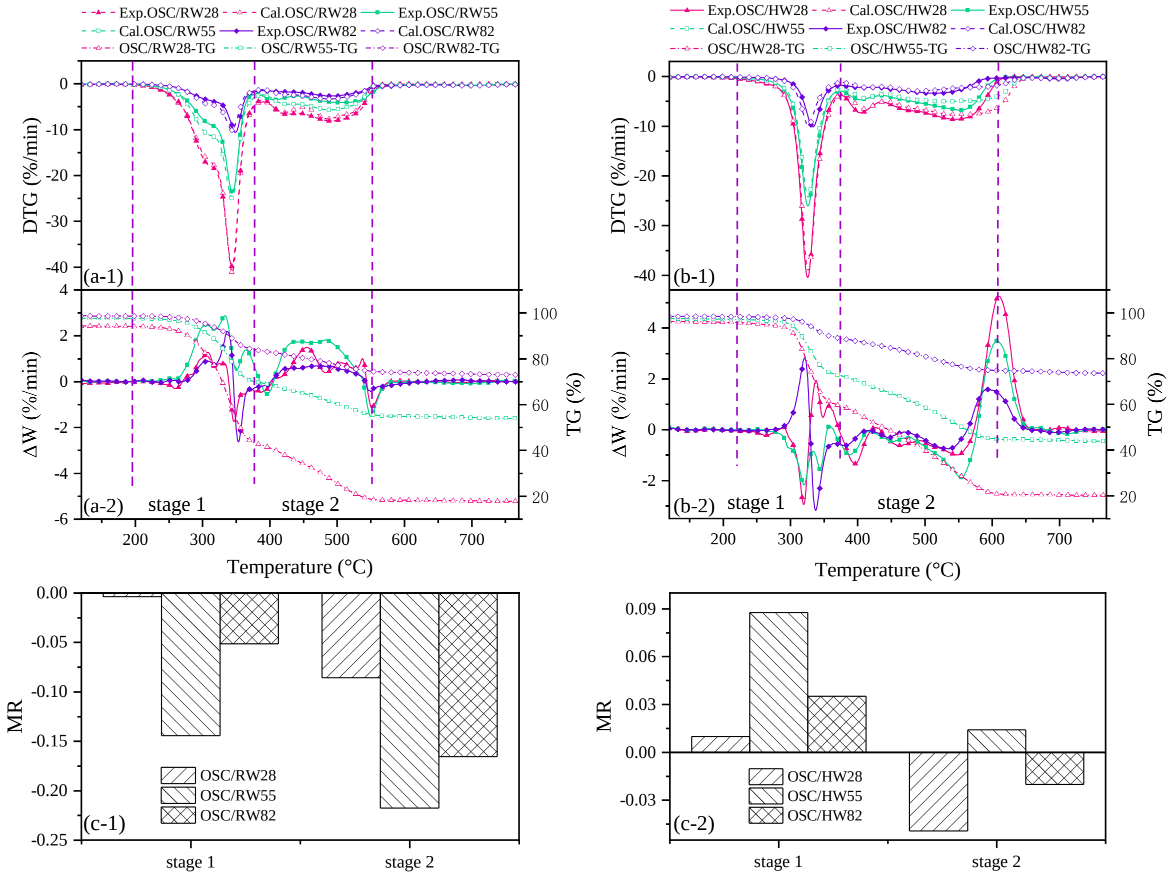

**Figure 4.5** The experimental and calculated DTG curves and their deviations of the blends under different blending ratios. (a-1) and (a-2) OSC/RW; (b-1) and (b-2) OSC/HW; (c-1) MR values of OSC/RW under different blending ratios; (c-2) MR values of OSC/HW under different blending ratios.

### 4.3.4.2 The interaction between OSC and HW

As shown in **Figure 4.5 (b-1)**, experimental curves of weight loss rate were mostly below the calculated curves. It means that experimental weight loss rate was larger than the predicted rate. Correspondingly, $\Delta W$ values were almost negative in stage 1 and stage 2, suggesting positive interaction for co-combustion (see **Figure 4.5 (b-2)**). Notably, **Figure 4.5 (b-2)** shows that the $\Delta W$ values were positive between 570 and 660 °C under different blending ratios, indicating a significant negative interaction. However, it should be noted that this largely negative interaction occurred at the end stage of co-combustion. The TG curve of OSC/HW blends, shown in **Figure 4.5 (b-2)**, also indicated that the combustion process was almost completed when the temperature increased above 600 °C. It was consistent with the lower burnout temperatures of OSC/HW than that of HW (see **Table 4.4** and **section 4.3.3**). Consequently, it could be summarized that the co-combustion interaction between OSC and HW was mainly positive.

The contrast interaction between OSC/RW and OSC/HW was attributed to the modified properties of samples and partial removal of alkali metals after HTT (see **Table 4.3**). On one hand, HW surface became rougher than RW after HTT, as displayed in **Figure 4.6**. It accelerated the pore formation via devolatilization process, which provided more gas diffusion channels to accelerate the decomposition rate, positively affecting the interactions between OSC and HW. Similar result was also obtained by Külaots et al. [4-31] They found that the removing of AAEMs could open more pores and thereby provide active sites to the gaseous products. On the other hand, the lower contents of alkali metals in HW should be a disadvantage to co-combustion owing to less catalytic support. Positive interaction between OSC and HW would be discussed further in **section 4.3.6** according to kinetic analysis results.

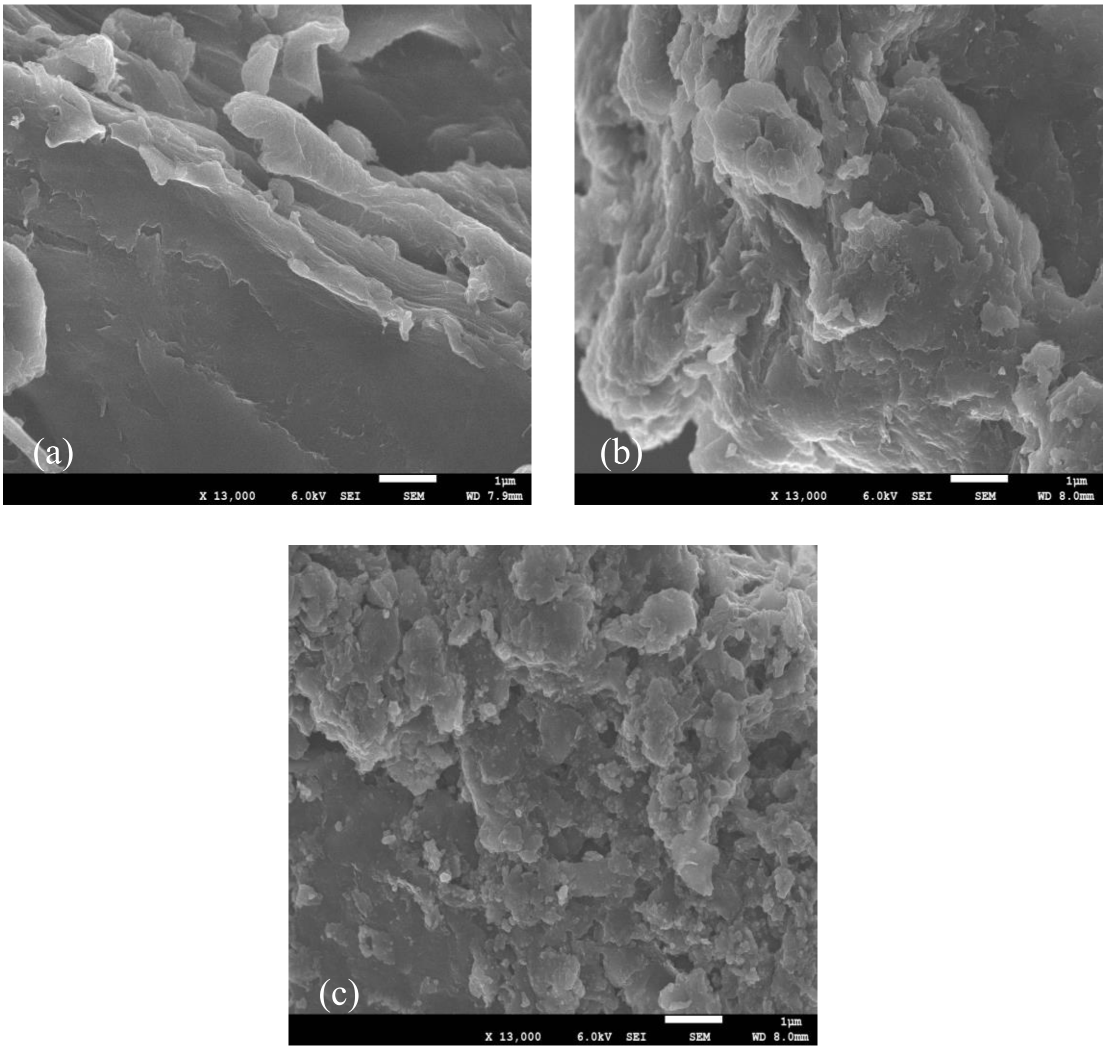

**Figure 4.6** SEM images of (a) RW, (b) HW, and (c) OSC.

### 4.3.5 Kinetic analysis

#### 4.3.5.1 Model-free methods

Apparent activation energy (*E*) at conversion ratio ($\alpha$) from 0.2 to 0.8 with an interval step of 0.05 in stage 1 and stage 2 was determined. It is noted that the conversion ratio is not the overall conversion degree but the local conversion degree in each stage. The Arrhenius plots were depicted for stage 1 and stage 2 by FWO and KAS method (see **Figures A.1 – A.4** and **Table A.3** in **Appendix**). **Table 4.6** listed the kinetic parameters based on conversion ratio for each sample. The *E* values as a function of α were shown in **Figure 4.7**. The results indicated that the variation of *E* calculated by the FWO method had good agreement with those of KAS methods, verifying the determined *E* were consistent.

**Table 4.6** Kinetic triplets (E, A, and model) for samples at 40 °C/min by master plot method.

| Sample | Stage 1 | | | | Stage 2 | | | |
|---|---|---|---|---|---|---|---|---|
| | $E_{ave}^{*}$ | A | Model | $R^2$ | $E_{ave}^{*}$ | A | Model | $R^2$ |
| OSC | 128.65 | 1.08E12 | F2 | 0.999 | 172.44 | 3.03E10 | R3 | 0.67 |
| RW | 211.33 | 1.80E20 | D4 | 0.998 | 169.28 | 4.12E13 | D3 | 0.999 |
| OSC/RW28 | 212.26 | 8.00E20 | D2 | 0.999 | 177.34 | 1.30E14 | D3 | 0.996 |
| OSC/RW55 | 207.90 | 3.43E20 | D2 | 0.997 | 163.61 | 8.86E12 | D3 | 0.996 |
| OSC/RW82 | 206.51 | 2.45E20 | D2 | 0.996 | 157.88 | 2.97E12 | D3 | 0.983 |
| HW | 208.40 | 2.47E21 | F1 | 0.983 | 126.18 | 8.09E9 | D3 | 0.998 |
| OSC/HW28 | 204.44 | 1.23E21 | F1 | 0.983 | 145.40 | 2.57E12 | D3 | 0.997 |
| OSC/HW55 | 186.96 | 3.26E19 | F1 | 0.981 | 151.16 | 6.01E11 | D3 | 0.998 |
| OSC/HW82 | 202.83 | 5.54E20 | F1 | 0.990 | 150.93 | 6.54E11 | D3 | 0.991 |

* avergae *E* values

As shown in **Figures 4.7 (a)** and **(b)**, the *E* value of OSC gradually decreased in stage 1 whereas the *E* value reached a peak at $\alpha = 0.5$ and increased again when $\alpha > 0.75$ in stage 2. The variation of *E* value was consistent with the thermal decomposition of OSC (see **section 4.3.2**). For RW, one peak of the *E* value was observed at $\alpha = 0.3$, and then the *E* value decreased until $\alpha = 0.75$ in stage 1. This stage could be attributed to the combustion of hemicellulose and cellulose. Hemicellulose was reported to have higher *E* value than cellulose during thermal degradation, thus leading to such a change in the *E* value [4-32, 4-33]. After HTT, less amount of hemicellulose was remained in HW comparing to RW. Therefore, the initial *E* value of HW was lower than that of RW and continuously increased with α. When $\alpha > 0.6$, the *E* value of HW was eventually larger than that of RW in stage 1, which was consistent with the composition profiles of their volatile and fixed carbon contents with increasing temperatures. The *E* values of RW and HW decreased with $\alpha$ in stage 2. In addition, HW had lower *E* than RW at any conversion ratio. This result agreed with previous studies [4-20, 4-27]. HTT degraded the highly cross-linked cell wall composed of cellulose, hemicellulose, and lignin, and thereby the *E* value was decreased. The results of apparent activation energies of RW and HW are close to previous related work, as listed in **Table A.4**. Moreover, it can be noted that the activation energies of biomass got a reduction after torrefaction due to the removal of hemicellulose, which agreed with the lower *E* value of HW in this work.

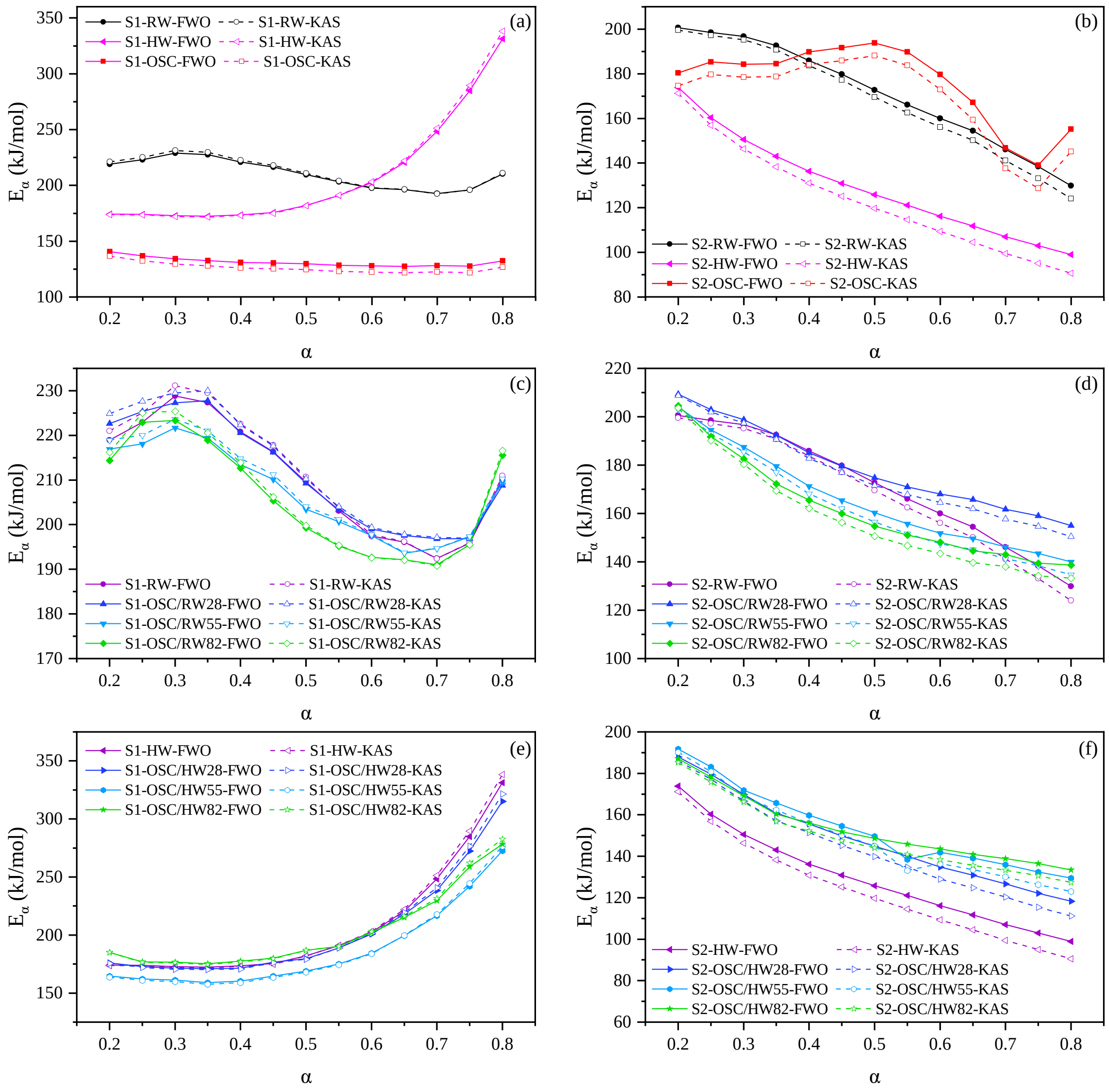

**Figure 4.7** The apparent activation energies (E) of OSC, RW, HW, and their respective blends (a) (b) variation of *E* for OSC, RW, and HW in stage 1 and stage 2; (c) (d) variation of *E* for OSC/RW in stage 1 and stage 2; (e) (f) variation of *E* for OSC/HW in stage 1 and stage 2. S1: Stage 1; S2: Stage 2.

As discussed in **section 4.3.2**, the combustion stages (stage 1 and stage 2) of RW and HW had different temperature ranges compared with OSC but similar with OSC/RW and OSC/HW. It means that combustion stages of the blend co-combustion were mainly dominated by RW or HW. Therefore, we just analyzed the effect of OSC addition on the *E* values of OSC/RW and OSC/HW. The *E* values of the blends in stage 1 and stage 2 displayed similar trends with RW or HW. On the other hand, **Figures 4.7 (c)** and **(e)** shows that the *E* values of OSC/RW and OSC/HW were lower than those of RW and HW in stage 1. Furthermore, the OSC addition significantly lowered the *E* values of OSC/HW, especially OSC/HW55. It agrees with the result in the previous section, in which OSC/HW55 displayed the strongest positive interaction in stage 1 (see **Figure 4.5 (c-2)**). **Figure 4.7 (d)** indicates that the $E$ values of OSC/RW in stage 2 became lower with increase of OSC proportion. However, the $E$ values of OSC/RW shifted higher than RW when $\alpha > 0.75$. **Figure 4.7 (f)** indicates that the $E$ values of OSC/HW gradually increased in stage 2 with OSC blending, implying that more energy input was required during co-combustion. It proposes that the OSC addition probably inhibited initializing the fixed carbon combustion of HW due to the accumulated ash layer when the combustion process continued. This result was not consistent with positive interactions to OSC/HW co-combustion (see **section 4.3.4.2**). A similar phenomenon was also observed during the co-combustion of dyeing sludge and rice husk by Wang et al. [4-34] They found that the $E$ values of the blends were higher than individual samples regardless of positive interactions. Despite the inconsistence, either in stage 1 or stage 2, the $E$ values of OSC/HW were significantly lower than OSC/RW under different OSC blending ratios.

### 4.3.5.2 Model-based methods

As shown in **Figure 4.8**, the average apparent activation energy, calculated from FWO and KAS methods, were used to establish experimental master plot curves of RW, HW, OSC, and their respective blends at 40 °C/min of heating rate. The curves of $G(\alpha)$ versus $EP(u)/\beta R$ were plotted, and **Table 4.6** listed the most feasible models of samples determined based on the linear least square. For RW, the $\alpha$-dependent trends of $P(u)/P(u_{0.5})$ had a good agreement with the D4 and D3 models in stage 1 and stage 2, respectively. It was consistent with previous studies [4-35]. D3 and D4 are diffusion-based models which assume that diffusive transfer of gaseous products controls overall reaction rate including numerous chemical reactions or micro-structure changes in particles [4-35]. For HW, the degradation curves in stage 1 and stage 2 were fitted to F1 and D3, respectively.

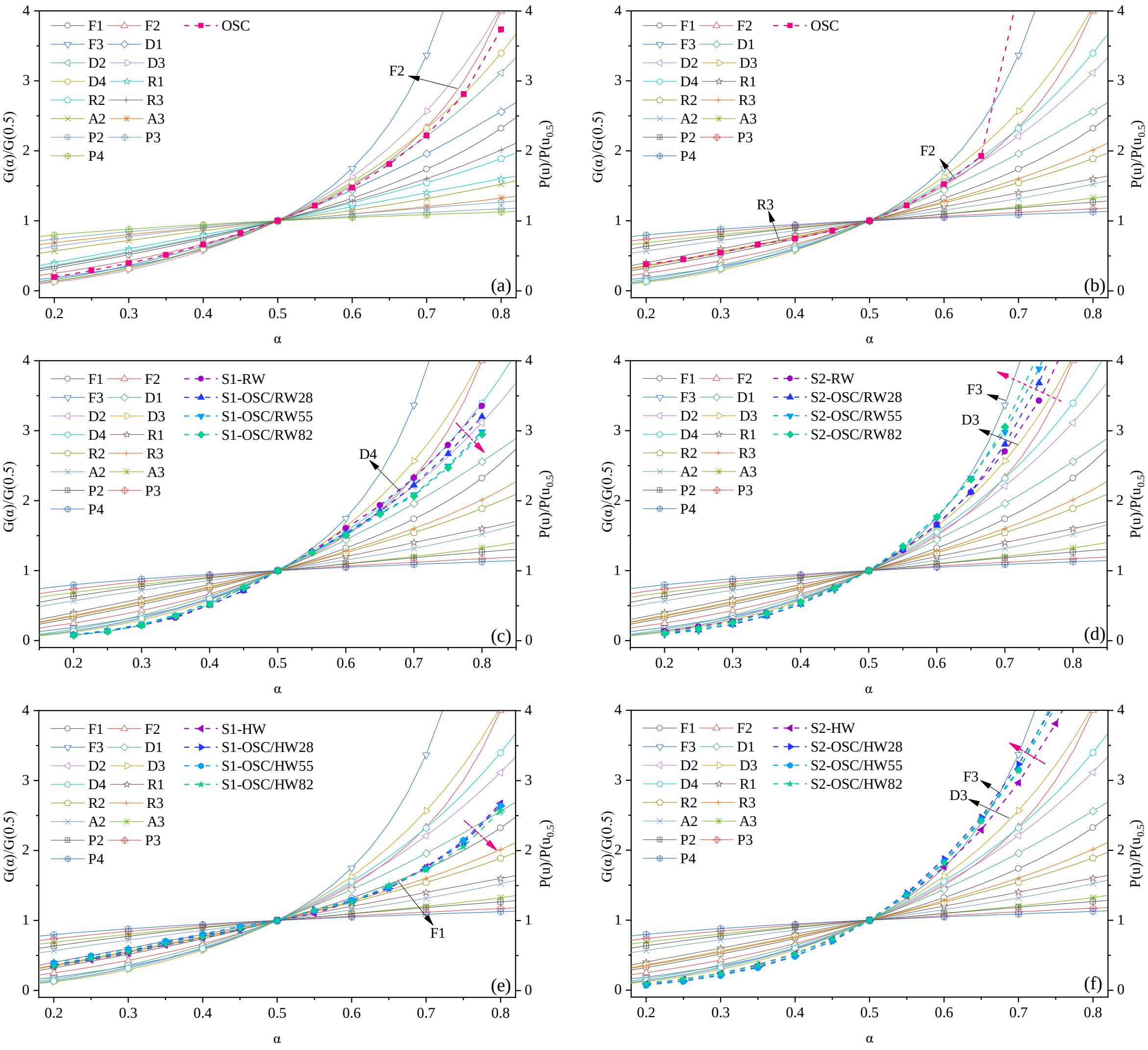

**Figure 4.8** $P(u)/P(u_{0.5})$ versus α in stage 1 at 40 ° C/min [(a) OSC, (c) RW and OSC/RW, (e) HW and OSC/HW]; $P(u)/P(u_{0.5})$ versus α in stage 2 at 40 ° C/min [(b) OSC, (d) RW and OSC/RW, (f) HW and OSC/HW]; and the direction of the pink dotted line arrow represented the variation of the curves with increasing OSC proportion in the blends.

In stage 1 of OSC, the heavy components wrapped on the OSC surface were thermally evaporated and oxidated into sticky oils or tars with increase of temperature [4-36]. Hence, the rate-determining reaction was chemical reaction (F2) (see **Figure 4.8 (a)**). However, **Figure 4.8 (b)** indicates that the reaction models of OSC varied with the increase of $\alpha$ in stage 2. As $\alpha$ ranging from 0.2 to 0.4, the degradation profile of OSC showed the best agreement with R3 theoretical plots, a three-dimensional phase boundary reaction, which was regarded as the governing model in the combustion of carbonaceous materials [4-37]. For OSC, heterogeneous reactions between fixed carbon and nascent ash layer took place, and the surface area of ash became the limiting factor [4-18, 4-38]. When $\alpha > 0.4$, the degradation curves of OSC sharply increased and could not locate into a specific reaction model.

As shown in **Figures 4.8 (c)** and **(e)**, the fittest models of OSC/RW (D2) and OSC/HW (F1) were similar with those of RW and HW in stage 1 under different OSC blending ratios. In stage 2, the degradation profiles of OSC/RW and OSC/HW still followed the D3 model, same as RW and HW (see **Figures 4.8 (d)** and **(f)**). Notably, the degradation profiles of both OSC/RW and OSC/HW located between D3 and F3 and gradually approached F3 with the increasing proportion of OSC. It is considered that OSC ash increased the surface area of the reactants and enlarged gas diffusion gaps. It might enhance gas diffusion during the fixed carbon combustion [4-18].

### 4.3.6 Possible mechanisms of OSC co-combustion with RW or HW

Previous research confirmed that the intrinsic solids in oil sludge had positive effects on the pyrolysis of oil sludge [4-18, 4-39], but the effect of solids on combustion and co-combustion with other feedstocks was still uncertain. The above sections revealed that the combustion of the blends contained complex reaction mechanisms. Therefore, in this section, these possible combustion mechanisms during the main (co-)combustion process (stage 1 and stage 2) were proposed based on the combustion characteristics, interactions, and kinetic analysis, with a schematic diagram depicting in **Figure 4.9**.

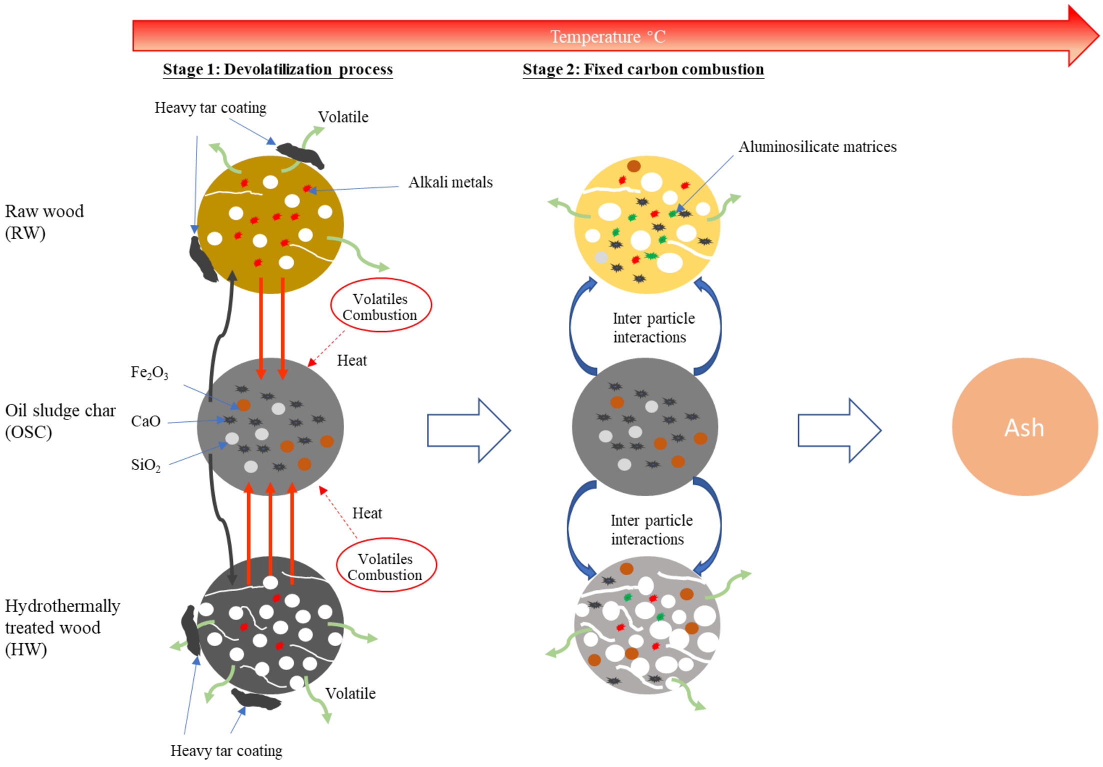

**Figure 4.9** (co-)combustion mechanism of OSC/RW and OSC/HW

The devolatilization process at low conversion stages of RW enhanced the formation of fixed carbon and heavy hydrocarbon layers. These layers conversely hindered the diffusion of gaseous products [4-37]. Besides, highly ordered cellulose regions in RW acted as barriers and obstructed heat transfer from the external source [4-40]. Therefore, the rate-limiting step in stage 1 was the diffusion-reaction (D4). After HTT, the inorganic substances were partially leached out, and many strongly bonded compounds were cracked and removed, giving HW improved homogeneity and well-developed pore structures. Heat transfer and gas diffusion inside HW particles became easier compared to RW, which enhanced gas diffusion. Thus, the rate-determination step was eventually shifted to F1 [4-18]. After blending with OSC, RW or HW ignited at first, and the released heat was consumed for OSC combustion. Meanwhile, the volatiles might be partially adsorbed by OSC due to its developed porosity (see **Figure 4.6**) and surface functional groups, leading to the reduction of the $E$ values [4-41]. These interactions should positively promote the decomposition rate of the blends. However, heavy components on the surface of OSC were thermally stimulated and accelerated the generation of sticky oils, which were inclined to coat the reactants (RW in this case) and conversely inhibited the diffusion [4-37]. As a result, a negative interaction appeared between OSC and RW. On the other hand, the positive interaction between OSC and HW could be due to faster gas diffusion in HW according to the kinetic models (Diffusion rate: F1 > D4). The volatiles from HW easily passed through owing to larger porosity of HW even when HW was coated by heavy components. Therefore, the positive interaction eventually remained.

In stage 2, the reaction model of RW was shifted from D2 in stage 1 to D3, representing a higher diffusion rate. This could be attributed to enhanced pore structure during devolatilization process, which provided channels for heat and gas transfer. However, with the removal of weakly bonded components, strongly bonded compounds in RW were recombined into hard solid polymers, impeding the diffusion reaction. Therefore, the dominant reaction model for HW became D3 in stage 2, signifying a lower diffusion rate than F1 in stage 1. For the blend co-combustion in stage 2, most of organic compounds in OSC were already evaporated and decomposed, eventually leaving a large amount of ash. The accumulated ash particles contained inert materials and could block the pore structure, which increased the thermal resistance of reactants. Hence, it made the $E$ values of OSC/HW increase apparently with increase of OSC blending ratio. Besides, some metal oxides such as $Fe_2O_3$ and CaO in OSC ash were reported to pose catalytic effect during combustion [4-2]. Cyclic deoxidation/oxidation reactions of these metal oxides assisted oxygen transfer to carbon surface of HW and accelerated the diffusion rate [4-42]. It promoted the decomposition and burnout of fixed carbon, which was consistent with decreased burnout temperature of OSC/HW. The catalytic support from metal oxides contained in OSC contributed into the positive interaction in OSC/HW co-combustion. For OSC/RW, low-melting-point substances, formed from reactions between alkali metals in RW and ash in OSC, were more susceptible to thermal decomposition than the inert ash particles, even though they aggravated the restriction on the decomposition rate. Therefore, OSC/RW exhibited decreasing $E$ values with an increase of OSC addition, whereas with negative interactions due to inhibited diffusion.

## 4.3 Conclusion

This chapter conducted co-combustion of OSC and RW/HW.

(1) RW or HW addition significantly improved combustion property and efficiency of OSC regarding the conventional combustion parameters.

(2) The RW blending caused negative interactions in co-combustion with OSC, although it decreased apparent activation energy. It mainly resulted from inhibited diffusion of volatile matters.

(3) HW addition yielded positive interactions owing to the developed porosity of HW, which effectively promotes volatiles diffusion, coupled with catalytic support by metal oxides in OSC.

(4) Not only the catalytic effect of inorganic elements on co-combustion but also their physical influence on heat and volatiles transfers can contribute to improving co-combustion performance.

## References

[4-1] Cheng, S., Wang, Y., Fumitake, T., Kouji, T., Li, A., & Kunio, Y. (2017). Effect of steam and oil sludge ash additive on the products of oil sludge pyrolysis. Applied Energy, 185, 146-157.

[4-2] Gong, Z., Wang, Z., Wang, Z., Fang, P., & Meng, F. (2019). Study on the migration characteristics of nitrogen and sulfur during co-combustion of oil sludge char and microalgae residue. Fuel, 238, 1-9.

[4-3] Wang, Z., Gong, Z., Wang, W., & Zhang, Z. (2020). Study on combustion characteristics and the migration of heavy metals during the co-combustion of oil sludge char and microalgae residue. Renewable Energy, 151, 648-658.

[4-4] Tong, W., Liu, Q., Ran, G., Liu, L., Ren, S., Chen, L., & Jiang, L. (2019). Experiment and expectation: Co-combustion behavior of anthracite and biomass char. Bioresource technology, 280, 412-420.

[4-5] Marzbali, M. H., Kundu, S., Halder, P., Patel, S., Hakeem, I. G., Paz-Ferreiro, J., ... & Shah, K. (2021). Wet organic waste treatment via hydrothermal processing: A critical review. Chemosphere, 279, 130557.

[4-6] Govindan, B., Chandra Babu Jakka, S., Radhakrishnan, T. K., Tiwari, A. K., Sudhakar, T. M., Shanmugavelu, P., ... & Sarkar, S. (2018). Investigation on kinetic parameters of combustion and oxy-combustion of calcined pet coke employing thermogravimetric analysis coupled to artificial neural network modeling. Energy & Fuels, 32(3), 3995-4007.

[4-7] Sezer, S., Kartal, F., & Özveren, U. (2021). The investigation of co-combustion process for synergistic effects using thermogravimetric and kinetic analysis with combustion index. Thermal Science and Engineering Progress, 23, 100889.

[4-8] Magdziarz, A., & Werle, S. (2014). Analysis of the combustion and pyrolysis of dried sewage sludge by TGA and MS. Waste management, 34(1), 174-179.

[4-9] Cheng, S., Wang, Y., Gao, N., Takahashi, F., Li, A., & Yoshikawa, K. (2016). Pyrolysis of oil sludge with oil sludge ash additive employing a stirred tank reactor. Journal of Analytical and Applied Pyrolysis, 120, 511-520.

[4-10] Cordero, T., Marquez, F., Rodriguez-Mirasol, J., & Rodriguez, J. J. (2001). Predicting heating values of lignocellulosics and carbonaceous materials from proximate analysis. Fuel, 80(11), 1567-1571.

[4-11] Khoshbouy, R., Takahashi, F., & Yoshikawa, K. (2019). Preparation of high surface area sludge-based activated hydrochar via hydrothermal carbonization and application in the removal of basic dye. Environmental research, 175, 457-467.

[4-12] Zhao, P., Shen, Y., Ge, S., & Yoshikawa, K. (2014). Energy recycling from sewage sludge by producing solid biofuel with hydrothermal carbonization. Energy conversion and management, 78, 815-821.

[4-13] He, C., Zhang, Z., Ge, C., Liu, W., Tang, Y., Zhuang, X., & Qiu, R. (2019). Synergistic effect of hydrothermal co-carbonization of sewage sludge with fruit and

agricultural wastes on hydrochar fuel quality and combustion behavior. Waste Management, 100, 171-181.

[4-14] Li, X. G., Ma, B. G., Xu, L., Hu, Z. W., & Wang, X. G. (2006). Thermogravimetric analysis of the co-combustion of the blends with high ash coal and waste tyres. Thermochimica Acta, 441(1), 79-83.

[4-15] Seggiani, M., Vitolo, S., Pastorelli, M., & Ghetti, P. (2007). Combustion reactivity of different oil-fired fly ashes as received and leached. Fuel, 86(12-13), 1885-1891.

[4-16] Hurt, R. H., & Gibbins, J. R. (1995). Residual carbon from pulverized coal fired boilers: 1. Size distribution and combustion reactivity. Fuel, 74(4), 471-480.

[4-17] Vyazovkin, S., Burnham, A. K., Criado, J. M., Pérez-Maqueda, L. A., Popescu, C., & Sbirrazzuoli, N. (2011). ICTAC Kinetics Committee recommendations for performing kinetic computations on thermal analysis data. Thermochimica acta, 520(1-2), 1-19.

[4-18] Qu, Y., Li, A., Wang, D., Zhang, L., & Ji, G. (2019). Kinetic study of the effect of in-situ mineral solids on pyrolysis process of oil sludge. Chemical Engineering Journal, 374, 338-346.

[4-19] Tang, W., Liu, Y., Zhang, H., & Wang, C. (2003). New approximate formula for Arrhenius temperature integral. Thermochimica Acta, 408(1-2), 39-43.

[4-20] Yan, W., Perez, S., & Sheng, K. (2017). Upgrading fuel quality of moso bamboo via low temperature thermochemical treatments: Dry torrefaction and hydrothermal carbonization. Fuel, 196, 473-480.

[4-21] Ma, P., Yang, J., Xing, X., Weihrich, S., Fan, F., & Zhang, X. (2017). Isoconversional kinetics and characteristics of combustion on hydrothermally treated biomass. Renewable Energy, 114, 1069-1076.

[4-22] Munir, S., Daood, S. S., Nimmo, W., Cunliffe, A. M., & Gibbs, B. M. (2009).

Thermal analysis and devolatilization kinetics of cotton stalk, sugar cane bagasse and shea meal under nitrogen and air atmospheres. Bioresource technology, 100(3), 1413-1418.

[4-23] Cheng, S., Zhang, H., Chang, F., Zhang, F., Wang, K., Qin, Y., & Huang, T. (2019). Combustion behavior and thermochemical treatment scheme analysis of oil sludges and oil sludge semicokes. Energy, 167, 575-587.

[4-24] Deng, S., Wang, X., Tan, H., Mikulčić, H., Yang, F., Li, Z., & Duić, N. (2016). Thermogravimetric study on the Co-combustion characteristics of oily sludge with plant biomass. Thermochimica acta, 633, 69-76.

[4-25] Mlonka-Mędrala, A., Magdziarz, A., Gajek, M., Nowińska, K., & Nowak, W. (2020). Alkali metals association in biomass and their impact on ash melting behaviour. Fuel, 261, 116421.

[4-26] Lee, S. H., Lee, T. H., Jeong, S. M., & Lee, J. M. (2019). Economic analysis of a 600 mwe ultra supercritical circulating fluidized bed power plant based on coal tax and biomass co-combustion plans. Renewable Energy, 138, 121-127.

[4-27] Zhang, Y., Zhang, Z., Zhu, M., Cheng, F., & Zhang, D. (2016). Interactions of coal gangue and pine sawdust during combustion of their blends studied using differential thermogravimetric analysis. Bioresource technology, 214, 396-403.

[4-28] Tong, W., Liu, Q., Ran, G., Liu, L., Ren, S., Chen, L., & Jiang, L. (2019). Experiment and expectation: Co-combustion behavior of anthracite and biomass char. Bioresource technology, 280, 412-420.

[4-29] Ma, Q., Han, L., & Huang, G. (2017). Potential of water-washing of rape straw on thermal properties and interactions during co-combustion with bituminous coal. Bioresource technology, 234, 53-60.

[4-30] Yao, Z., Ma, X., Wang, Z., & Chen, L. (2017). Characteristics of co-combustion and kinetic study on hydrochar with oil shale: a thermogravimetric analysis. Applied Thermal Engineering, 110, 1420-1427.

[4-31] Külaots, I., Link, S., Arvelakis, S., & Suuberg, E. M. (2010). Adsorption properties of wheat straw, reed and Douglas fir chars. In International Carbon 2010 conference.

[4-32] Bach, Q. V., Tran, K. Q., Skreiberg, Ø., Khalil, R. A., & Phan, A. N. (2014). Effects of wet torrefaction on reactivity and kinetics of wood under air combustion conditions. Fuel, 137, 375-383.

[4-33] Barzegar, R., Yozgatligil, A., Olgun, H., & Atimtay, A. T. (2020). TGA and kinetic study of different torrefaction conditions of wood biomass under air and oxy-fuel combustion atmospheres. Journal of the Energy Institute, 93(3), 889-898.

[4-34] Wang, T., Fu, T., Chen, K., Cheng, R., Chen, S., Liu, J., ... & Xue, Y. (2020). Co-combustion behavior of dyeing sludge and rice husk by using TG-MS: Thermal conversion, gas evolution, and kinetic analyses. Bioresource Technology, 311, 123527.

[4-35] Gil, M. V., Casal, D., Pevida, C., Pis, J. J., & Rubiera, F. (2010). Thermal behaviour and kinetics of coal/biomass blends during co-combustion. Bioresource technology, 101(14), 5601-5608.

[4-36] Liu, C., Liu, J., Sun, G., Xie, W., Kuo, J., Li, S., ... & Evrendilek, F. (2018). Thermogravimetric analysis of (co-) combustion of oily sludge and litchi peels: combustion characterization, interactions and kinetics. Thermochimica acta, 667, 207-218.

[4-37] Yorulmaz, S. Y., & Atimtay, A. T. (2009). Investigation of combustion kinetics of treated and untreated waste wood samples with thermogravimetric analysis. Fuel Processing Technology, 90(7-8), 939-946.

[4-38] Singh, S., Chakraborty, J. P., & Mondal, M. K. (2020). Intrinsic kinetics, thermodynamic parameters and reaction mechanism of non-isothermal degradation of torrefied Acacia nilotica using isoconversional methods. Fuel, 259, 116263.

[4-39] Cheng, S., Wang, Y., Gao, N., Takahashi, F., Li, A., & Yoshikawa, K. (2016).

Pyrolysis of oil sludge with oil sludge ash additive employing a stirred tank reactor. Journal of Analytical and Applied Pyrolysis, 120, 511-520.

[4-40] Poletto, M., Zattera, A. J., & Santana, R. M. (2012). Thermal decomposition of wood: kinetics and degradation mechanisms. Bioresource Technology, 126, 7-12.

[4-41] Gong, Z., Meng, F., Wang, Z., Fang, P., Li, X., Liu, L., & Zhang, H. (2019). Study on preparation of an oil sludge-based carbon material and its adsorption of CO2: effect of the blending ratio of oil sludge pyrolysis char to KOH and urea. Energy & Fuels, 33(10), 10056-10065.

[4-42] Li, X. G., Ma, B. G., Xu, L., Luo, Z. T., & Wang, K. (2007). Catalytic effect of metallic oxides on combustion behavior of high ash coal. Energy & fuels, 21(5), 2669-2672.

# Chapter 5 Conclusions and recommendations

## 5.1 Overall conclusion

Integrated pyrolysis and combustion treatment can efficiently recover resources in oil sludge and remove the hazards of oil sludge. However, for ash-rich oil sludge, especially oilfield sludge, this integrated treatment is still limited by some shortcomings, such as low pyrolysis efficiency and low energy recovery efficiency. Aiming at this problem, this study introduces biomass into this treatment system, investigating the interactions and kinetics of co-pyrolysis/co-combustion of oil sludge/oil sludge char and biomass, and deducing the reaction mechanism.

**Chapter 1** introduced the background of this research, including the classification, characterization, and hazards of oil sludge, the overview of treatment methods of oil sludge, the integrated pyrolysis and combustion of oil sludge, and two typical biomass pretreatment methods to give a comprehensive understanding about the research objective and significance of this work.

To obtain hydrocarbon-rich pyrolysis oil, torrefaction is an effective method to pretreat biomass. In **Chapter 2**, the effect of torrefaction on the morphological structure evolution and pyrolysis reactivity of biomass was investigated. The results indicated: (1) Intensified torrefaction led to enhanced surface aromaticity, rougher surface structure, and decreased crystallinity of rice straw. (2) The pyrolysis reactivity of rice straw was weakened after torrefaction, and the decomposition temperature ranges of TS were shifted to higher temperatures with increasing torrefaction temperature. (3) Torrefaction altered the pyrolysis pathway of torrefied rice straw to enhance char production at the expense of oil and gas. (4) Torrefaction pretreatment enhanced hydrocarbon production, especially alkanes and aromatics.

The results in **Chapter 2** indicated that torrefaction of rice straw enhanced hydrocarbon production in pyrolysis oil and enriched lignin content in torrefied rice straw. Therefore, in **Chapter 3**, co-pyrolysis of oil sludge and raw/torrefied biomass to enhance hydrocarbon production and evaluate the co-pyrolysis synergistic behavior among oil sludge and model biomass components were conducted. According to the results: (1) Co-pyrolysis of OS and RS promoted char conversion to volatiles, especially gas products. (2) The incorporation of OS into either RS or TS promoted hydrocarbon production at the expense of oxygenates. A significant synergistic effect was witnessed in enhancing hydrocarbon production after OS addition. (3) RS/OS mass ratio of 1:1 was a critical point considering the degree of promoting the formation of hydrocarbons. A higher blending ratio of OS hindered mass and heat transfer, thereby suppressing the gas formation and lowering the synergy for hydrocarbon generation. (4) Severe torrefaction increased TS's main decomposition temperature range close to that of OS, and positive synergistic effects for oil generation were observed when OS was blended into TS obtained at 250 and 300 °C. (5) A notable result in this work is that OS addition supplied ample hydrogen atoms and Ni/$SiO_2$ minerals, which further promoted the hydrogenation and ring-opening of aromatic structures, enhancing alkane and olefin formation at the consumption of aromatics.

**Chapter 2** and **Chapter 3** focused on incorporating biomass into co-pyrolysis with oil sludge. Additionally, adding biomass to combustion with oil sludge char is also an effective method to enhance energy recovery. In **Chapter 4**, co-combustion of oil sludge char and raw/hydrothermally treated biomass is performed to promote combustion efficiency and evaluate the effect of alkali metals on co-combustion interactions, kinetics, and mechanisms. The results showed: (1) RW or HW addition significantly improved combustion property and efficiency of OSC regarding the conventional combustion parameters. (2) The RW blending caused negative interactions in co-combustion with OSC, although it decreased apparent activation energy. It mainly resulted from inhibited diffusion of volatile matters. (3) On the contrary, HW blending yielded positive interactions owing to the developed porosity of HW, which effectively promotes volatiles diffusion, coupled with catalytic support by metal oxides in OSC. (4) Not only the catalytic effect of inorganic elements on co-combustion but also their physical influence on heat and volatiles transfers can contribute to improving co-combustion performance.

## 5.2 Recommendations

(1) This study employed torrefied rice straw to enhance hydrocarbon production and investigated the interactions between oil sludge and model biomass components since intensified torrefaction gradually increased the content of lignin in rice straw. It is recommended to perform co-pyrolysis of oil sludge with typical model biomass components (hemicellulose, cellulose, and lignin) to observe a concrete interaction and mechanism.

(2) This study proposed that the radical reactions between samples led to the synergistic effect which promoted hydrocarbon production. Future work should evaluate the generation and migration of radicals, thereby illustrating the concrete synergistic pathway.

(3) This study investigated the synergistic behavior during co-pyrolysis of rice straw/torrefied rice straw. Furthermore, a deconvoluted understanding of synergistic effects should be conducted. For example, the contributions of volatile interactions, volatile-char interactions, and biomass-oil sludge ash (to the synergy) could be detailed by different experimental configurations such as non-contact pyrolysis of samples.

(4) Biomass addition increased the pyrolysis oil yields compared to oil sludge alone. Future work can add catalysts to further improve oil quality, such as increasing the concentration of light-weight compounds in the oil.

## 5.3 Practical applications

The practical application of this work is illustrated in **Figure 5.1**. In the same pyrolysis reactor, torrefaction (200 – 300 °C) of biomass is conducted at first to modify raw biomass. Then the temperature of the reactor is increased around 600 °C and oil sludge is added to co-pyrolysis with torrefied biomass. The steam generated from torrefaction can be used for pyrolysis, since pyrolysis with steam addition is an efficient method to increase the conversion of solid fuels and biomass into liquid products. Therefore, the energy input of the integrated pyrolysis and combustion system can be fully utilized, and the quality of co-pyrolysis oil can be promoted, with higher concentration of hydrocarbons and lower concentration of oxygenates.

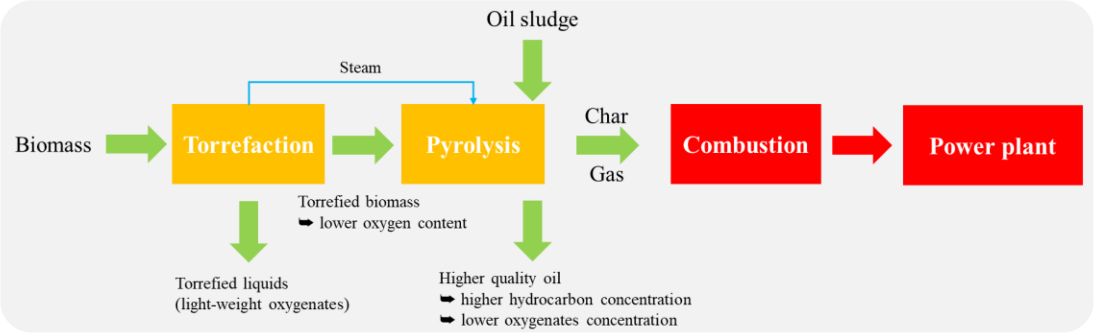

**Figure 5.1** Practical application of this work.

# Appendix

**Table A.1** Relative concentrations of straight-chain alkanes and aromatics in oil from individual pyrolysis of samples.

| | RS | TS200 | TS250 | TS300 | OS |
|---|---|---|---|---|---|
| ***Straight-chain alkanes (C10-C24)*** | | | | | |
| C10 | 0 | 0 | 0 | 0 | 0 |
| C11 | 0 | 0 | 0 | 0 | 0.54 |
| C12 | 0.54 | 0 | 1.49 | 1.07 | 0.76 |
| C13 | 0.63 | 1.02 | 1.52 | 0.46 | 1.61 |
| C14 | 0 | 0 | 0 | 0 | 1.77 |
| C15 | 0.33 | 0.26 | 0.64 | 2.05 | 2.36 |
| C16 | 0.62 | 0.73 | 2.93 | 5.45 | 2.86 |
| C17 | 0 | 0 | 0 | 0 | 3.52 |
| C18 | 0.23 | 0.29 | 0.5 | 1.43 | 4.42 |
| C19 | 0 | 0 | 0 | 0 | 3.15 |
| C20 | 0.26 | 0.48 | 3.03 | 2.77 | 2.34 |
| C21 | 0.41 | 0.12 | 0.87 | 0 | 2.64 |
| C22 | 0.38 | 0 | 0 | 0 | 2.58 |
| C23 | 0 | 0 | 0 | 0 | 2.2 |
| C24 | 2.98 | 3.64 | 4.68 | 23.61 | 4.37 |
| **Sum** | 6.38 | 6.54 | 15.66 | 36.84 | 35.12 |
| ***Straight-chain alkanes (C25-C27)*** | | | | | |
| C25 | 0 | 0 | 0 | 0 | 0 |
| C26 | 0 | 0 | 0 | 0 | 0.87 |
| C27 | 0 | 0 | 0 | 0 | 0 |
| **Sum** | 0 | 0 | 0 | 0 | 0.87 |
| ***Aromatics*** | | | | | |
| Monocyclic | 0.59 | 0.71 | 0.92 | 0.74 | 0.52 |
| Bicyclic | 6.73 | 10.26 | 17.1 | 22.23 | 0.2 |
| Tricyclic | 0 | 0 | 1.59 | 0 | 0.8 |
| Tetracyclic | 0 | 0 | 1.25 | 0 | 0 |
| **Sum** | 7.32 | 10.97 | 20.86 | 22.97 | 1.52 |

**Table A.2** Relative concentrations of straight-chain alkanes, oxygenates, and aromatics in oil from co-pyrolysis of samples.

| | RS:OS=3:1 | | | RS:OS=1:1 | | | RS:OS=1:3 | | | TS200:OS=3:1 | | | TS250:OS=3:1 | | | TS300:OS=3:1 | | |
|---|---|---|---|---|---|---|---|---|---|---|---|---|---|---|---|---|---|---|
| | Exp. | Cal. | Exp.-Cal. | Exp. | Cal. | Exp.-Cal. | Exp. | Cal. | Exp.-Cal. | Exp. | Cal. | Exp.-Cal. | Exp. | Cal. | Exp.-Cal. | Exp. | Cal. | Exp.-Cal. |
| ***Straight chain alkanes (C10-C24)*** | | | | | | | | | | | | | | | | | | |
| C10 | 0 | 0 | 0 | 0 | 0 | 0 | 0 | 0 | 0 | 0.09 | 0 | 0.09 | 0 | 0 | 0 | 0 | 0 | 0 |
| C11 | 0 | 0.14 | -0.14 | 0.3 | 0.27 | 0.03 | 0.45 | 0.41 | 0.04 | 0 | 0.14 | -0.14 | 0 | 0.14 | -0.14 | 0 | 0.14 | -0.14 |
| C12 | 0.44 | 0.6 | -0.16 | 0.45 | 0.65 | -0.2 | 0.62 | 0.71 | -0.09 | 0.47 | 0.19 | 0.28 | 0.57 | 1.31 | -0.74 | 0 | 0.99 | -0.99 |
| C13 | 0.29 | 0.88 | -0.59 | 0.97 | 1.12 | -0.15 | 1.49 | 1.37 | 0.12 | 0.38 | 1.17 | -0.79 | 0.49 | 1.54 | -1.05 | 0.53 | 0.75 | -0.22 |
| C14 | 0.34 | 0.44 | -0.1 | 0.7 | 0.89 | -0.19 | 0.98 | 1.33 | -0.35 | 0.93 | 0.44 | 0.49 | 0.69 | 0.44 | 0.25 | 0.71 | 0.44 | 0.27 |
| C15 | 0.71 | 0.84 | -0.13 | 1.09 | 1.35 | -0.26 | 1.21 | 1.85 | -0.64 | 0.73 | 0.79 | -0.06 | 1 | 1.07 | -0.07 | 1.07 | 2.13 | -1.06 |
| C16 | 0.68 | 1.18 | -0.5 | 0.94 | 1.74 | -0.8 | 1.69 | 2.3 | -0.61 | 0.62 | 1.26 | -0.64 | 0.88 | 2.91 | -2.03 | 1.06 | 4.8 | -3.74 |
| C17 | 2.05 | 0.88 | 1.17 | 1.85 | 1.76 | 0.09 | 2.26 | 2.64 | -0.38 | 1.55 | 0.88 | 0.67 | 1.04 | 0.88 | 0.16 | 2.51 | 0.88 | 1.63 |
| C18 | 0.69 | 1.28 | -0.59 | 1.3 | 2.33 | -1.03 | 2.23 | 3.37 | -1.14 | 1.16 | 1.32 | -0.16 | 1.56 | 1.48 | 0.08 | 1.12 | 2.18 | -1.06 |
| C19 | 0.68 | 0.79 | -0.11 | 1.41 | 1.58 | -0.17 | 1.95 | 2.36 | -0.41 | 0.68 | 0.79 | -0.11 | 0.89 | 0.79 | 0.1 | 1.08 | 0.79 | 0.29 |
| C20 | 1.54 | 0.78 | 0.76 | 2.35 | 1.3 | 1.05 | 3.91 | 1.82 | 2.09 | 0.72 | 0.95 | -0.23 | 1.09 | 2.86 | -1.77 | 1.09 | 2.66 | -1.57 |
| C21 | 0.71 | 0.97 | -0.26 | 1.64 | 1.53 | 0.11 | 1.42 | 2.08 | -0.66 | 0.92 | 0.75 | 0.17 | 1.05 | 1.31 | -0.26 | 1.37 | 0.66 | 0.71 |
| C22 | 0.79 | 0.93 | -0.14 | 1.19 | 1.48 | -0.29 | 2.22 | 2.03 | 0.19 | 0.82 | 0.65 | 0.17 | 1.18 | 0.65 | 0.53 | 1.61 | 0.65 | 0.96 |
| C23 | 1.58 | 0.55 | 1.03 | 1.73 | 1.1 | 0.63 | 1.46 | 1.65 | -0.19 | 0.9 | 0.55 | 0.35 | 1.88 | 0.55 | 1.33 | 2.5 | 0.55 | 1.95 |
| C24 | 2.18 | 3.33 | -1.15 | 2.84 | 3.68 | -0.84 | 4.16 | 4.02 | 0.14 | 1.18 | 3.82 | -2.64 | 5.66 | 4.6 | 1.06 | 6.2 | 18.8 | -12.6 |
| **Sum** | 12.68 | 13.57 | -0.89 | 18.76 | 20.75 | -1.99 | 26.05 | 27.94 | -1.89 | 11.15 | 13.69 | -2.54 | 17.98 | 20.53 | -2.55 | 20.85 | 36.41 | -15.56 |
| ***Straight chain alkanes (C15-C27)*** | | | | | | | | | | | | | | | | | | |
| C25 | 0 | 0 | 0 | 0.84 | 0 | 0.84 | 1.21 | 0 | 1.21 | 0.43 | 0 | 0.43 | 0.75 | 0 | 0.75 | 1.25 | 0 | 1.25 |
| C26 | 1.05 | 0.22 | 0.83 | 1.12 | 0.44 | 0.68 | 1.32 | 0.65 | 0.67 | 0.99 | 0.22 | 0.77 | 1.49 | 0.22 | 1.27 | 1.94 | 0.22 | 1.72 |
| C27 | 2.79 | 0 | 2.79 | 3.18 | 0 | 3.18 | 0 | 0 | 0 | 3.52 | 0 | 3.52 | 4.83 | 0 | 4.83 | 3.31 | 0 | 3.31 |

| | | | | | | | | | | | | | | | | | | |
|---|---|---|---|---|---|---|---|---|---|---|---|---|---|---|---|---|---|---|
| **Sum** | 3.84 | 0.22 | 3.62 | 5.14 | 0.44 | 4.7 | 2.53 | 0.65 | 1.88 | 4.94 | 0.22 | 4.72 | 7.07 | 0.22 | 6.85 | 6.5 | 0.22 | 6.28 |
| ***Oxygenates*** | | | | | | | | | | | | | | | | | | |
| Acid | 3.14 | 11.20 | -8.06 | 1.15 | 7.67 | -6.52 | 0.88 | 4.15 | -3.27 | 4.30 | 10.20 | -5.90 | 3.23 | 6.03 | -2.80 | 2.14 | 0.74 | 1.40 |
| Alcohol | 11.42 | 6.58 | 4.84 | 9.88 | 8.36 | 1.52 | 10.16 | 10.14 | 0.02 | 7.40 | 6.30 | 1.11 | 20.56 | 5.72 | 14.84 | 15.78 | 4.22 | 11.56 |
| Aldehyde | 7.42 | 9.84 | -2.42 | 0.52 | 6.68 | -6.16 | 0.48 | 3.53 | -3.05 | 7.38 | 7.85 | -0.47 | 0 | 2.73 | -2.73 | 0 | 0.09 | -0.09 |
| Anhydrosugars | 0.75 | 1.52 | -0.77 | 0 | 1.01 | -1.01 | 0 | 0.51 | -0.51 | 0.60 | 1.35 | -0.75 | 0 | 0.95 | -0.95 | 0 | 0 | 0 |
| Ester | 3.12 | 4.36 | -1.24 | 1.87 | 3.19 | -1.32 | 1.98 | 2.03 | -0.04 | 2.04 | 3.38 | -1.34 | 0 | 0.22 | -0.22 | 1.77 | 0.64 | 1.13 |
| Furan | 0 | 8.99 | -8.99 | 0 | 6.00 | -6.00 | 0 | 3.00 | -3.00 | 0.83 | 8.16 | -7.33 | 0 | 3.58 | -3.58 | 0 | 0 | 0 |
| Ketone | 10.81 | 11.60 | -0.78 | 4.05 | 7.84 | -3.79 | 2.23 | 4.09 | -1.86 | 7.43 | 10.77 | -3.34 | 3.1 | 7.62 | -4.52 | 2.65 | 0.54 | 2.11 |
| Phenol | 9.33 | 7.65 | 1.68 | 2.37 | 5.10 | -2.73 | 1.98 | 2.55 | -0.57 | 10.94 | 11.06 | -0.12 | 9.02 | 13.65 | -4.63 | 1.23 | 15.34 | -14.11 |
| **Sum** | 45.99 | 61.72 | -15.73 | 19.84 | 45.85 | -26.01 | 17.71 | 29.97 | -12.26 | 40.92 | 59.06 | -18.14 | 35.91 | 40.49 | -4.58 | 23.57 | 21.57 | 2.00 |
| ***Aromatics*** | | | | | | | | | | | | | | | | | | |
| Monocyclic | 0 | 0.57 | -0.57 | 0.64 | 0.56 | 0.08 | 0.53 | 0.54 | -0.01 | 0.06 | 0.66 | -0.6 | 0.94 | 0.82 | 0.12 | 0 | 0.69 | -0.69 |
| Bicyclic | 5.05 | 5.1 | -0.05 | 2.18 | 3.47 | -1.29 | 1.73 | 1.83 | -0.1 | 7.7 | 7.75 | -0.05 | 8.48 | 12.88 | -4.4 | 6.07 | 16.72 | -10.65 |
| Tricyclic | 0 | 0.2 | -0.2 | 0.5 | 0.4 | 0.1 | 0 | 0.6 | -0.6 | 0.49 | 0.2 | 0.29 | 0 | 1.39 | -1.39 | 0.54 | 0.2 | 0.34 |
| Tetracyclic | 0 | 0 | 0 | 0 | 0 | 0 | 0 | 0 | 0 | 0 | 0 | 0 | 0.3 | 0.94 | -0.64 | 0.39 | 0 | 0.39 |
| **Sum** | 5.05 | 5.87 | -0.82 | 3.32 | 4.42 | -1.1 | 2.26 | 2.97 | -0.71 | 8.25 | 8.61 | -0.36 | 9.72 | 16.03 | -6.31 | 7 | 17.61 | -10.61 |

[*] ΔW denotes the difference between experimental concentrations and calculated concentrations; the background color scale: from green to red, represents Δ value increases from the smallest negative number to the largest positive number, implying the synergistic effect from inhibition to promotion.

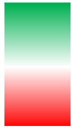

**Table A.3** Combustion kinetic parameters of samples in stage 1 and stage 2 by FWO and KAS methods.

| Sample | α | Stage 1 | | Stage 2 | | Sample | α | Stage 1 | | Stage 2 | |
|---|---|---|---|---|---|---|---|---|---|---|---|
| | | FWO | KAS | FWO | KAS | | | FWO | KAS | FWO | KAS |
| | | E kJmol$^{-1}$ | E kJmol$^{-1}$ | E kJmol$^{-1}$ | E kJmol$^{-1}$ | | | E kJmol$^{-1}$ | E kJmol$^{-1}$ | E kJmol$^{-1}$ | E kJmol$^{-1}$ |
| RW | 0.2 | 218.91 | 220.99 | 202.24 | 201.20 | HW | 0.2 | 174.10 | 173.68 | 171.65 | 168.94 |
| | 0.25 | 222.94 | 225.06 | 200.03 | 198.79 | | 0.25 | 173.95 | 173.43 | 160.35 | 156.80 |
| | 0.3 | 228.79 | 231.13 | 195.21 | 193.55 | | 0.3 | 172.76 | 172.10 | 150.47 | 146.24 |
| | 0.35 | 227.37 | 229.55 | 190.94 | 189.06 | | 0.35 | 172.29 | 171.60 | 142.89 | 138.10 |
| | 0.4 | 220.81 | 222.57 | 186.43 | 184.16 | | 0.4 | 173.55 | 172.93 | 136.17 | 130.86 |
| | 0.45 | 216.31 | 217.83 | 177.98 | 175.26 | | 0.45 | 175.53 | 174.93 | 130.72 | 124.96 |
| | 0.5 | 209.59 | 210.68 | 170.47 | 167.19 | | 0.5 | 182.01 | 181.74 | 124.79 | 118.64 |
| | 0.55 | 203.11 | 203.78 | 164.86 | 161.29 | | 0.55 | 190.94 | 191.06 | 119.81 | 113.24 |
| | 0.6 | 197.42 | 197.79 | 158.22 | 154.14 | | 0.6 | 202.55 | 203.19 | 115.70 | 108.75 |
| | 0.65 | 196.07 | 196.21 | 152.77 | 148.32 | | 0.65 | 220.57 | 222.07 | 110.72 | 103.43 |
| | 0.7 | 192.44 | 192.39 | 144.15 | 139.18 | | 0.7 | 248.31 | 251.25 | 106.53 | 98.94 |
| | 0.75 | 195.84 | 195.96 | 135.70 | 130.28 | | 0.75 | 284.83 | 289.58 | 102.11 | 94.11 |
| | 0.8 | 210.14 | 210.93 | 127.48 | 121.55 | | 0.8 | 331.22 | 338.21 | 98.08 | 89.79 |
| | $E_{ave}$ | 210.75 | 211.91 | 169.73 | 166.46 | | $E_{ave}$ | 207.89 | 208.91 | 128.46 | 122.52 |
| MR28 | 0.2 | 222.63 | 224.89 | 206.90 | 206.19 | MH28 | 0.2 | 175.84 | 175.51 | 186.99 | 185.15 |
| | 0.25 | 225.32 | 227.64 | 201.76 | 200.62 | | 0.25 | 172.68 | 172.10 | 179.00 | 176.51 |
| | 0.3 | 227.29 | 229.55 | 198.05 | 196.63 | | 0.3 | 171.34 | 170.60 | 169.44 | 166.36 |
| | 0.35 | 227.77 | 229.97 | 192.36 | 190.56 | | 0.35 | 170.94 | 170.19 | 160.75 | 156.97 |
| | 0.4 | 220.57 | 222.32 | 185.17 | 182.91 | | 0.4 | 171.42 | 170.69 | 155.53 | 151.40 |
| | 0.45 | 216.23 | 217.66 | 178.06 | 175.26 | | 0.45 | 176.63 | 176.09 | 150.16 | 145.58 |
| | 0.5 | 209.27 | 210.26 | 173.63 | 170.52 | | 0.5 | 179.56 | 179.08 | 145.18 | 140.26 |
| | 0.55 | 203.35 | 204.03 | 169.99 | 166.53 | | 0.55 | 188.88 | 188.89 | 139.88 | 134.52 |
| | 0.6 | 199.00 | 199.37 | 168.41 | 164.87 | | 0.6 | 200.97 | 201.53 | 134.90 | 129.12 |
| | 0.65 | 197.58 | 197.79 | 164.38 | 160.46 | | 0.65 | 217.97 | 219.41 | 130.08 | 123.96 |
| | 0.7 | 196.86 | 197.12 | 160.19 | 156.05 | | 0.7 | 238.36 | 240.77 | 125.90 | 119.47 |
| | 0.75 | 196.86 | 196.96 | 157.27 | 152.89 | | 0.75 | 272.50 | 276.52 | 122.34 | 115.56 |
| | 0.8 | 208.80 | 209.51 | 153.08 | 148.40 | | 0.8 | 315.33 | 321.59 | 117.76 | 110.66 |
| | $E_{ave}$ | 211.66 | 212.85 | 177.64 | 174.76 | | $E_{ave}$ | 204.03 | 204.84 | 147.53 | 142.73 |
| MR55 | 0.2 | 216.94 | 218.91 | 213.15 | 212.76 | MH55 | 0.2 | 164.70 | 163.79 | 194.65 | 193.22 |
| | 0.25 | 218.12 | 220.07 | 205.40 | 204.44 | | 0.25 | 162.09 | 160.96 | 183.27 | 181.00 |
| | 0.3 | 221.68 | 223.65 | 195.60 | 194.05 | | 0.3 | 161.22 | 159.96 | 172.44 | 169.44 |
| | 0.35 | 219.39 | 221.07 | 185.25 | 182.99 | | 0.35 | 159.01 | 157.63 | 164.94 | 161.46 |
| | 0.4 | 213.46 | 214.83 | 177.19 | 174.59 | | 0.4 | 160.27 | 158.88 | 159.17 | 155.22 |
| | 0.45 | 210.14 | 211.26 | 172.29 | 169.11 | | 0.45 | 164.62 | 163.45 | 154.43 | 150.07 |
| | 0.5 | 203.42 | 204.11 | 166.52 | 162.95 | | 0.5 | 168.97 | 168.03 | 149.92 | 145.25 |
| | 0.55 | 200.66 | 201.20 | 162.64 | 158.80 | | 0.55 | 174.97 | 174.26 | 146.21 | 141.17 |
| | 0.6 | 197.58 | 197.79 | 159.48 | 155.31 | | 0.6 | 184.30 | 183.99 | 142.57 | 137.18 |
| | 0.65 | 193.62 | 193.72 | 155.61 | 151.15 | | 0.65 | 199.39 | 199.79 | 139.49 | 133.86 |

| | | | | | | | | | | | |
|---|---|---|---|---|---|---|---|---|---|---|---|
| | 0.7 | 194.65 | 194.71 | 154.19 | 149.57 | | 0.7 | 216.70 | 217.91 | 135.54 | 129.53 |
| | 0.75 | 197.26 | 197.37 | 151.42 | 146.49 | | 0.75 | 242.15 | 244.60 | 132.30 | 126.12 |
| | 0.8 | 209.51 | 210.26 | 148.50 | 143.33 | | 0.8 | 272.58 | 276.52 | 128.98 | 122.47 |
| | $E_{ave}$ | 207.42 | 208.38 | 172.86 | 169.66 | | $E_{ave}$ | 187.00 | 186.91 | 154.15 | 149.69 |
| MR82 | 0.2 | 221.52 | 223.65 | 209.75 | 209.10 | MH82 | 0.2 | 185.01 | 185.07 | 191.17 | 189.48 |
| | 0.25 | 227.29 | 229.63 | 198.92 | 197.54 | | 0.25 | 176.87 | 176.42 | 179.32 | 176.84 |
| | 0.3 | 227.37 | 229.55 | 187.86 | 185.82 | | 0.3 | 176.63 | 176.09 | 172.44 | 169.52 |
| | 0.35 | 222.47 | 224.31 | 179.08 | 176.51 | | 0.35 | 175.21 | 174.59 | 165.33 | 161.87 |
| | 0.4 | 218.04 | 219.57 | 173.47 | 170.44 | | 0.4 | 177.50 | 176.92 | 160.35 | 156.55 |
| | 0.45 | 210.14 | 211.26 | 168.33 | 164.95 | | 0.45 | 180.11 | 179.58 | 157.03 | 152.89 |
| | 0.5 | 203.42 | 204.11 | 165.49 | 161.87 | | 0.5 | 186.83 | 186.73 | 153.87 | 149.40 |
| | 0.55 | 201.13 | 201.61 | 161.85 | 157.88 | | 0.55 | 190.23 | 190.22 | 152.45 | 147.74 |
| | 0.6 | 198.05 | 198.37 | 160.98 | 156.89 | | 0.6 | 202.32 | 202.86 | 149.45 | 144.58 |
| | 0.65 | 197.66 | 197.87 | 160.43 | 156.14 | | 0.65 | 215.12 | 216.33 | 146.76 | 141.59 |
| | 0.7 | 195.76 | 195.79 | 159.88 | 155.39 | | 0.7 | 229.66 | 231.46 | 144.78 | 139.34 |
| | 0.75 | 200.66 | 200.87 | 160.12 | 155.55 | | 0.75 | 258.75 | 261.97 | 141.31 | 135.52 |
| | 0.8 | 221.60 | 222.90 | 160.43 | 155.72 | | 0.8 | 278.35 | 282.51 | 136.09 | 129.95 |
| | $E_{ave}$ | 211.16 | 212.27 | 172.82 | 169.52 | | $E_{ave}$ | 202.51 | 203.14 | 157.72 | 153.48 |
| OSC | 0.2 | 140.44 | 136.43 | 180.27 | 174.59 | | | | | | |
| | 0.25 | 136.72 | 132.36 | 185.25 | 179.67 | | | | | | |
| | 0.3 | 134.04 | 129.37 | 184.22 | 178.42 | | | | | | |
| | 0.35 | 132.61 | 127.87 | 184.46 | 178.67 | | | | | | |
| | 0.4 | 130.80 | 125.79 | 189.75 | 184.07 | | | | | | |
| | 0.45 | 130.40 | 125.21 | 191.65 | 185.90 | | | | | | |
| | 0.5 | 129.61 | 124.38 | 193.78 | 188.06 | | | | | | |
| | 0.55 | 128.27 | 122.88 | 189.75 | 183.74 | | | | | | |
| | 0.6 | 127.79 | 122.22 | 179.64 | 172.93 | | | | | | |
| | 0.65 | 127.40 | 121.72 | 167.15 | 159.38 | | | | | | |
| | 0.7 | 128.11 | 122.30 | 146.76 | 137.60 | | | | | | |
| | 0.75 | 127.56 | 121.63 | 138.94 | 128.62 | | | | | | |
| | 0.8 | 132.38 | 126.54 | 155.14 | 145.08 | | | | | | |
| | $E_{ave}$ | 131.24 | 126.05 | 175.90 | 168.98 | | | | | | |

**Table A.4** Apparent activation energies of the combustion of woody biomass from related work.

| Sample | E kJ/mol (ave) | Kinetic method | References |
|---|---|---|---|
| RW | 190.31 | FWO, KAS | Present work |
| HW | 167.29 | FWO, KAS | Present work |
| Acacia | 190.45 | FWO | [A-1] |
| Torrefied acacia | 163.85 | FWO | [A-1] |
| Pine | 191.14 | FWO | [A-1] |
| Torrefied pine | 143.12 | FWO | [A-1] |
| Fir wood | 197.33 | Coat Redfern | [A-2] |
| Poplar wood chip | 181.22 | FWO, KAS | [A-3] |
| Pine wood | 186.92 | FWO | [A-4] |
| wood sawdust | 178.43 | FWO | [A-5] |

[A-1] Wilk, M., Magdziarz, A., Gajek, M., Zajemska, M., Jayaraman, K., & Gokalp, I. (2017). Combustion and kinetic parameters estimation of torrefied pine, acacia and Miscanthus giganteus using experimental and modelling techniques. Bioresource Technology, 243, 304-314.

[A-2] López-González, D., Fernandez-Lopez, M., Valverde, J. L., & Sanchez-Silva, L. (2013). Thermogravimetric-mass spectrometric analysis on combustion of lignocellulosic biomass. Bioresource technology, 143, 562-574.

[A-3] Liu, L., Pang, Y., Lv, D., Wang, K., & Wang, Y. (2021). Thermal and kinetic analyzing of pyrolysis and combustion of self-heating biomass particles. Process Safety and Environmental Protection, 151, 39-50.

[A-4] Xu, X., Pan, R., & Chen, R. (2021). Combustion characteristics, kinetics, and thermodynamics of pine wood through thermogravimetric analysis. Applied Biochemistry and Biotechnology, 193(5), 1427-1446.

[A-5] Wang, T., Hou, H., Ye, Y., Rong, H., Li, J., & Xue, Y. (2019). Combustion behavior of refuse-derived fuel produced from sewage sludge and rice husk/wood sawdust using thermogravimetric and mass spectrometric analyses. Journal of Cleaner Production, 222, 1-11.

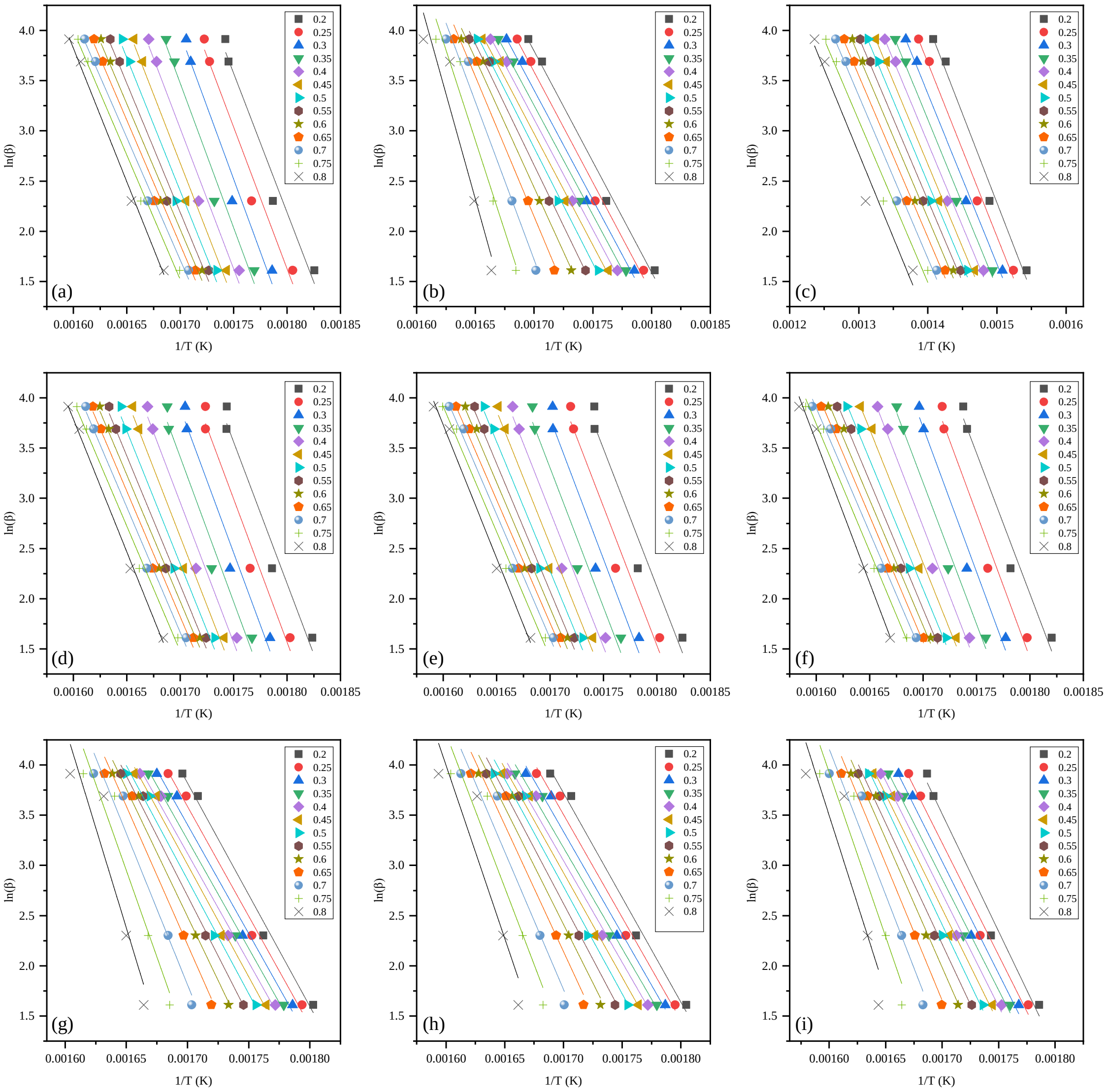

**Figure A.1** Iso-conversional plots at various conversion degree for (a) RW, (b) HW, (c) OSC, (d) OSC/RW28, (e) OSC/RW55, (f) OSC/RW82, (g) OSC/HW28, (h) OSC/HW55, (i) OSC/HW82 in stage 1 by FWO method.

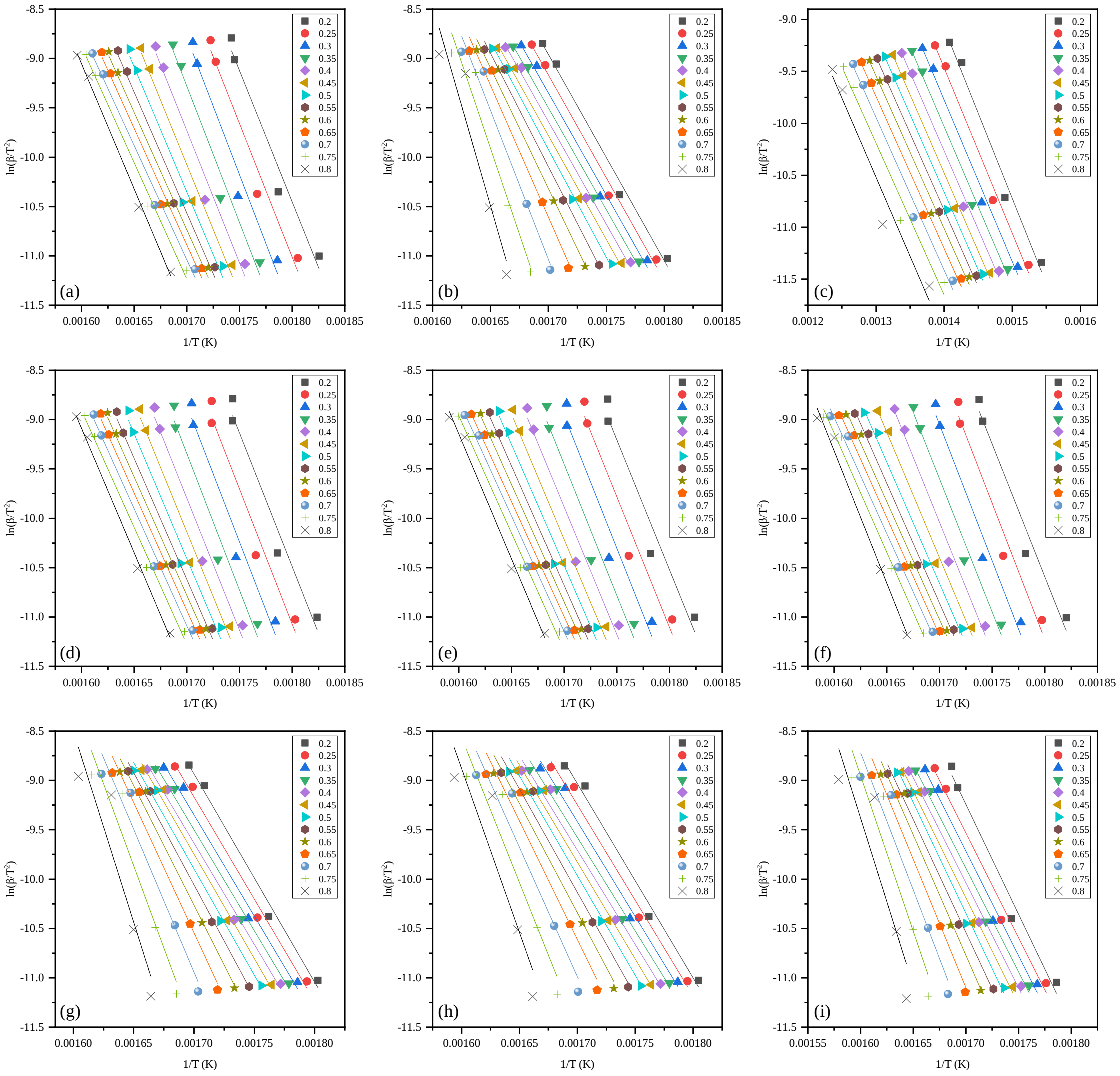

**Figure A.2** Iso-conversional plots at various conversion degree for (a) RW, (b) HW, (c) OSC, (d) OSC/RW28, (e) OSC/RW55, (f) OSC/RW82, (g) OSC/HW28, (h) OSC/HW55, (i) OSC/HW82 in stage 1 by KAS method.

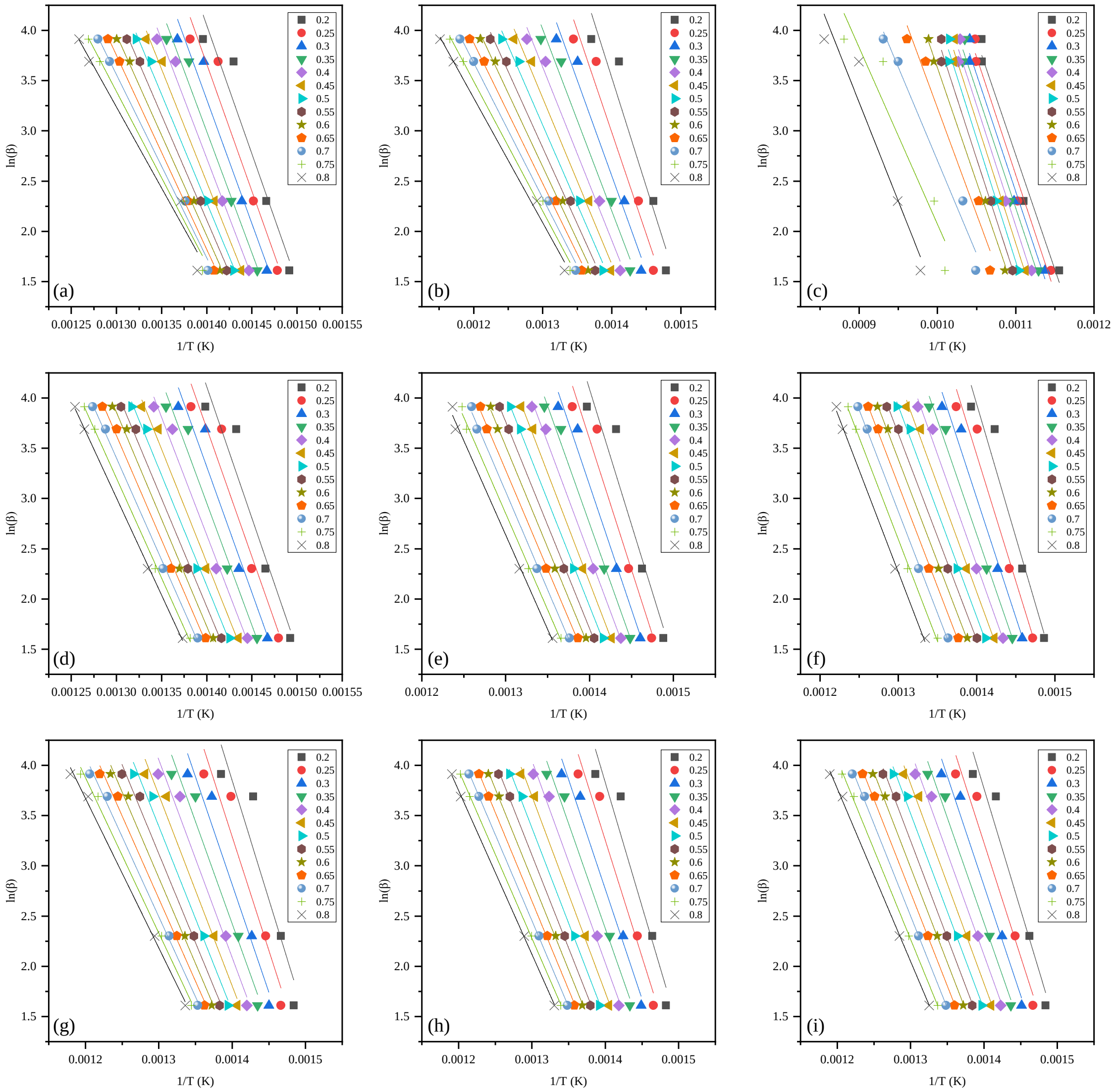

**Figure A.3** Iso-conversional plots at various conversion degree for (a) RW, (b) HW, (c) OSC, (d) OSC/RW28, (e) OSC/RW55, (f) OSC/RW82, (g) OSC/HW28, (h) OSC/HW55, (i) OSC/HW82 in stage 2 by FWO method.

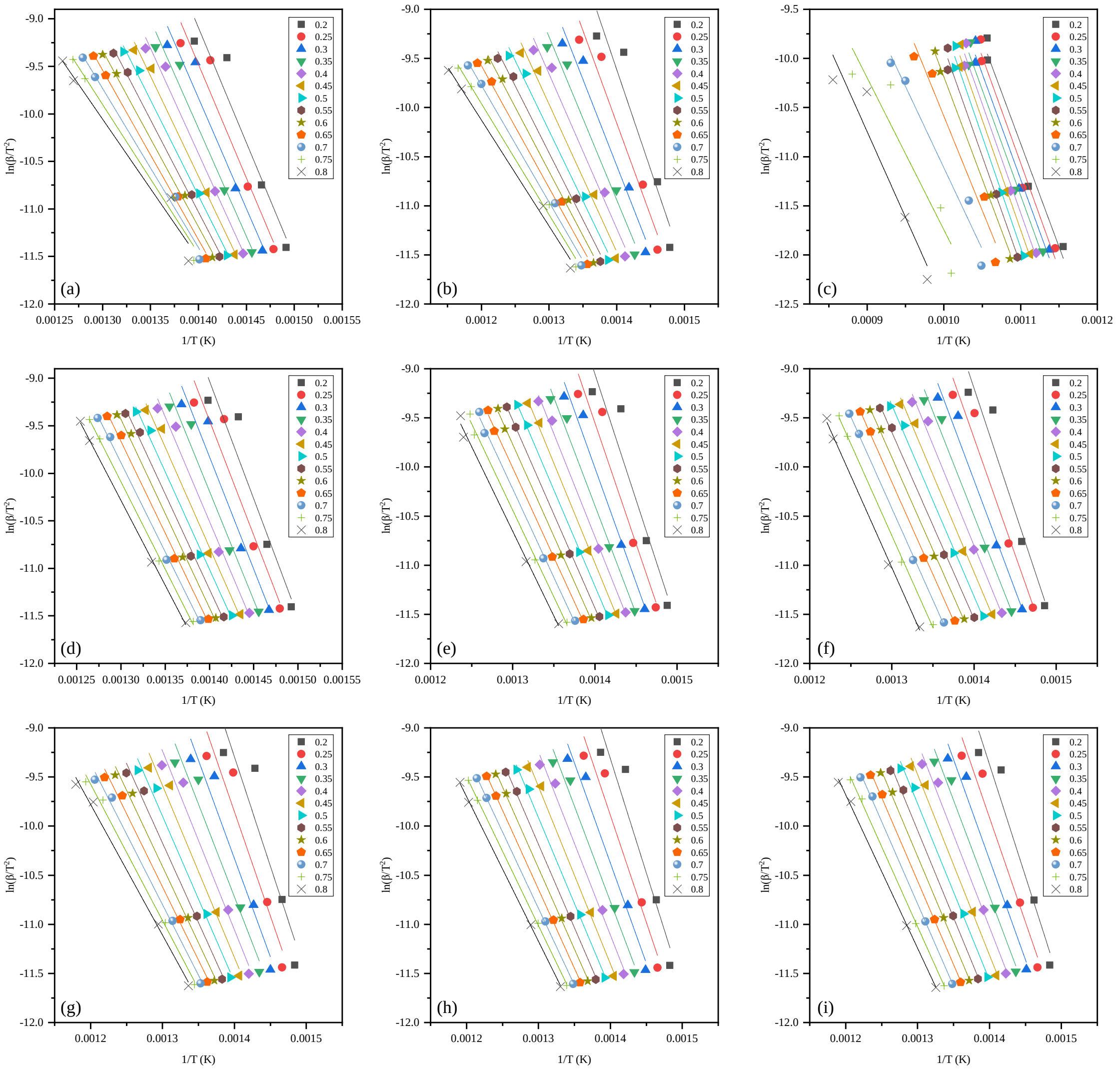

**Figure A.4** Iso-conversional plots at various conversion degree for (a) RW, (b) HW, (c) OSC, (d) OSC/RW28, (e) OSC/RW55, (f) OSC/RW82, (g) OSC/HW28, (h) OSC/HW55, (i) OSC/HW82 in stage 2 by KAS method.